Emissions and Chemistry of Reactive Nitrogen in Wildfire Plumes

Qiaoyun Peng

A dissertation

submitted in partial fulfillment of the

requirements for the degree of

Doctor of Philosophy

University of Washington

2022

Reading Committee:

Joel Thornton, Chair

Lyatt Jaeglé

Becky Suess

Program Authorized to Offer Degree:

Atmospheric Sciences

University of Washington

Abstract

Emissions and Chemistry of Reactive Nitrogen in Wildfire Plumes

Qiaoyun Peng

Chair of the Supervisory Committee:

Joel Thornton

Department of Atmospheric Sciences

Wildfires are an important source of reactive nitrogen species to the atmosphere, accounting for approximately 25% of global annual nitrogen oxides (NO_x). Emissions of wildfires are highly variable depending on factors such as fuel types and burning conditions, yet in situ measurements and quantification of primary emissions from open wildfires have been scarce. This work presents detailed observations of reactive nitrogen emissions and chemistry within wildfire plumes sampled during the Western Wildfire Experiment for Cloud chemistry, Aerosol absorption and Nitrogen (WE-CAN) aircraft campaign with unprecedented comprehensive measurements of over 250 wildfire plume transects. In this dissertation, I systematically investigate the complexities of reactive nitrogen chemistry in authentic smoke, including radical sources, photochemical evolutions, and secondary pollutant formation. I demonstrate that the emission ratios of nitrous

acid (HONO) from fires may be significantly underestimated in previous studies where measurements were not close enough to fire sources, highlighting the critical need to update the values in regional air quality models. I show that HONO is the most important primary radical source in fresh wildfire plumes, contributing over 90% of hydrogen oxidies ($HO_x \equiv OH + HO_2$) production in plumes with age shorter than an hour. I then evaluate potential drivers of variability in HONO emissions across the range of fires sampled, and find a dependence on modified combustion efficiency and fuel nitrogen proxy. With the observational constraints, I examine the rapid daytime post-emission changes of reactive nitrogen using a 0-D photochemical box model. The model underpredicts the loss of NO_x in fires with high NO_x emissions, and I show that current model mechanisms likely miss out on a suite of oxidized organic nitrogen species such as alkyl and acyl peroxynitrates in fire plumes, consistent with a suite of organic nitrogen compounds measured by chemical ionization mass spectrometry. I find HONO mixing ratios in aged smoke are systematically higher than expected from known chemical reactions, and conducted extensive correlation analysis to identify potential secondary sources of HONO. From an ideal case study of sufficiently aged smoke, I show that the missing HONO production could be predicted by an empirical multilinear regression of two candidate mechanisms – the photolysis of particle nitrate and the aerosol heterogeneous uptake of NO_2. The relationship could also be extended to all aged smoke detected in the campaign with good consistency.

TABLE OF CONTENTS

LIST OF FIGURES

Chapter 2

Chapter 3

Chapter 4

LIST OF TABLES

Chapter 2

Chapter 3

Chapter 4

ACKNOWLEDGEMENTS

I am indebted to my advisor, Joel Thornton, for the immense support and understanding throughout my PhD journey. Joel offers an endless supply of inspiration, and has enlightened me to turn the seemingly messy data into novel findings. I always feel recharged and motivated after our meetings, and am amazed at how Joel could read my numerous revisions with extraordinary patience. I couldn't be more grateful for the encouragement and freedom that Joel gives me in pursuing the goals in research and career in general. I also would like to say thanks to my PhD committee for offering timely support and insightful feedback at every stage of my study.

I feel lucky to have worked with my groupmates, Ben Lee, Brett Palm, Jessica Haskins, Carley Fredrickson, Phil Rund, Jeremy Chan, Siegfried Schobesberger, Yue Zhao, Emma D'Ambro, Megan McKeown, Julia Greenwald, and Lexie Goldberger, for all the stimulating discussions and daily chats. Working in the office alongside them is delightful, and I love the group get-togethers and the tradition of decorating Joel's office doors at Christmas. It is their kind support and comments that prepared me for all the conference posters, talks, and defense. I am particularly grateful to Ben and Brett for mentoring on topics like mass spectrum analysis and instrument deployment, as well as all general research critiques that are really invaluable in shaping my research methodology.

I would also thank the WE-CAN science team and my collaborators, Emily Fischer, Frank Flocke, Lu Hu, Sam Hall, Delphine Farmer, and many others, for making the intensive field campaign a cherished time of my PhD life, and giving constructive comments to my papers.

Thanks to all my friends in and out of the department, without whom I would not have survived the dark rainy days. Thanks to my partner Yue for the tremendous joy he brought to my life, and enduring the sleepless nights before deadlines. Finally, thanks to my parents for their unwavering belief in me with love and care.

Chapter 1. INTRODUCTION

1.1 OVERVIEW OF WILDFIRE CHEMISTRY

Wildfires have been recognized to be an important source of reactive trace gases and particles, which significantly impact tropospheric chemistry, air quality, public health, and climate on regional or even global scales (Adams et al., 2019; Garcia-Hurtado et al., 2014; Y. Liu et al., 2014; Urbanski, 2014; Yokelson et al., 2007). Fresh smoke from wildfires is a complex mixture of gases and aerosols, the relative proportions of which are affected by many factors including fuel type, combustion efficiency and meteorological conditions (Akagi et al., 2011; Jaffe & Wigder, 2012). Smoke particles directly affect radiative budget through scattering and absorbing radiation and indirectly through changing cloud properties by serving as cloud condensation nuclei (CCN). Additionally, carbon dioxide (CO_2) is a dominant component of fire emissions, which contributes substantially to the greenhouse effect. These disturbances may lead to climate effects including enhancement of climate anomalies like droughts (Rosenfeld et al., 2008), changes in stratosphere temperatures at similar or even larger magnitudes than induced by volcanic eruptions (Stocker et al., 2021), as well as dramatic shifts in terrestrial carbon balance with mass and energy repartitioning between biosphere and atmosphere (Zhao et al., 2021). From the air quality perspective, wildfires also emit large amounts of hydrocarbons and nitrogen oxides (NO_x = NO + NO_2), which are important precursors of ozone (O_3) and particulate matter (PM) in the presence of sunlight. As important criteria pollutants, both O_3 and PM produced from wildfires deteriorate air quality and pose serious health risks to those exposed (Chen et al., 2017; J. C. Liu et al., 2017).

The potential for intense wildland fires is expected to rise in a warming climate, and fire season length is predicted to increase by over 20 days per year for northern high latitudes at the end of the century (Flannigan et al., 2013; Jolly et al., 2015). Significant increase in wildfire frequency and duration have been reported over the last few decades, and frequency of large fire events (>1000 km^2) has more than doubled in North American boreal regions (Dennison et al., 2014; Kasischke & Turetsky, 2006; Westerling et al., 2006). These shifts in fire regimes imply more and larger fire emissions over the prolonged fire seasons. As wildfires have been shown to promote criteria pollutants formation (X. Liu et al., 2017; O'Dell et al., 2020), it is important to better understand the emissions, photochemistry and impacts of these fires.

With the ongoing interest in wildfire emissions in the context of global warming and air quality impacts, a number of laboratory and field campaigns targeting fire emission and chemistry have been carried out in the past few years in the western United States (Akagi et al., 2012; Burling et al., 2011; Lindaas et al., 2021; McKendry et al., 2011; Robinson et al., 2021; Selimovic et al., 2018; Singh et al., 2012; Veres et al., 2010). O_3 evolution in fire plumes is found to be highly variable, with the majority of observations indicating net enhancements of varying magnitude (Morris et al., 2006; Oltmans et al., 2010; Pfister et al., 2006), while several studies showing that O_3 is barely formed or even depleted downwind (M. J. Alvarado et al., 2010; Verma et al., 2009). In wildfire plumes, particulate matter less than 2.5 microns in size ($PM_{2.5}$), arises from both primary (i.e. directly emitted) and secondary (i.e., formed from chemistry in the atmosphere) sources. Primary $PM_{2.5}$ is mostly in the form of organic or elemental (black) carbon, while secondary $PM_{2.5}$ is either organic or inorganic. The relative contribution of primary and secondary organic aerosol (POA or SOA, respectively) to $PM_{2.5}$ varies greatly among different fire events and evolves downwind (Akagi et al., 2012; McKendry et al., 2011; Palm et al., 2020), while

secondary inorganic aerosol formation is often dominated by ammonium nitrate from oxidation of NO_x to nitric acid (HNO_3). The variability in O_3 and $PM_{2.5}$ formation and evolution observed in wildfire plumes implies variations in precursor emissions and subsequent photochemistry of fire plumes, both over time for a given fire and across different fires.

The pathways to form O_3 and $PM_{2.5}$ generally involve many photochemical reactions driven by complex radical chemistry. Figure 1.1 shows a schematic of oxidative chemistry in daytime wildfire plumes. Various radical precursors emitted or produced from wildfires undergo photolysis, giving rise to critical oxidants including hydroxyl radicals (OH) and hydroperoxyl radicals (HO_2). OH initiates the oxidation of Volatile Organic Compounds (VOCs) into alkyl radicals (R), which immediately reacts with O_2 to form peroxy radical (RO_2). RO_2 takes on further reactions with NO and either converts to RO and NO_2, or produces alkyl nitrates ($RONO_2$) with larger RO_2 molecules tending to have higher yields. RO_2 reactions with NO_2 lead to formation of peroxynitrates (RO_2NO_2), a subset of which (e.g., peroxy acyl nitrates (PAN)) may establish a thermal equilibrium with NO_2, allowing sequestered NO_x to be re-released to the atmosphere in downwind regions while descending into lower altitudes with higher temperatures. Organic nitrates, as an important NO_x sink, may condense into particulate phase and contributes to the growth of Secondary Organic Aerosol (SOA), which represents a major component of submicron-sized aerosol and has important climate and air quality implications (Murphy et al., 2006; Shrivastava et al., 2017; Pye et al., 2021). A competing NO_2 sink is the oxidation by OH into HNO_3 which is generally considered a permanent loss from the atmosphere. The partitioning of reactive nitrogen into reversible reservoirs with variable lifetimes and irreversible sinks like HNO_3 determines the fate of NO_x. Several studies have explored wildfire emissions as well as partitioning of reactive nitrogen compounds, and showed substantial variability in emission factors and

fractionation with fire intensity and sizes (Castellanos et al., 2014; Juncosa Calahorrano et al., 2020; Lindaas et al., 2021; Mebust et al., 2011). Consequently, the different NO_x loss pathways may lead to variable photochemical O_3 formation with plume transport. The formation of ozone has a non-linear dependence on the relative amount of VOC and NO_x. In NO_x-limited (or VOC-saturated) regimes, increasing NO_x promotes O_3 production through facilitating the radical cycling over peroxides formation; in NO_x-saturated (or VOC-limited) regimes, increasing NO_x decreases O_3 production as a result of faster loss to HNO_3. Evolving physiochemical conditions in wildfire plumes further complicates the O_3 formation regime as a function of fire characteristics, meteorological conditions, and distance downwind. Jin et al. (2021) observed NO_x-limited chemistry from over 3000 fires globally based on satellite-derived NO_x lifetime analysis, with more efficient chemical loss of NO_x at larger fire NO_x emissions. Robinson et al. (2021) reported rapid (< 0.5 h since emission) transitions in O_3 production scheme from NO_x-saturated to NO_x-limited driven by changing radical productions in wildfire plumes from observations during the FIREX campaign. Oxygenated VOCs like aldehydes have substantial secondary productions in wildfire plumes, while NO_x is efficiently oxidized and sequestered into different reservoirs. Thus, most fire plumes are NO_x-saturated in near-source regions, and then transition to being NO_x-limited with transport (M. J. Alvarado et al., 2015; Müller et al., 2016). As varying fire conditions may change [VOCs]/[NO_x] as a function of distance, the fractionation of nitrogen species also changes. The interactions between NO_x and VOCs influence the absolute production rate of O_3 by setting the NO/NO_2 ratio and peroxy radical abundance, which in turn affects the lifetime of NO_x and its conversion into reservoirs as well as O_3 production efficiency of a fire plume. Further, the downwind O_3 may be affected when wildfire smoke mixes with NO_x-rich urban plumes. Buysse et al. (2019) observed elevated O_3 and $PM_{2.5}$ at nearly all air quality system sites on days influenced

by wildfire smoke from ground-based monitoring in 18 western US cities during summer 2013-2017. The impacts of wildfires on air quality in urban areas is sensitive to accurate description of NO_x fates and VOC oxidation, which in turn depends on getting the evolution of NO_x and VOC lifetimes simulated correctly as the plumes are transported and aged as they move from wildlands to urban areas. Therefore, simulation of different fire scenarios is essential to enable more comprehensive evaluations of how the fate of NO_x and formation of secondary pollutants varies with fire conditions and emission factors.

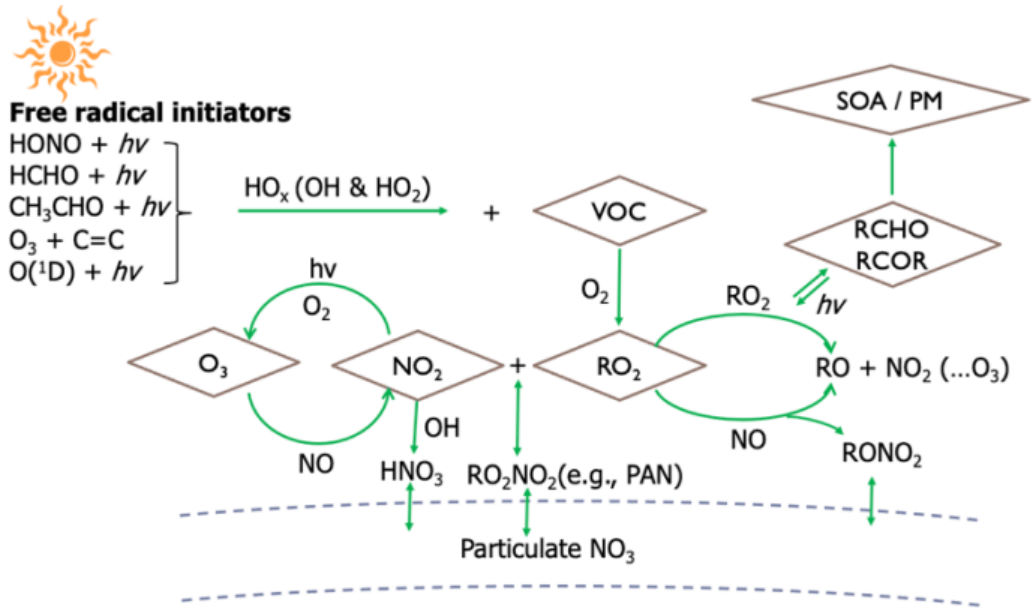

Figure 1.1. Schematic of reactive nitrogen chemistry in daytime wildfire plumes.

To understand and forecast the air quality and climate impacts of wildfires requires an accurate description of the fate of NO_x, the radical drivers of plume chemical evolution, and the processes leading to secondary organic and inorganic aerosol. While the photochemistry of biomass burning plumes has been studied previously in field and laboratory experiments (Akagi et al., 2012, 2013; M. J. Alvarado et al., 2010; Matthew James Alvarado & Prinn, 2009; Parrington

et al., 2013), relatively few observational data sets are available with pseudo-Lagrangian sampling of wildfire plume composition. Currently, only a handful of studies have reported on reactive nitrogen chemistry in biomass burning plume intercepts, and near-field photochemical modeling are particularly lacking. Accurate estimates and model representation of these emissions are essential to determining the impact of wildfires on nitrogen reservoir and tropospheric ozone on larger scales. Further work is needed to develop models for predicting fire-sourced pollutants with extended interpretation of limited field observations to different locations and time periods.

Ozone production, secondary PM formation, and reactive nitrogen fate are critically dependent on primary radical sources that regulate the local oxidizing capacity. Past studies have revealed that radicals play a critical role in the formation of secondary pollutants in plumes from urban or industrial origin (Z. Liu et al., 2012; Tan et al., 2019; Volkamer et al., 2010), yet few studies have reported the radical budget and oxidative capacity within wildfire plumes. A key radical source in wildfire plumes is likely HONO photolysis (Harris et al., 1982; Theys et al., 2020; Zhang et al., 2012), and studies have shown significant variabilities in HONO emissions from fire to fire (Akagi et al., 2011; Hodshire et al., 2019). The emission profiles are in part regulated by the predominance of different burning conditions, as HONO and NO_x are primarily produced in the flaming stage with more complete oxidation in comparison to the smoldering stage at which incomplete oxidation products like CO are favored (Yokelson et al., 2013). Previous *in situ* HONO measurements in biomass burning plumes were largely confined to prescribed fires, and more detailed information on primary HONO emissions from wildland fires at the source level is essential for quantifying fire-generated HONO, examining the governing factors of emission variabilities, as well as simulating subsequent photochemical impacts.

Several box model studies have corroborated the importance of HONO photolysis to HO_x budget and further impact on O_3 build-up (Elshorbany et al., 2009; Harris et al., 1982; Lu et al., 2010; Zhang et al., 2012). HONO can be an important source of OH radicals in the early stages of wildfires, so any underestimation has a significant impact on the oxidizing capacity of the atmosphere. However, a scarcity of *in situ* HONO measurements and uncertainties in HONO primary emissions currently limit the ability to understand and simulate photochemical production of O_3 and secondary aerosol within wildfire plumes. It is critical to develop a detailed understanding of the radical budget and relevant photochemistry in biomass burning plumes as it regulates primary pollutant removal and secondary pollutant formation in fire-prone regions.

As smoke travels downwind, rapid daytime photolytic loss leads to exponential decay of directly emitted HONO. Multiple field studies have shown much higher daytime HONO levels than expected from known reactions, implying large unidentified HONO sources to reconcile such observations (Sörgel et al., 2011; Ye et al., 2018). Postulated secondary HONO sources involve different precursors such as inorganic oxides and particulate nitrate (pNO_3). Heterogeneous reactions of NO_2 on surfaces including ground (Kleffmann et al., 2003; Stutz et al., 2002; Su et al., 2008) and aerosol (Ammann et al., 1998; Han et al., 2016; Kleffmann et al., 1999) are considered a potentially ubiquitous source of HONO, but with an uncertain magnitude especially for aerosol particle surfaces. Photosensitized heterogeneous reduction of NO_2 on organic substrates or soot particles has been observed as a major HONO source in many studies (Aubin & Abbatt, 2007; George et al., 2005; Han et al., 2016). Other studies have suggested that particulate nitrate can be photolyzed to produce HONO (Bao et al., 2018; Ye et al., 2016; Zhou et al., 2001, 2002, 2003). Novel homogeneous HONO sources have also been proposed more recently but were considered irrelevant in actual atmospheric conditions (Bejan et al., 2006; S. Li et al., 2008; X. Li et al., 2014).

A consensus on the importance of secondary HONO sources has not yet been achieved, and the dominant mechanisms of HONO formation are still widely discussed. The potential resupply of HONO from secondary processes in smoke plumes may play an important role in the radical recycling and chemical transformations downwind. Still, the important chemical processes contributing to HONO in biomass burning events remain understudied. With improved quantitative understanding of fire emissions and chemistry, better assessments may be achieved on the production and fate of important radical precursors like HONO, which is critical for describing the fate of reactive nitrogen and formation of ozone and secondary $PM_{2.5}$ components in wildfire plumes.

1.2 MOTIVATING QUESTIONS FOR THIS WORK

My work is designed to better understand and simulate the chemical evolution of authentic wildfire emissions utilizing in situ measurements during the Western Wildfire Experiment for Cloud Chemistry, Aerosol Absorption, and Nitrogen (WE-CAN) campaign. This work seeks to addresses the gaps in wildfire emissions and chemistry with a focus on the fate of reactive nitrogen species. The motivating questions for each chapter are presented as below:

Chapter 2. HONO emissions from western US wildfires provide dominant radical source in fresh wildfire smoke [Peng et al., 2020]

How much HONO is emitted relative to CO from wildfires in the western U.S.? How do the emission ratios (HONO/CO) change with different fuel characteristics and burning conditions? What are the main factors driving uncertainties in HONO emission ratios?

Chapter 3. Observations and Modeling of NO_x Photochemistry and Fate in Fresh Wildfire Plumes [Peng et al., 2021]

What important chemical transformations happen to reactive nitrogen as fire emissions get transported, diluted, and reacted with radicals? What are ozone and particulate nitrate production rates and can these be simulated using known chemistry?

Chapter 4. Observational Constraints on Secondary HONO Production in Aged Wildfire Smoke from Airborne Measurements in Western US [in prep]

What is the evidence of active secondary HONO chemistry in biomass burning plumes during the daytime? What are the sources of secondary HONO and what are the implications for its role in reactive nitrogen cycling?

1.3 REFERENCES

Adams, C., McLinden, C. A., Shephard, M. W., Dickson, N., Dammers, E., Chen, J., et al. (2019). Satellite-derived emissions of carbon monoxide, ammonia, and nitrogen dioxide from the 2016 Horse River wildfire in the Fort McMurray area. *Atmospheric Chemistry and Physics*, *19*(4), 2577–2599. https://doi.org/10.5194/acp-19-2577-2019

Akagi, S. K., Yokelson, R. J., Wiedinmyer, C., Alvarado, M. J., Reid, J. S., Karl, T., et al. (2011). Atmospheric Chemistry and Physics Emission factors for open and domestic biomass burning for use in atmospheric models. *Atmos. Chem. Phys*, *11*, 4039–4072. https://doi.org/10.5194/acp-11-4039-2011

Akagi, S. K., Craven, J. S., Taylor, J. W., Mcmeeking, G. R., Yokelson, R. J., Burling, I. R., et al. (2012). Evolution of trace gases and particles emitted by a chaparral fire in California. *Atmos. Chem. Phys*, *12*, 1397–1421. https://doi.org/10.5194/acp-12-1397-2012

Akagi, S. K., Yokelson, R. J., Burling, I. R., Meinardi, S., Simpson, I., Blake, D. R., et al. (2013). Measurements of reactive trace gases and variable O $_3$ formation rates in some South Carolina biomass burning plumes. *Atmospheric Chemistry and Physics*, *13*(3), 1141–1165. https://doi.org/10.5194/acp-13-1141-2013

Alvarado, M. J., Logan, J. A., Mao, J., Apel, E., Riemer, D., Blake, D., et al. (2010). Nitrogen oxides and PAN in plumes from boreal fires during ARCTAS-B and their impact on ozone: an integrated analysis of aircraft and satellite observations. *Atmospheric Chemistry and Physics*, *10*(20), 9739–9760. https://doi.org/10.5194/acp-10-9739-2010

Alvarado, M. J., Lonsdale, C. R., Yokelson, R. J., Akagi, S. K., Coe, H., Craven, J. S., et al. (2015). Investigating the links between ozone and organic aerosol chemistry in a biomass burning plume from a prescribed fire in California chaparral. *Atmospheric Chemistry and Physics*, *15*(12), 6667–6688. https://doi.org/10.5194/acp-15-6667-2015

Alvarado, Matthew James, & Prinn, R. G. (2009). Formation of ozone and growth of aerosols in young smoke plumes from biomass burning: 1. Lagrangian parcel studies. *Journal of Geophysical Research Atmospheres*, *114*(9), D09306. https://doi.org/10.1029/2008JD011144

Ammann, M., Kalberer, M., Jost, D. T., Tobler, L., Rössler, E., Piguet, D., et al. (1998). Heterogeneous production of nitrous acid on soot in polluted air masses. *Nature 1998 395:6698*, *395*(6698), 157–160. https://doi.org/10.1038/25965

Aubin, D. G., & Abbatt, J. P. D. (2007). Interaction of NO2 with hydrocarbon soot: focus on HONO yield, surface modification, and mechanism. *The Journal of Physical Chemistry. A*, *111*(28), 6263–6273. https://doi.org/10.1021/JP068884H

Bao, F., Li, M., Zhang, Y., Chen, C., & Zhao, J. (2018). Photochemical Aging of Beijing Urban PM2.5: HONO Production. *Environmental Science and Technology*, *52*(11), 6309–6316. https://doi.org/10.1021/ACS.EST.8B00538/SUPPL_FILE/ES8B00538_SI_001.PDF

Bejan, I., Abd El Aal, Y., Barnes, I., Benter, T., Bohn, B., Wiesen, P., & Kleffmann, J. (2006). The photolysis of ortho-nitrophenols: a new gas phase source of HONO. *Physical Chemistry Chemical Physics*, *8*(17), 2028–2035. https://doi.org/10.1039/B516590C

Burling, I. R., Yokelson, R. J., Akagi, S. K., Urbanski, S. P., Wold, C. E., Griffith, D. W. T., et al. (2011). Airborne and ground-based measurements of the trace gases and particles emitted by prescribed fires in the United States. *Atmospheric Chemistry and Physics*, *11*(23), 12197–12216. https://doi.org/10.5194/acp-11-12197-2011

Buysse, C. E., Kaulfus, A., Nair, U., & Jaffe, D. A. (2019). Relationships between Particulate

Matter, Ozone, and Nitrogen Oxides during Urban Smoke Events in the Western US. *Environmental Science and Technology*, *53*(21), 12519–12528. https://doi.org/10.1021/ACS.EST.9B05241/SUPPL_FILE/ES9B05241_SI_001.PDF

Castellanos, P., Boersma, K. F., & Van Der Werf, G. R. (2014). Satellite observations indicate substantial spatiotemporal variability in biomass burning NOx emission factors for South America. *Atmospheric Chemistry and Physics*, *14*(8), 3929–3943. https://doi.org/10.5194/acp-14-3929-2014

Chen, J., Li, C., Ristovski, Z., Milic, A., Gu, Y., Islam, M. S., et al. (2017, February 1). A review of biomass burning: Emissions and impacts on air quality, health and climate in China. *Science of the Total Environment*. Elsevier B.V. https://doi.org/10.1016/j.scitotenv.2016.11.025

Dennison, P. E., Brewer, S. C., Arnold, J. D., & Moritz, M. A. (2014). Large wildfire trends in the western United States, 1984–2011. *Geophysical Research Letters*, *41*(8), 2928–2933. https://doi.org/10.1002/2014GL059576

Elshorbany, Y. F., Kurtenbach, R., Wiesen, P., Lissi, E., Rubio, M., Villena, G., et al. (2009). *Oxidation capacity of the city air of Santiago, Chile*. *Atmos. Chem. Phys* (Vol. 9). Retrieved from www.atmos-chem-phys.net/9/2257/2009/

Flannigan, M., Cantin, A. S., De Groot, W. J., Wotton, M., Newbery, A., & Gowman, L. M. (2013). Global wildland fire season severity in the 21st century. *Forest Ecology and Management*, *294*, 54–61. https://doi.org/10.1016/J.FORECO.2012.10.022

Garcia-Hurtado, E., Pey, J., Borrás, E., Sánchez, P., Vera, T., Carratalá, A., et al. (2014). Atmospheric PM and volatile organic compounds released from Mediterranean shrubland wildfires. *Atmospheric Environment*, *89*, 85–92. https://doi.org/10.1016/j.atmosenv.2014.02.016

George, C., Strekowski, R. S., Kleffmann, J., Stemmler, K., & Ammann, M. (2005). Photoenhanced uptake of gaseous NO2 on solid organic compounds: a photochemical source of HONO? *Faraday Discussions*, *130*(0), 195–210. https://doi.org/10.1039/B417888M

Han, C., Yang, W., Wu, Q., Yang, H., & Xue, X. (2016). Heterogeneous Photochemical Conversion of NO2 to HONO on the Humic Acid Surface under Simulated Sunlight. *Environmental Science and Technology*, *50*(10), 5017–5023. https://doi.org/10.1021/ACS.EST.5B05101/SUPPL_FILE/ES5B05101_SI_001.PDF

Harris, G. W., Carter, W. P. L., Winer, A. M., Pitts, J. N., Platt, U., & Perner, D. (1982). Observations of nitrous acid in the Los Angeles atmosphere and implications for predictions of ozone-precursor relationships. *Environmental Science & Technology*, *16*(7), 414–419. https://doi.org/10.1021/es00101a009

Hodshire, A. L., Akherati, A., Alvarado, M. J., Brown-Steiner, B., Jathar, S. H., Jimenez, J. L., et al. (2019, April 29). Aging Effects on Biomass Burning Aerosol Mass and Composition: A Critical Review of Field and Laboratory Studies. *Environmental Science and Technology*. American Chemical Society. https://doi.org/10.1021/acs.est.9b02588

Jaffe, D. A., & Wigder, N. L. (2012, May 1). Ozone production from wildfires: A critical review. *Atmospheric Environment*. Pergamon. https://doi.org/10.1016/j.atmosenv.2011.11.063

Jin, X., Zhu, Q., Cohen, R. C., & Xiaomeng, J. (2021). Direct estimates of biomass burning NO x emissions and lifetimes using daily observations from TROPOMI. *Atmos. Chem. Phys*, *21*, 15569–15587. https://doi.org/10.5194/acp-21-15569-2021

Jolly, W. M., Cochrane, M. A., Freeborn, P. H., Holden, Z. A., Brown, T. J., Williamson, G. J.,

& Bowman, D. M. J. S. (2015). Climate-induced variations in global wildfire danger from 1979 to 2013. *Nature Communications*, *6*. https://doi.org/10.1038/NCOMMS8537

Juncosa Calahorrano, J. F., Lindaas, J., O'Dell, K., Palm, B. B., Peng, Q., Flocke, F., et al. (2020). Daytime Oxidized Reactive Nitrogen Partitioning in Western U.S. Wildfire Smoke Plumes. *Journal of Geophysical Research: Atmospheres*, e2020JD033484. https://doi.org/10.1029/2020JD033484

Kasischke, E. S., & Turetsky, M. R. (2006). Recent changes in the fire regime across the North American boreal region—Spatial and temporal patterns of burning across Canada and Alaska. *Geophysical Research Letters*, *33*(9). https://doi.org/10.1029/2006GL025677

Kleffmann, J., Becker, K. H., Lackhoff, M., & Wiesen, P. (1999). Heterogeneous conversion of NO2 on carbonaceous surfaces. *Physical Chemistry Chemical Physics*, *1*(24), 5443–5450. https://doi.org/10.1039/A905545B

Kleffmann, J., Kurtenbach, R., Lörzer, J., Wiesen, P., Kalthoff, N., Vogel, B., & Vogel, H. (2003). Measured and simulated vertical profiles of nitrous acid—Part I: Field measurements. *Atmospheric Environment*, *37*(21), 2949–2955. https://doi.org/10.1016/S1352-2310(03)00242-5

Li, S., Matthews, J., & Sinha, A. (2008). Atmospheric hydroxyl radical production from electronically excited NO 2 and H2O. *Science*, *319*(5870), 1657–1660. https://doi.org/10.1126/SCIENCE.1151443/SUPPL_FILE/LI.SOM.PDF

Li, X., Rohrer, F., Hofzumahaus, A., Brauers, T., Häseler, R., Bohn, B., et al. (2014). Missing gas-phase source of HONO inferred from Zeppelin measurements in the troposphere. *Science*, *344*(6181), 292–296. https://doi.org/10.1126/SCIENCE.1248999/SUPPL_FILE/LI_SM.PDF

Lindaas, J., Pollack, I. B., Garofalo, L. A., Pothier, M. A., Farmer, D. K., Kreidenweis, S. M., et al. (2021). Emissions of Reactive Nitrogen From Western U.S. Wildfires During Summer 2018. *Journal of Geophysical Research: Atmospheres*, *126*(2), e2020JD032657. https://doi.org/10.1029/2020JD032657

Liu, J. C., Wilson, A., Mickley, L. J., Dominici, F., Ebisu, K., Wang, Y., et al. (2017). Wildfire-specific fine particulate matter and risk of hospital admissions in urban and rural counties. *Epidemiology*, *28*(1), 77–85. https://doi.org/10.1097/EDE.0000000000000556

Liu, X., Huey, L. G., Yokelson, R. J., Selimovic, V., Simpson, I. J., Müller, M., et al. (2017). Airborne measurements of western U.S. wildfire emissions: Comparison with prescribed burning and air quality implications. *Journal of Geophysical Research*, *122*(11), 6108–6129. https://doi.org/10.1002/2016JD026315

Liu, Y., Goodrick, S., & Heilman, W. (2014). Wildland fire emissions, carbon, and climate: Wildfire-climate interactions. *Forest Ecology and Management*, *317*, 80–96. https://doi.org/10.1016/j.foreco.2013.02.020

Liu, Z., Wang, Y., Gu, D., Zhao, C., Huey, L. G., Stickel, R., et al. (2012). Summertime photochemistry during CAREBeijing-2007: RO x budgets and O 3 formation. *Atmos. Chem. Phys*, *12*, 7737–7752. https://doi.org/10.5194/acp-12-7737-2012

Lu, K., Zhang, Y., Su, H., Brauers, T., Chou, C. C., Hofzumahaus, A., et al. (2010). Oxidant (O3 + NO2) production processes and formation regimes in Beijing. *Journal of Geophysical Research: Atmospheres*, *115*(D7), 7303. https://doi.org/10.1029/2009JD012714

McKendry, I., Strawbridge, K., Karumudi, M. L., O'Neill, N., Macdonald, A. M., Leaitch, R., et al. (2011). Californian forest fire plumes over Southwestern British Columbia: lidar, sunphotometry, and mountaintop chemistry observations. *Atmospheric*

Chemistry and Physics, *11*(2), 465–477. https://doi.org/10.5194/acp-11-465-2011

Mebust, A. K., Russell, A. R., Hudman, R. C., Valin, L. C., & Cohen, R. C. (2011). Characterization of wildfire NOx emissions using MODIS fire radiative power and OMI tropospheric NO2 columns. *Atmospheric Chemistry and Physics*, *11*(12), 5839–5851. https://doi.org/10.5194/acp-11-5839-2011

Monge, M. E., D'Anna, B., Mazri, L., Giroir-Fendler, A., Ammann, M., Donaldson, D. J., & George, C. (2010). Light changes the atmospheric reactivity of soot. *Proceedings of the National Academy of Sciences*, *107*(15), 6605–6609. https://doi.org/10.1073/PNAS.0908341107

Morris, G. A., Hersey, S., Thompson, A. M., Pawson, S., Nielsen, J. E., Morris, G. A., et al. (2006). Alaskan and Canadian forest fires exacerbate ozone pollution over Houston, Texas, on 19 and 20 July 2004. *J. Geophys. Res*, *111*, 24–27. https://doi.org/10.1029/2006JD007090

Müller, M., Anderson, B. E., Beyersdorf, A. J., Crawford, J. H., Diskin, G. S., Eichler, P., et al. (2016). In situ measurements and modeling of reactive trace gases in a small biomass burning plume. *Atmospheric Chemistry and Physics*, *16*(6), 3813–3824. https://doi.org/10.5194/acp-16-3813-2016

O'Dell, K., Hornbrook, R. S., Permar, W., Levin, E. J. T., Garofalo, L. A., Apel, E. C., et al. (2020). Hazardous Air Pollutants in Fresh and Aged Western US Wildfire Smoke and Implications for Long-Term Exposure. *Environmental Science and Technology*, *54*(19), 11838–11847. https://doi.org/10.1021/ACS.EST.0C04497/SUPPL_FILE/ES0C04497_SI_002.XLS

Oltmans, S. J., Lefohn, A. S., Harris, J. M., Tarasick, D. W., Thompson, A. M., Wernli, H., et al. (2010). Enhanced ozone over western North America from biomass burning in Eurasia during April 2008 as seen in surface and profile observations. *Atmospheric Environment*, *44*(35), 4497–4509. https://doi.org/10.1016/j.atmosenv.2010.07.004

Palm, B. B., Peng, Q., Fredrickson, C. D., Lee, B. H., Garofalo, L. A., Pothier, M. A., et al. (2020). Quantification of organic aerosol and brown carbon evolution in fresh wildfire plumes. *Proceedings of the National Academy of Sciences of the United States of America*, *117*(47), 29469–29477. https://doi.org/10.1073/pnas.2012218117

Parrington, M., Palmer, P. I., Lewis, A. C., Lee, J. D., Rickard, A. R., Carlo, P. Di, et al. (2013). Sciences ess Atmospheric Chemistry and Physics Climate of the Past Geoscientific Instrumentation Methods and Data Systems Ozone photochemistry in boreal biomass burning plumes. *Atmos. Chem. Phys*, *13*, 7321–7341. https://doi.org/10.5194/acp-13-7321-2013

Pfister, G. G., Emmons, L. K., Hess, P. G., Honrath, R., Lamarque, J.-F., Val Martin, M., et al. (2006). Ozone production from the 2004 North American boreal fires. *Journal of Geophysical Research*, *111*(D24), D24S07. https://doi.org/10.1029/2006JD007695

Robinson, M. A., Decker, Z. C. J., Barsanti, K. C., Coggon, M. M., Flocke, F. M., Franchin, A., et al. (2021). Variability and Time of Day Dependence of Ozone Photochemistry in Western Wildfire Plumes. *Environmental Science and Technology*, *55*(15), 10280–10290. https://doi.org/10.1021/ACS.EST.1C01963/SUPPL_FILE/ES1C01963_SI_001.PDF

Rosenfeld, D., Lohmann, U., Raga, G. B., O'Dowd, C. D., Kulmala, M., Fuzzi, S., et al. (2008). Flood or drought: How do aerosols affect precipitation? *Science*. https://doi.org/10.1126/science.1160606

Selimovic, V., Yokelson, R. J., Warneke, C., Roberts, J. M., De Gouw, J., Reardon, J., &

Griffith, D. W. T. (2018). Aerosol optical properties and trace gas emissions by PAX and OP-FTIR for laboratory-simulated western US wildfires during FIREX. *Atmos. Chem. Phys*, *18*, 2929–2948. https://doi.org/10.5194/acp-18-2929-2018

Singh, H. B., Cai, C., Kaduwela, A., Weinheimer, A., & Wisthaler, A. (2012). Interactions of fire emissions and urban pollution over California: Ozone formation and air quality simulations. *Atmospheric Environment*, *56*, 45–51. https://doi.org/10.1016/j.atmosenv.2012.03.046

Sörgel, M., Trebs, I., Serafimovich, A., Moravek, A., Held, A., & Zetzsch, C. (2011). Simultaneous HONO measurements in and above a forest canopy: Influence of turbulent exchange on mixing ratio differences. *Atmospheric Chemistry and Physics*, *11*(2), 841–855. https://doi.org/10.5194/ACP-11-841-2011

Stemmler, K., Ammann, M., Donders, C., Kleffmann, J., & George, C. (2006). Photosensitized reduction of nitrogen dioxide on humic acid as a source of nitrous acid. *Nature 2006 440:7081*, *440*(7081), 195–198. https://doi.org/10.1038/nature04603

Stocker, M., Ladstädter, F., & Steiner, A. K. (2021). Observing the climate impact of large wildfires on stratospheric temperature. *Scientific Reports*, *11*(1). https://doi.org/10.1038/S41598-021-02335-7

Stutz, J., Alicke, B., & Neftel, A. (2002). Nitrous acid formation in the urban atmosphere: Gradient measurements of NO2 and HONO over grass in Milan, Italy. *Journal of Geophysical Research: Atmospheres*, *107*(D22), LOP 5-1. https://doi.org/10.1029/2001JD000390

Su, H., Cheng, Y. F., Shao, M., Gao, D. F., Yu, Z. Y., Zeng, L. M., et al. (2008). Nitrous acid (HONO) and its daytime sources at a rural site during the 2004 PRIDE-PRD experiment in China. *Journal of Geophysical Research Atmospheres*, *113*(14), 14312. https://doi.org/10.1029/2007JD009060

Tan, Z., Lu, K., Hofzumahaus, A., Fuchs, H., Bohn, B., Holland, F., et al. (2019). Experimental budgets of OH, HO_2, and RO_2 radicals and implications for ozone formation in the Pearl River Delta in China 2014. *Atmospheric Chemistry and Physics*, *19*(10), 7129–7150. https://doi.org/10.5194/acp-19-7129-2019

Theys, N., Volkamer, R., Müller, J. F., Zarzana, K. J., Kille, N., Clarisse, L., et al. (2020). Global nitrous acid emissions and levels of regional oxidants enhanced by wildfires. *Nature Geoscience*, *13*(10), 681–686. https://doi.org/10.1038/S41561-020-0637-7

Urbanski, S. (2014). Wildland fire emissions, carbon, and climate: Emission factors. *Forest Ecology and Management*, *317*, 51–60. https://doi.org/10.1016/j.foreco.2013.05.045

Veres, P., Roberts, J. M., Burling, I. R., Warneke, C., de Gouw, J., & Yokelson, R. J. (2010). Measurements of gas-phase inorganic and organic acids from biomass fires by negative-ion proton-transfer chemical-ionization mass spectrometry. *Journal of Geophysical Research*, *115*(D23), D23302. https://doi.org/10.1029/2010JD014033

Verma, S., Worden, J., Pierce, B., Jones, D. B. A., Al-Saadi, J., Boersma, F., et al. (2009). Ozone production in boreal fire smoke plumes using observations from the Tropospheric Emission Spectrometer and the Ozone Monitoring Instrument. *Journal of Geophysical Research*, *114*(D2), D02303. https://doi.org/10.1029/2008JD010108

Volkamer, R., Sheehy, P., Molina, L. T., & Molina, M. J. (2010). Oxidative capacity of the Mexico City atmosphere-Part 1: A radical source perspective. *Atmos. Chem. Phys*, *10*, 6969–6991. https://doi.org/10.5194/acp-10-6969-2010

Westerling, A. L., Hidalgo, H. G., Cayan, D. R., & Swetnam, T. W. (2006). Warming and earlier spring increase Western U.S. forest wildfire activity. *Science*, *313*(5789), 940–943.

https://doi.org/10.1126/SCIENCE.1128834/SUPPL_FILE/WESTERLING.SOM.PDF
Ye, C., Zhou, X., Pu, D., Stutz, J., Festa, J., Spolaor, M., et al. (2016). Rapid cycling of reactive nitrogen in the marine boundary layer. *Nature*, *532*(7600), 489–491. https://doi.org/10.1038/nature17195
Ye, C., Zhou, X., Pu, D., Stutz, J., Festa, J., Spolaor, M., et al. (2018). Tropospheric HONO distribution and chemistry in the southeastern US. *Atmos. Chem. Phys*, *18*, 9107–9120. https://doi.org/10.5194/acp-18-9107-2018
Yokelson, R. J., Karl, T., Artaxo, P., Blake, D. R., Christian, T. J., Griffith, D. W. T., et al. (2007). The tropical forest and fire emissions experiment: Overview and airborne fire emission factor measurements. *Atmospheric Chemistry and Physics*, *7*(19), 5175–5196. https://doi.org/10.5194/acp-7-5175-2007
Yokelson, R. J., Andreae, M. O., & Akagi, S. K. (2013). Pitfalls with the use of enhancement ratios or normalized excess mixing ratios measured in plumes to characterize pollution sources and aging. *Atmospheric Measurement Techniques*, *6*(8), 2155–2158. https://doi.org/10.5194/amt-6-2155-2013
Zhang, R., Sarwar, G., Fung, J. C. H., Lau, A. K. H., & Zhang, Y. (2012). Examining the impact of nitrous acid chemistry on ozone and PM over the pearl river delta region. *Advances in Meteorology*, *2012*. https://doi.org/10.1155/2012/140932
Zhao, B., Zhuang, Q., Shurpali, N., Köster, K., Berninger, F., & Pumpanen, J. (2021). North American boreal forests are a large carbon source due to wildfires from 1986 to 2016. *Scientific Reports*, *11*(1). https://doi.org/10.1038/S41598-021-87343-3
Zhou, X., Beine, H. J., Honrath, R. E., Fuentes, J. D., Simpson, W., Shepson, P. B., & Bottenheim, J. W. (2001). Snowpack photochemical production of HONO: A major source of OH in the Arctic boundary layer in springtime. *Geophysical Research Letters*, *28*(21), 4087–4090. https://doi.org/10.1029/2001GL013531
Zhou, X., He, Y., Huang, G., Thornberry, T. D., Carroll, M. A., & Bertman, S. B. (2002). Photochemical production of nitrous acid on glass sample manifold surface. *Geophysical Research Letters*, *29*(14), 26–1. https://doi.org/10.1029/2002GL015080
Zhou, X., Gao, H., He, Y., Huang, G., Bertman, S. B., Civerolo, K., & Schwab, J. (2003). Nitric acid photolysis on surfaces in low-NOx environments: Significant atmospheric implications. *Geophysical Research Letters*, *30*(23), 2217. https://doi.org/10.1029/2003GL018620

CHAPTER 2. HONO EMISSIONS FROM WESTERN US WILDFIRES PROVIDE DOMINANT RADICAL SOURCE IN FRESH WILDFIRE SMOKE[1]

2.1 INTRODUCTION

Nitrous acid (HONO) is emitted directly into the atmosphere through various combustion processes, from vehicle exhaust (Li et al., 2008) to biomass burning (Keene et al., 2006). As a source of both hydroxyl radicals (OH) and nitrogen oxides (NO_x = NO + NO_2), HONO emissions can have a significant impact on the atmosphere's oxidizing capacity (Elshorbany et al., 2009).

During biomass burning, biomass nitrogen is combusted to form a range of inorganic and organic N containing species, such as HCN, HNCO, HONO, NO, NO_2, N_2O, N_2, etc. The speciation among these various forms at the source remains actively researched (Chen et al., 2007; Koppmann et al., 2005). In laboratory studies of biomass burning, Veres et al. (2010) observed HONO to carbon monoxide (CO) emission ratios between 1.2 and 4.6 pptv $ppbv^{-1}$ depending on the fuel type. Yokelson et al. (2007) observed direct emissions of HONO with a study-average HONO to CO emission ratio of 1.5 pptv $ppbv^{-1}$ from pasture fires during the Amazon dry season. Stockwell et al. (2014) determined the overall HONO to CO emission ratio to be 0.26 pptv $ppbv^{-1}$ in regional Indonesian peat fires during the FLAME-4 laboratory experiments.

In wildland fire plumes, the fate and importance of HONO is influenced by fuel characteristics (e.g. moisture and N content), combustion conditions, sunlight, smoke plume

[1] Reprinted with permission from Peng, Q., Palm, B. B., Melander, K. E., Lee, B. H., Hall, S. R., Ullmann, K., et al. (2020). HONO Emissions from Western U.S. Wildfires Provide Dominant Radical Source in Fresh Wildfire Smoke. *Environmental Science and Technology*, *54*(10), 5954–5963. https://doi.org/10.1021/acs.est.0c00126 Copyright 2020 American Chemical Society

opacity, cloud cover, and dilution rates (Akagi et al., 2012). Photolysis is expected to be the dominant daytime loss pathway for HONO with a lifetime of 10-20 minutes at midday and unit quantum yield to OH and NO (Barney et al., 2000; W. R. Stockwell & Calvert, 1978). Previous *in situ* HONO measurements in biomass burning plumes were largely confined to prescribed fires, aged smoke far from the source, or outside of the typical western U.S. fire season (Akagi et al., 2011; May et al., 2015; R. J. Yokelson et al., 2008). While laboratory studies are useful for characterizing the initial conditions of wildfire emissions, they cannot replicate the variable and changing combustion conditions of wildfires, particularly for species as short-lived as HONO. Fuels are typically heterogeneous in composition and burn unevenly, creating variable plume heights and smoke transport at different phases of combustion (Liu et al., 2012). Moreover, atmospheric and ecosystem conditions prior to and during fires affect burning conditions and fuel moisture content, which in turn affect emissions.

Uncertainties in HONO primary emissions limit the ability to understand and simulate photochemical production of O_3 and secondary aerosol within wildfire plumes. Several prognostic models of biomass burning plumes have found that inclusion of additional HONO emissions accelerates initial plume chemistry and improves the agreement between simulated and measured O_3 production (Alvarado et al., 2009; Alvarado & Prinn, 2009; Trentmann et al., 2005). Thus, more detailed information on primary HONO emissions at the source level is essential for simulating fire-generated HONO and subsequent photochemical impacts.

Herein, we use *in situ* measurements collected from the NCAR/NSF C-130 aircraft during the Western Wildfire Experiment for Cloud chemistry, Aerosol absorption and Nitrogen (WE-CAN) campaign, which was carried out in summer 2018 in the western U.S., to examine HONO and associated trace gases in fresh smoke plumes from large wildfires. Several fire plumes with

known source locations and fuel types were sampled in a pseudo-Lagrangian approach, which proved useful for the study of near-source HONO and its impact on subsequent gas-phase photochemistry in plumes with physical ages from less than half an hour to greater than 5 hours for the same fire. Moreover, the number of distinct fires sampled allow us to evaluate potential drivers of variability in HONO emissions.

2.2 WE-CAN CAMPAIGN OVERVIEW AND INSTRUMENTATION

The WE-CAN campaign took place from 22 July to 14 September 2018. The research aircraft was based in Boise, ID from 24 July to 31 August 2018, and this period is the focus of our paper. More detail on the campaign can be found in the Supplemental Information (SI). Here we focus on observations collected by the University of Washington (UW) High Resolution Time of Flight Chemical Ionization Mass Spectrometer (HRToF-CIMS). Measurements of other relevant species and parameters by different instruments on board are summarized in Table S2.1.

The HRToF-CIMS with iodide (I^-) adduct ionization was employed as described in detail previously (Lee et al., 2014, 2018), and in the SI, with the main modification being the use of a sheath-flow facilitated, coaxial IMR region (Palm et al., 2019). Under laminar flow conditions, only 25% of gases are expected to diffuse to the inlet wall and back to the center of the flow from which we sample into the ion-molecule reaction (IMR) region. Background signals were measured every 60 seconds by overflowing the IMR sampling orifice with ultra-high purity (UHP) N_2 for 6 s as described previously (Lee et al., 2018; Palm et al., 2019). The sampling inlet was also overflowed with UHP N_2 during flight every 20 min for 12 s. To prevent titration of reagent ions and thus nonlinear responses in wildfire plumes, the sample flow entering the IMR was diluted as needed with a known flow rate of UHP N_2 to maintain constant reagent ion count rates.

We calibrated the HRToF-CIMS response to HONO, and a range of other trace gases (Table S2.2) before and after the campaign, and tied the calibration to HCN, Cl_2, and HCOOH standards used to monitor relative changes in instrument sensitivity. We generated HONO following a modified version of the method in Febo et al. (1995), flowing the headspace of dilute aqueous HCl across a fresh $NaNO_2$ salt bed to promote the reaction

$$HCl(g) + NaNO_2(s) \rightarrow NaCl(s) + HONO(g) \qquad (2.1)$$

HONO output from R1 is variable in time, depending on HCl flow rate, relative humidity, as well as the extent of physical transformations of the $NaNO_2$ [22]. We therefore simultaneously measured the output utilizing an independently calibrated total reactive nitrogen (NO_y) instrument operating a heated molybdenum catalyst coupled to a chemiluminescence NO analyzer. We also bubbled the output into vials containing a Griess reagent (sulfanilic acid and 2-naphthylamine in dilute acetic acid) which reacts with NO_2^- in solution to form a visible light-absorbing compound. The vials were then analyzed by UV-Vis absorbance at 528 nm as commonly done for aquatic NO_2^-/HONO measurements following Xue et al. (2012). The two calibration approaches resulted in the same HONO calibration factor to within combined uncertainties, of 2.1 ± 0.6 counts per second/pptv HONO/10^6 counts per second of reagent ions, which also agrees well with our independently determined value used for the previous WINTER campaign (Lee et al., 2018; Palm et al., 2019). More details on HONO calibration and interference checks, such as from $H^{13}COOH$ and NO_2 reactions on inlet surfaces, can be found in the SI (Figures S1 and S2).

Maps of WE-CAN research flights are shown colored by mixing ratios of HCN (Figure 2.1) and HONO (Figure S2.3) measured by the HRToF-CIMS. Altogether 258 fire plumes were sampled across the 16 research flights (RFs). Most flights took off at approximately 14:00 local

time ± 1 hour, with a flight duration of approximately 6 hours. More information can be found at https://www.eol.ucar.edu/field_projects/we-can.

2.3 Results and Discussion

2.3.1 Primary HONO emissions

In Figure 2.1, we show the average of HONO and CO concentrations, normalized to their respective maximum mixing ratios, measured during the horizontal transects of 18 fire plumes. For each plume intercept, prior to normalizing by the maximum, we subtracted the respective "background ambient" concentration to determine the plume enhancement, where the median of 20 seconds of ambient abundances just prior to intercepting the plume are used as the background. We have divided the intercepts into "near-field" and "far-field" representing how far downwind from the fire the plume was sampled and thus how long the smoke has been in the atmosphere. The threshold for physical "age" (see SI) of the near-field intercepts is < 40 min, while > 1 hour for those in the far field. The insets show the absolute mixing ratios measured during typical fresh and aged plume intercepts for HONO and CO.

From these plume intercepts, we wish to calculate the normalized excess mixing ratio (NEMR), also called enhancement ratio (EnR), which has been widely adopted to connect smoke plume observations to fire emissions (Briggs et al., 2016; R. J. Yokelson et al., 2013). It is defined as

$$NEMR_X = \Delta X/\Delta Y = (X_{plume} - X_{bkg})/(Y_{plume} - Y_{bkg}) \qquad (2.2)$$

where ΔX and ΔY are the absolute excess concentration of target species X and reference species Y relative to the ambient background, respectively. Reference species Y is used to account for plume dilution by entrainment of background air in the near field, and has most commonly been CO, given its slow chemistry.

We evaluated the various choices for determining NEMR, such as the ratio of maximum concentration enhancements in the plume, the ratio of integrals of concentrations across the entire plume(Karl et al., 2007), and the slope of linear least square fits of ΔX versus ΔY. We chose to use the ratio of maximum concentration enhancements (see SI), because of the expected short photolytic lifetime of HONO in the atmosphere. As illustrated in Figure 2.1b and 2.1c, HONO plume transects are narrower than CO, and the difference in width becomes more prominent as the plume ages downwind. As the plume ages, it is turbulently diffusing and thus spreading in spatial extent, as indicated by the wider CO transects in the far-field compared to the near-field. HONO transects, in contrast, become if anything narrower in the far-field compared to the near-field, and oppositely compared to those of CO. As discussed more fully below, this trend is largely driven by the changing HONO photolysis frequency along the plume transect (Figure S2.4), and is indicative that HONO emitted by the fire is being lost relative to the emitted CO during transport (as expected).

At the plume edges, mixing of the smoke plume with cleaner background air leads to less aerosol light extinction and thus faster HONO photolysis. In addition, at the top of the plume, photolysis rates are actually enhanced by scattering from the plume below. Not only do these behaviors imply a complex 3-D variation in the chemical processing of fresh wildfire plumes, with both dilution and photochemistry enhanced at the plume edges (Garofalo et al., 2019), but they also suggest that using linear fits of □HONO to □CO across the plume intercept, plume-average concentrations, or even integrals over the plume intercepts would bias $NEMR_{HONO}$ low. Similarly, low time resolution observations of HONO (e.g. < 1 Hz) would also bias estimates of HONO emission ratios low if the role of edge effects on HONO abundances were not taken into account. Using only the top 5% of 1Hz HONO concentrations within a plume intercept are thus our best

attempt to address this bias by focusing more towards the central, optically thicker, part of plumes, but measurements at any point downwind of the fire will be potentially biased by HONO losses.

The emission ratio (ER) is a special case of the NEMR, which is reserved for measurements taken at the source, i.e., in the freshest smoke plumes (Yokelson et al., 1999), and is more of a characteristic of fuel type and burning conditions, while NEMR may undergo substantial changes downwind of the source due to differential dilution, chemistry, and deposition. In the following discussions, we report $NEMR_{HONO}$ determined within 1 hour of smoke emissions as approximations to its ER for consistency with previous methods (Garofalo et al., 2019), and evaluate factors affecting its variability. Given HONO's short photolytic lifetime, we thus expect our NEMR to be lower limits to the ER.

Figure 2.2 shows HONO to CO NEMR from the emission plume passes for 18 different fires sampled across 10 different flights during WE-CAN. We have also labeled each with a corresponding physical age estimate. As described above, the NEMRs in plumes with estimated physical ages less than 1 hour were assumed to represent the emission ratios for that species, relative to CO or NO_x. Ages of plumes clearly affected by more than 1 fire, e.g., as determined by satellite observations and in-flight observations, are considered unknown and excluded from this analysis. NEMRs computed using the entire plume integration method are shown in Figure S2.5 for comparison, and while broadly similar were consistently lower by an average of 40% for HONO to CO NEMR, and 29% for HONO to NO_x NEMR. Tables S2.3 and S2.4 list the quantification methods, ranges and other relevant information for HONO ER in the literature as well as in this study.

As indicated in Figure 2.2, HONO is present in substantial amounts in the early stages of most plumes, with HONO to CO ER spanning from 0.65 to 17.2 pptv $ppbv^{-1}$ (average 5.3 ± 5.2

pptv ppbv^{-1}). The high HONO ER inferred from some of the youngest plume intercepts highlights the importance of direct fire emissions to HONO abundances, and the overall large variations in HONO ERs suggest differences in meteorological conditions, fuel type, plume reactivity, location and distance from the source (Jaffe et al., 2013; R. J. Yokelson et al., 2013). Our range of HONO to CO NEMR covers values measured in past laboratory and field studies (Akagi et al., 2011; Burling et al., 2011; Koss et al., 2018; Müller et al., 2016; Veres et al., 2010; R. J. Yokelson et al., 2007) (see shading in Figure 2.2) that sampled fire emissions across several fuel types in the U.S., where the flaming stage HONO to CO NEMR range was reported as approximately 2 – 5 pptv ppbv^{-1}. The reported emission factors of HONO and CO in Akagi et al. (2011) imply that HONO to CO NEMRs range from 1.8 to 7.0 ppt·ppb^{-1} in temperate forests, while ranging from 5.9 to 10.7 pptv ppbv^{-1} in tropical forests, which are of the same magnitude as the highest HONO to CO NEMR observed during WE-CAN. Later, Akagi et al. (2013) observed HONO to CO ER of 4.00 ± 0.61 pptv ppbv^{-1} emitted by a prescribed fire in chaparral fuels in California. Neuman et al. (2016) determined that the HONO to CO ratio ranged from 1.3 to 5.2 pptv ppbv^{-1} in flaming stage fires using airborne measurements over the Southeast U.S. at night. For added context, study-wide HONO NEMRs across different age ranges are shown in Figure S2.6.

To assess whether fire-to-fire differences in the HONO to CO NEMR are caused by the variable nitrogen content of fuels, it is useful to compare ΔHONO to ΔNO_x, which is also emitted during the flaming phase (Burling et al., 2010). The observed HONO to NO_x ER during WE-CAN ranged from 0.25 to 1.4 pptv pptv^{-1} (average 0.72 ± 0.34 pptv pptv^{-1}), for fires sampled 10 – 33 km downwind (corresponding to 0.3 – 1.0 h transport after emission), as shown in Figure 2.2. For added context, Figure S2.7 shows scatter plots of HONO to CO and NO_x for the closest plume transect in each fire during the campaign.

Our $\Delta HONO/\Delta NO_x$ ERs clearly lie above most previous determinations. Trentmann et al. (2005) first described significant HONO emissions at ~0.03 pptv pptv^{-1} to NO_x in a savanna fire. Later, Keene et al. (2006) measured $\Delta HONO/\Delta NO_x$ values ranging from 0.048 to 0.23 pptv pptv^{-1} for different Southern African biomass samples in the laboratory. Yokelson et al. (2007) reported $\Delta HONO/\Delta NO_x$ of ~0.14 pptv pptv^{-1} from Brazilian pasture fires. Akagi et al. (2013) observed $\Delta HONO/\Delta NO_x$ molar ratios spanning from 0.16 to 0.33 pptv pptv^{-1} in South Carolina biomass burning plumes. Chai et al. (2019) determined an overall range of $HONO/NO_x$ ratio from 0.13 to 0.53 pptv pptv^{-1} for fresh emissions of 20 laboratory fires of different fuels. The laboratory studies by Burling et al. (2010) found the fire-integrated molar emission ratios of HONO relative to NO_x ranged from approximately 0.03 to 0.20 pptv pptv^{-1}, with higher values observed for southeastern fuels, while later airborne measurements from prescribed burning in southwestern U.S. by Burling et al. (2011) revealed systematically higher $\Delta HONO/\Delta NO_x$ molar ratios spanning from 0.077 to 0.22 pptv pptv^{-1}. Stockwell et al. (2014) reported the $\Delta HONO/\Delta NO_x$ ratio was ~0.13 pptv pptv^{-1} in cooking fires through a series of laboratory measurements. Selimovic et al. (2018) detected a HONO to NO_x NEMR of 0.9 pptv pptv^{-1} from an Engelmann spruce canopy fire burned in the FIREX Fire Lab experiments, while reporting a study average $\Delta HONO/\Delta NO_x$ of 0.21 ± 0.13 from various fuel types, suggesting fresh, moister conifer-canopy fuels may drive higher HONO to NO_x NEMR.

The collective range of ~0.03 – 0.9 pptv pptv^{-1} in the HONO to NO_x NEMRs assembled from these prior studies implies high fire-to-fire variability in HONO emissions, not just from burning conditions, but also from fuel type and fuel characteristics such as moisture and nitrogen content (Akagi et al., 2012; Burling et al., 2010; Keene et al., 2006). Additional factors that can affect reported HONO to NO_x and HONO to CO NEMRs include HONO photochemistry after

emission and measurement artifacts. Previous field measurements were mostly carried out in well-mixed plumes that had photolysis conditions close to clear sky. The large differences compared to previous measurements may reflect WE-CAN's overall higher sampling frequency closer to fire sources, where the more rapid post-emission loss of HONO compared to NO_x, as illustrated by the differences between Figure S2.2b and S2.2c, is less significant. The relative change of HONO to NO_x following emission is smaller than the corresponding change in HONO to CO over the same timescale, given that CO remains constant aside from dilution, while NO_x and HONO both dilute and react, so these photochemical effects are not necessarily able to explain all the differences in the HONO to NO_x NEMRs. It is not clear to what extent past measurements of NO_x were contaminated by HONO (or vice versa). For example, NO_x is often measured by catalytic conversion of NO_2 to NO as well as photolytic conversion with wavelengths < 400 nm which will also convert some fraction of HONO to NO, biasing the reported HONO to NO_x NEMR low. Non-intrusive measurements like Fourier transform infrared spectrometers (FT-IR), used for some of the previous studies allow simultaneous detection of many different species including HONO and NO_x, and is likely free of artifacts resulting from HONO conversion to NO_x (Akagi et al., 2011; Selimovic et al., 2018; R. J. Yokelson et al., 2007). The NO_2 measurement made during WE-CAN used photolysis by LED having output optimized to 398 nm, with half power reached at ± 6 nm, implying minimal HONO conversion. The large variability in $\Delta HONO/\Delta NO_x$ within WE-CAN, and the relatively small set of previous observations suggests that previous studies may simply not have sampled fires with the fuel nitrogen content, moisture content, Modified Combustion Efficiency (MCE), etc. of those sampled during WE-CAN. MCE is a proxy for the degree of flaming versus smoldering combustion:

$$\mathrm{MCE} = \frac{\Delta CO_2}{\Delta CO_2 + \Delta \mathrm{CO}} \qquad (2.3)$$

where ΔCO_2 and ΔCO are background-corrected mixing ratio enhancements of CO_2 and CO, respectively (Ward & Radke, 1993; Robert J. Yokelson et al., 1996).Thus, we conclude that there are large variations from fire to fire and across the fire season in HONO to NO_x emission ratios.

2.3.2 HONO evolution and contribution to radical chemistry

During WE-CAN, multiple fires were sampled in a pseudo-Lagrangian fashion, which allowed for investigations into the chemical evolution of the primary emissions downwind from the source. Figure 2.3 displays the study-wide HONO to CO NEMR evolution in the first few hours of aging, where the points are colored by the average HONO photolysis frequency (j_{HONO}) measured in each plume transect. The median HONO to CO NEMR of this sample population decays by more than 90% in less than 1 hour, which in turn suggests an e-folding time of about 20 minutes. An exponential fit (dashed red curve) to this observed decay in $\Delta HONO/\Delta CO$ yields a decay constant of 0.058 min^{-1} (with 95% confidence bounds 0.053 - 0.063), which is nearly identical to the median observed HONO j-value (0.057 min^{-1}). An offset of 0.096 pptv $ppbv^{-1}$ was included in the fit function so that the curve passes through all the data at higher plume ages. However, the physical meaning of this offset is unclear given that it implies HONO mixing ratios near or below our 1 Hz detection limit (~20 pptv) and so we refrain from interpreting what it implies in terms of potential HONO steady state in aged plumes.

The rapid decay of HONO in Figure 2.3 is a sign of its impact on chemical processing within the smoke plume and, as noted above, that the emission ratios relative to CO are likely biased low. The youngest plume ages in Figure 2.3 are ~ 20-30 min transport time from the source, equivalent to 1 to 2 photolysis lifetimes depending on plume *j*-values. Further downwind, where plume ages exceed 2 hours, HONO mixing ratios drop to tens of pptv, which are close to the CIMS detection limit for HONO and the ambient background mixing ratios, as shown in Figure S2.8.

Figure 2.3 suggests the possibility to correct the measured HONO NEMR to account for the HONO lost to photolysis. However, we do not have measurements closer to the source to constrain such an estimate. Given that closer to the fire, plume opacity is likely increasing substantially, and plume vertical motions become more important than the horizontal motions, which we use to estimate plume age, a simple exponential function to estimate HONO at t = 0 may lead to substantial error. Thus, our reported ER for HONO are likely lower limits, and could be larger (e.g., by factors of 2 or more), but by how much remains uncertain.

The photolysis of HONO yields OH radicals and NO. In Figure 2.4, we show that the photolysis of HONO dominates the primary HO_x (OH + HO_2) radical production over the first ~1.5 h of atmospheric transport in the wildfire plumes sampled during WE-CAN. We used campaign-wide in-plume observations to generate an observationally constrained estimate of the average primary radical source strength within plumes as a function of plume age as was done in an earlier study (Haskins et al., 2019):

$$\mathrm{P}(HO_X) = j_{HONO}[HONO] + 2j_{HCHO}[HCHO] + j_{CH_3CHO}[CH_3CHO] + \emptyset_{OH}j_{O^1D}[O_3] + \sum_i [O_3](k_i[alkene_i]) \quad (2.4)$$

More details are elaborated in the SI. HONO photolysis is the most important single primary source observed in fresh wildfire plumes, with maximum values close to 11 pptv s^{-1}. HONO contributes over 90% in plumes with age shorter than an hour, and accounts for approximately 27% of HO_x production even in plumes with physical ages of 3 hours. HCHO photolysis becomes more important in more aged plumes, but absolute radical production rates drop substantially after 1 hour, explaining in part the sustained relative contribution of HONO. O_3 photolysis is the third largest contributor overall to the total radical production rate within WE-CAN sampled plumes, but is most important in background air. The dominant role of HONO as the primary radical source,

and its relatively rapid decay, suggests that wildfire plumes are highly photochemically active in the first few hours after emission, and then become much less active, closer to background air, thereafter.

2.3.3 HONO NEMR Variability

In wildfires, a variety of nitrogen containing species are emitted, including ammonia (NH_3), HONO, NO_x, and hydrogen cyanide (HCN), acetonitrile (CH_3CN) and isocyanic acid (HNCO) (Urbanski, 2014; Veres et al., 2010). These nitrogenous gases are emitted to varying degrees depending on fuel and combustion conditions (Burling et al., 2011; Coggon et al., 2016). Rarely is it possible to directly measure the fuels consumed at each burning stage, thus we aim to develop an understanding from the WE-CAN campaign of what drives variability from fire to fire in the HONO emission relative to longer-lived trace gases such as CO and HCN.

Setting aside HONO photolysis as perhaps the dominant driver of HONO NEMR variability at any point downwind of a fire, we focus on relationships among various trace gases and combustion conditions measured as close to the fires as possible. HONO mixing ratios in more aged smoke can be quite low due to its fast decay; HONO can also be formed by multiphase processes (Ye et al., 2016) and thus measurements of plumes with older physical ages may not reflect direct emissions. Therefore, to analyze HONO emission characteristics, we focus on plume intercepts with physical age shorter than the instantaneous HONO photolysis lifetime to minimize the impact of HONO photolytic loss after emission on our conclusions.

The release of fuel nitrogen and its chemical speciation depends significantly on the heating rate and fuel rank, i.e., the relative amount of nitrogen contained in aromatic structures relative to that in amine structures (Leppälahti & Koljonen, 1995). At combustion temperatures over 1000 K, increased fuel rank tends to produce more HCN, while decreased fuel rank favors NH_3 formation.

These pyrolysis products then undergo further in-flame processing in the flaming stage (Sekimoto et al., 2018; Robert J. Yokelson et al., 1996). It is hypothesized that HONO emission results from conversion of NO or NO_2 in series depending on temperature in the vicinity of the flame, where fast oxidations of HCN and NH_3 also occur (Chai et al., 2019). Thus, HONO emissions are expected to anti-correlate with HCN and NH_3, as they are intermediate products that are being oxidized in the flame chemistry, while HONO emissions are expected to correlate with MCE and NO_x, corresponding to higher combustion temperatures which favor more oxidized nitrogen. MCE ranged from 0.86 to > 0.94 in WE-CAN, suggesting some of the fire to fire variation in our reported ERs results from burning conditions alone. For major wildfires covering large areas, flaming and smoldering may occur concurrently, similar to the condition where many different smaller fires burn at the same time (Akagi et al., 2011). The co-existence of two combustion phases is common in plumes sampled during WE-CAN, as reflected by a large number of MCEs between flaming and smoldering MCE cutoffs. That said, the effective MCE in a plume intercept explains some of the large variability in the HONO NEMRs (factor of ~10) across the various fires sampled during WE-CAN (Figure 2.5c). Similarly, $\Delta HONO/\Delta CO$ is negatively correlated with $\Delta NH_3/\Delta CO$ as well as with $(\Delta HCN+\Delta CH_3CN)/\Delta CO$ (Figure 2.5a and 2.5b); both these parameters are expected to be larger when flame temperatures are lower and at lower MCEs. Previous work showed that NH_3/NO_x molar ratio was negatively correlated with MCE for a range of fuels, and that the emission factor of NH_3 and HCN are anti-correlated with MCE (Burling et al., 2011; Goode et al., 1999, 2000; McMeeking et al., 2009). Others found that NO_x and HONO are positively correlated with MCE (Veres et al., 2010). Pyrolysis experiments with a series of biofuel model compounds reveal that the HNCO/HCN ratio is highly dependent on flame temperature while only slightly dependent on the type of compounds (Hansson et al., 2003, 2004). The emission of these species

as well as the relative partitioning between reduced and oxidized fuel nitrogen appears to depend on both fuel nitrogen content and MCE (Burling et al., 2011; Coggon et al., 2016), and are therefore potentially a good reference set for evaluating biomass burning conditions.

We define a broader metric, R_N, which is the ratio of reduced N to total N, except for HONO emitted (2.5). It serves as a proxy of fire temperature and oxidizing conditions, with lower values representing higher combustion temperatures and more oxidation.

$$R_N = \frac{HCN+CH_3CN+NH_x}{HCN+CH_3CN+NH_x+ HNCO+NO_x+(NO_z-HONO)} \quad (2.5)$$

NH_x is the sum of NH_3 and NH_4^+ in both phases, and NO_z represents oxidized reactive nitrogen species such as PAN and other organic nitrates, $2*N_2O_5$, and total (gas+particle) nitrate. Oxidation state aside, we did not include HNCO (in which N is thought to be reduced) in the numerator as it is relatively enhanced compared to HCN for higher combustion temperatures as shown previously (Scharko et al., 2019). R_N is highly correlated with our measured HONO enhancements (R^2 = 0.74), as shown in Figure 2.5d. It is likely a more stable metric for estimating HONO emissions when a lack of observations or plume age do not allow direct quantification of HONO release assuming dry deposition is not significant. For example, HONO is often not measured during wildfire smoke studies, or a smoke plume is sampled several hours or more downwind of the source, in which the majority of emitted HONO will have photolyzed. The relationships in Figure 2.5d provide a means of estimating what the emitted HONO was in such cases and therefore its contribution to the primary radical source during plume evolution.

2.4. Atmospheric Implications

The above results highlight the importance of wildfires as a primary HONO source over the Western U.S. in summer. To our knowledge, our study has reported the highest HONO

emission ratios in wildfire plumes. However, our HONO emission ratios are essentially convolutions of the initial emission and any post-emission processes (e.g., photolysis, radical recombination, multiphase chemistry) that may have taken place during plume transport and aging, and are thus potentially lower limits. The focus on fresh biomass burning plumes allowed us to observe how the starting chemistry varies with fuel nitrogen, combustion efficiency, and other trace gas emission, providing an additional constraint on the release of HONO. We show that HONO emissions scale with MCE as well as measures of fire temperature and oxidation conditions, likely reflecting that emissions of this species are driven by flaming combustion with high temperatures.

The HONO NEMRs presented here are likely critical to interpret the evolution of other trace gases and to initiate models intending to represent rapid oxidation within biomass burning plumes. While a complete assessment of plume radical chemistry is beyond the scope of this work, further investigations of the impact of these HONO emissions on downwind chemical evolution with a suite of models is warranted. Moreover, the variation of HONO photolysis frequencies and concentrations between the center and edges of the plumes that we observe suggests that a 3-D chemical plume model is ultimately needed for a complete description of smoke plume chemical evolution and dispersion.

2.5. Supplemental Information

2.5.1 UW HRToF-CIMS Operation

Ambient air was sampled at 20 volumetric liters per minute (LPM) through a ~50-cm long, 3/4" O.D. PTFE Teflon tube, at ambient pressure and temperature. The inlet tip was cut at a 45° angle to facilitate rejection of particles larger than ~ 300 nm from the inlet. A major modification prior to WE-CAN was the development and incorporation of a sheath-flow facilitated, coaxial

IMR region described (Palm et al., 2019). Ambient air was sampled at 20 standard liters per minute through a 40 cm length of 18 mm OD Teflon tubing, and subsampled from the center into the ion-molecule reaction (IMR) region. The residence time in the sampling inlet was thus < 0.6 s, and 0.1 s in the IMR (Palm et al., 2019). In brief, I^- ion generation, pressure, and background signal determination were identical to that described earlier (Lee et al., 2018), but ions and sample flow were parallel, and molecular diffusion, not turbulence, drove mixing of reagent ions and sample flow. Water vapor was continuously added to the IMR as described previously in order to minimize the effects of changing ambient water vapor concentrations on instrument sensitivity (Lee et al., 2018).

2.5.2 Operation of Other Instruments on Board

Measurements of NO, NO_2, NH_3, O_3, HCHO, CO, CO_2, photolysis frequencies based on *in-situ* spectral radiometer data, aerosol size distributions, wind speed and direction, T, P, and GPS position were provided by other instruments aboard the same aircraft. More details are listed in Table S2.1.

2.5.3 HONO Calibrations and Quality Assessments

Continuous HONO output was generated by flushing the headspace of dilute aqueous HCl with zero air across a fresh $NaNO_2$ salt bed. HONO is challenging to measure in the ambient atmosphere, particularly in chemically complex and highly polluted environments such as wildfire plumes. One challenge to HONO measurements using CIMS is the potential interference by ions with the same mass-to-charge ratio, the most common being the naturally occurring ^{13}C isotope of formic acid (HCOOH). Iodide adduct ionization detects both HONO and HCOOH, and both are expected in wildfire plumes. In most plumes sampled during this campaign, the $H^{13}COOH$ signal

was only a minor contributor to total signal at the same unit mass as HONO and the mass accuracy and resolving power allow for robust fitting and removal of the corresponding signal (see Figure S2.1).

A second common concern is the generation of HONO from NO_2 conversion on surfaces within the sampling manifold. In Figure S2.2, *in situ* observations of HONO, NO_x and CO during a set of intercepts through the Taylor Creek Fire smoke plume (RF03, 30 July 2018), are shown, where two transects (labeled as "fresh plume" and "aged plume") are highlighted. Based on the observed behavior, the contribution of NO_2 conversion to HONO in the instrument must be less than 10% given the variation in the HONO/NO_2 ratio within the same fire plume, consistent with the short residence time in the sampling manifold (< 0.7 s) limiting the influence of wall interactions.

For the calibrations to HONO described in the main text, we verified the detection efficiency of the NO_y analyzer using a calibrated HNO_3 permeation tube source immediately prior to and after the WE-CAN campaign. We assumed that the conversion efficiency of the molybdenum catalyst for HONO to NO was unity(Allegrini et al., 1987). For the UV-VIS analysis of the HONO source, we compared the absorbance of the solutions containing Griess reagent and the output of the HONO generator to that from a set of calibration solutions of sodium nitrite in water. These two methods (NO_y-chemiluminescence and optical absorbance) resulted in a HONO calibration factor for the HRToF-CIMS of 2.1 ± 0.6 counts per second/pptv HONO/10^6 counts per second of reagent ions. This was the value when the water vapor concentrations in the IMR provided a 0.5 ratio of $[I(H_2O)^-]/I^-$ for the CIMS tuning used during WE-CAN. The water vapor dependence for HONO was also measured (see Table S2.2).

Calibrations for other trace gases reported by the HRToF-CIMS in this study were more straightforward and followed approaches described previously (Lee et al., 2018), involving permeation tubes and compressed gas mixtures each independently verified by gravimetric analysis or the vendor. Table S2.2 lists the calibration factors, method, and associated uncertainties for the HRToF-CIMS observations used herein.

2.5.4 Physical Plume Age Estimates

To analyze the temporal evolution of HONO after emission, we calculate the physical plume ages as distances from the geometric center of plume intercepts to the fire source divided by the mean wind speed measured within the plumes. For instance, the distance between the geometric center of the first plume pass we encountered in RF03 and fire source is 12.1 km, and the mean wind speed during this intercept is 7.46 m s^{-1}, thus the physical plume age is calculated to be 27 min. WE-CAN Flight tracks colored by HONO mixing ratios are shown in Figure S2.3. The fire sources were determined by U.S. Forest Service through a series of analysis. The location of the fires was confidently identified for 189 out of the 258 plumes segments observed in WE-CAN, while the remaining 69 were more likely regionally mixed smoke with uncertain or unknown sources. Of the 189 plume segments, these were linked to the 19 fires shown in Figure 2.3. Uncertainties in ages are assumed to be due only to the measured wind speed variations. The wind speed varies across the plumes, and in some cases, plumes from multiple fires are actively mixing together. Consequently, the physical age estimates for a particular plume may vary.

2.5.5 NEMR Calculation Methods and Associated Uncertainties

There are two common ways of calculating plume-average $NEMR_x$ in practice: one from the regression slope of locally enhanced X and Y concentrations in each plume pass, and the other

being an integration under the in-plume excess mixing ratio time series. The latter approach has been more prevalently used in continuous measurements since it accounts for different instrument response times (Karl et al., 2007).

This rapid spatially heterogeneous HONO depletion affects estimates of NEMR via plume integration methods. NEMR calculated using the ratio of full integral across the entire plume pass, for more direct comparisons with past studies, is shown in Figure S2.5. As noted in the main text, we chose to use the ratio of the maximum concentration enhancement, specifically the ratio of mean of the highest 5% background-corrected HONO concentrations in an intercept to the mean of background-corrected tracer (e.g., CO or NO_x) concentrations within the same time window where the top 5% HONO concentrations are measured. Both approaches give broadly the same results within measurement uncertainty, but the full integral method is 40% lower for HONO to CO NEMR, and 29% lower for HONO to NO_x NEMR on average in these fresh plumes as expected since it is likely affected by faster decay of HONO at the plume edges.

Uncertainty is dominated by the uncertainty in our HONO calibration factor which we estimate as ± 30% based on the multiple calibration attempts. Uncertainty from the subtraction of ambient background to determine plume enhancements can arise both from the challenge to identify the background concentrations near large fire complexes burning for several days, and also as the plume evolves downwind becoming more diluted with in-plume concentrations approaching the background values (May et al., 2015). In our case, given our focus on the near-field observations made possible during WE-CAN, uncertainties in background ambient concentrations have no impact on our conclusions as the measured □HONO are in the tens of ppbv and background ambient concentrations are tens of pptv at the most.

2.5.6 Spatial Variation of Plume Photolysis Frequencies

As indicated in Figure 2.2, the lifetime of HONO within fire plumes is dependent on plume age as well as the relative position within the plume likely due to the differing radiative impacts of aerosol particles. We compared the evolution of j_{HONO} at different plume positions, shown in Figure S2.4. Peak HONO enhancements (95^{th} percentile for each plume transect) were used to identify the plume centers, moderate HONO enhancements (70^{th} percentile) for plume wings, and low HONO enhancements (30^{th} percentile) for plume edges. These different plume scenarios gave three estimates of photolysis rates evolution versus time. There are clear differences in j_{HONO} and thus photochemical processing between the center and edges of the plume. The HONO photolysis frequencies measured near the plume center were typically about half of that near the plume edge. Young plumes tend to be optically thick with lower j-values overall, but the lowest j-values always occur in the plume center, as expected.

2.5.7 Radical Source Strength Quantification

As indicated in section 3.2 in the main text, we used campaign-wide in-plume observations of actinic flux, O_3, water vapor, formaldehyde (HCHO), acetaldehyde (CH_3CHO), alkenes, nitric acid (HNO_3), and HONO to generate an observationally constrained estimate of the average primary radical source strength within plumes as a function of plume age. The sources of HO_x mainly include photolysis of HONO (R1), O_3 (R2), HCHO (R3), CH_3CHO (R4), as well as non-photolytic sources like ozonolysis of alkenes (R5).

(R1) $HONO + h\nu \rightarrow OH + NO$

(R2a) $O_3 + h\nu \rightarrow O(^1D) + O_2$

(R2b) $O(^1D) + H_2O \rightarrow 2\ OH$

(R2c) $O(^1D) + M \rightarrow O(^3P) + M$

(R3) $HCHO + hv + 2\ O_2 \rightarrow 2\ HO_2 + CO$

(R4) $CH_3CHO + hv + O_2 \rightarrow CH_3 + HO_2 + CO$

(R5) $Alkenes + O_3 \rightarrow OH, HO_2, RO_2 + products$

The total production rate is calculated as

$$P(HO_X) = j_{HONO}[HONO] + 2j_{HCHO}[HCHO] + j_{CH_3CHO}[CH_3CHO] + \emptyset_{OH} j_{O^1D}[O_3] + \sum_i [O_3](k_i[alkene_i]), \quad (2.6)$$

where

$$\emptyset_{OH} = \frac{2[H_2O]}{k[M]} \quad (2.7)$$

For ozone photolysis, $\emptyset_{OH}$ is the yield of OH from the reaction of $O(^1D)$ with H_2O (R2b) against deactivation of $O(^1D)$ via collisions with other gases (denoted as M) such as N_2 and O_2 (R2c). Thus the yield $\emptyset_{OH}$ is dependent on the relative abundance of water vapor and M (2.7). In case of ozonolysis reactions, the HO_x yields varies with each alkene species i, and the summation of all measured alkene-ozone reactivity were used for deriving HO_x source strength. In our study, HO_x production from ozonolysis is negligible compared to the photolytic sources and were discarded in the budget analysis.

2.6. REFERENCES

Akagi, S. K., Yokelson, R. J., Wiedinmyer, C., Alvarado, M. J., Reid, J. S., Karl, T., et al. (2011). Atmospheric Chemistry and Physics Emission factors for open and domestic biomass burning for use in atmospheric models. *Atmos. Chem. Phys*, *11*, 4039–4072. https://doi.org/10.5194/acp-11-4039-2011

Akagi, S. K., Craven, J. S., Taylor, J. W., Mcmeeking, G. R., Yokelson, R. J., Burling, I. R., et al. (2012). Evolution of trace gases and particles emitted by a chaparral fire in California. *Atmos. Chem. Phys*, *12*, 1397–1421. https://doi.org/10.5194/acp-12-1397-2012

Akagi, S. K., Yokelson, R. J., Burling, I. R., Meinardi, S., Simpson, I., Blake, D. R., et al. (2013). Measurements of reactive trace gases and variable O $_3$ formation rates in some South Carolina biomass burning plumes. *Atmospheric Chemistry and Physics*, *13*(3), 1141–1165. https://doi.org/10.5194/acp-13-1141-2013

Allegrini, I., Buttini, P., Di Palo, V., & Possanzini, M. (1987). Preparation of Standard Atmospheres of Nitrogen Acid Compounds: The NO2 Permeation Tube. In *Physico-Chemical Behaviour of Atmospheric Pollutants* (pp. 15–24). Springer Netherlands. https://doi.org/10.1007/978-94-009-3841-0_3

Alvarado, M. J., & Prinn, R. G. (2009). Formation of ozone and growth of aerosols in young smoke plumes from biomass burning: 1. Lagrangian parcel studies. *Journal of Geophysical Research Atmospheres*, *114*(9), D09306. https://doi.org/10.1029/2008JD011144

Alvarado, M. J., Wang, C., & Prinn, R. G. (2009). Formation of ozone and growth of aerosols in young smoke plumes from biomass burning: 2. Three-dimensional Eulerian studies, *114*, D09307. https://doi.org/10.1029/2008JD011186

Apel, E. C., Hornbrook, R. S., Hills, A. J., Blake, N. J., Barth, M. C., Weinheimer, A., et al. (2015). Upper tropospheric ozone production from lightning NOx-impacted convection: Smoke ingestion case study from the DC3 campaign. *Journal of Geophysical Research*, *120*(6), 2505–2523. https://doi.org/10.1002/2014JD022121

Barney, W. S., Wingen, L. M., Lakin, M. J., Brauers, T., Stutz, J., & Finlayson-Pitts, B. J. (2000). Infrared absorption cross-section measurements for nitrous acid (HONO) at room temperature. *Journal of Physical Chemistry A*, *104*(8), 1692–1699. https://doi.org/10.1021/jp9930503

Briggs, N. L., Jaffe, D. A., Gao, H., Hee, J. R., Baylon, P. M., Zhang, Q., et al. (2016). Particulate matter, ozone, and nitrogen species in aged wildfire plumes observed at the Mount Bachelor Observatory. *Aerosol and Air Quality Research*, *16*(12), 3075–3087. https://doi.org/10.4209/aaqr.2016.03.0120

Burling, I. R., Yokelson, R. J., Griffith, D. W. T., Johnson, T. J., Veres, P., Roberts, J. M., et al. (2010). Laboratory measurements of trace gas emissions from biomass burning of fuel types from the southeastern and southwestern United States. *Atmos. Chem. Phys*, *10*, 11115–11130. https://doi.org/10.5194/acp-10-11115-2010

Burling, I. R., Yokelson, R. J., Akagi, S. K., Urbanski, S. P., Wold, C. E., Griffith, D. W. T., et al. (2011). Airborne and ground-based measurements of the trace gases and particles emitted by prescribed fires in the United States. *Atmospheric Chemistry and Physics*, *11*(23), 12197–12216. https://doi.org/10.5194/acp-11-12197-2011

Chai, J., Miller, D. J., Scheuer, E., Dibb, J., Selimovic, V., Yokelson, R., et al. (2019). Isotopic

characterization of nitrogen oxides (NOx), nitrous acid (HONO), and nitrate (pNO3−) from laboratory biomass burning during FIREX. *Atmospheric Measurement Techniques*, *12*(12), 6303–6317. https://doi.org/10.5194/amt-12-6303-2019

Chen, L. W. A., Moosmüller, H., Arnott, W. P., Chow, J. C., Watson, J. G., Susott, R. A., et al. (2007). Emissions from laboratory combustion of wildland fuels: Emission factors and source profiles. *Environmental Science and Technology*, *41*(12), 4317–4325. https://doi.org/10.1021/es062364i

Coggon, M. M., Veres, P. R., Yuan, B., Koss, A., Warneke, C., Gilman, J. B., et al. (2016). Emissions of nitrogen-containing organic compounds from the burning of herbaceous and arboraceous biomass: Fuel composition dependence and the variability of commonly used nitrile tracers. *Geophysical Research Letters*, *43*(18), 9903–9912. https://doi.org/10.1002/2016GL070562

Elshorbany, Y. F., Kurtenbach, R., Wiesen, P., Lissi, E., Rubio, M., Villena, G., et al. (2009). Oxidation capacity of the city air of Santiago, Chile. *Atmospheric Chemistry and Physics*, *9*(6), 2257–2273. https://doi.org/10.5194/acp-9-2257-2009

Febo, A., Perrino, C., Gherardi, M., & Sparapani, R. (1995). Evaluation of a High-Purity and High-Stability Continuous Generation System for Nitrous Acid. *Environ. Sci. Technol*, *29*, 2390–2395. https://doi.org/10.1021/es00009a035

Garofalo, L. A., Pothier, M. A., Levin, E. J. T., Campos, T., Kreidenweis, S. M., & Farmer, D. K. (2019). Emission and Evolution of Submicron Organic Aerosol in Smoke from Wildfires in the Western United States. *ACS Earth and Space Chemistry*, *3*(7), 1237–1247. https://doi.org/10.1021/acsearthspacechem.9b00125

Goode, J. G., Yokelson, R. J., Susott, R. A., & Ward, D. E. (1999). Trace gas emissions from laboratory biomass fires measured by open-path Fourier transform infrared spectroscopy: Fires in grass and surface fuels. *Journal of Geophysical Research Atmospheres*, *104*(D17), 21237–21245. https://doi.org/10.1029/1999JD900360

Goode, J. G., Yokelson, R. J., Ward, D. E., Susott, R. A., Babbitt, R. E., Davies, M. A., & Hao, W. M. (2000). Measurements of excess O3, CO2, CO, CH4, C2H4, C2H2, HCN, NO, NH3, HCOOH, CH3COOH, HCHO, and CH3OH in 1997 Alaskan biomass burning plumes by airborne Fourier transform infrared spectroscopy (AFTIR). *Journal of Geophysical Research Atmospheres*, *105*(D17), 22147–22166. https://doi.org/10.1029/2000jd900287

Hansson, K. M., Samuelsson, J., Åmand, L. E., & Tullin, C. (2003). The temperature's influence on the selectivity between HNCO and HCN from pyrolysis of 2,5-diketopiperazine and 2-pyridone. *Fuel*, *82*(18), 2163–2172. https://doi.org/10.1016/S0016-2361(03)00206-0

Hansson, K. M., Samuelsson, J., Tullin, C., & Åmand, L. E. (2004). Formation of HNCO, HCN, and NH3 from the pyrolysis of bark and nitrogen-containing model compounds. *Combustion and Flame*, *137*(3), 265–277. https://doi.org/10.1016/j.combustflame.2004.01.005

Haskins, J. D., Lopez-Hilfiker, F. D., Lee, B. H., Shah, V., Wolfe, G. M., DiGangi, J., et al. (2019). Anthropogenic Control Over Wintertime Oxidation of Atmospheric Pollutants. *Geophysical Research Letters*, *46*(24), 14826–14835. https://doi.org/10.1029/2019GL085498

Hu, L., Millet, D. B., Baasandorj, M., Griffis, T. J., Turner, P., Helmig, D., et al. (2015). Isoprene emissions and impacts over an ecological transition region in the U.S. Upper Midwest inferred from tall tower measurements. *Journal of Geophysical Research*, *120*(8), 3553–3571. https://doi.org/10.1002/2014JD022732

Jaffe, D. A., Wigder, N., Downey, N., Pfister, G., Boynard, A., & Reid, S. B. (2013). Impact of Wildfires on Ozone Exceptional Events in the Western U.S. *Environmental Science & Technology*, *47*(19), 11065–11072. https://doi.org/10.1021/es402164f

Karl, T. G., Christian, T. J., Yokelson, R. J., Artaxo, P., Hao, W. M., & Guenther, A. (2007). The Tropical Forest and Fire Emissions Experiment: method evaluation of volatile organic compound emissions measured by PTR-MS, FTIR, and GC from tropical biomass burning. *Atmospheric Chemistry and Physics*, *7*(22), 5883–5897. https://doi.org/10.5194/acp-7-5883-2007

Keene, W. C., Lobert, J. M., Crutzen, P. J., Maben, J. R., Scharffe, D. H., Landmann, T., et al. (2006). Emissions of major gaseous and particulate species during experimental burns of southern African biomass. *Journal of Geophysical Research Atmospheres*, *111*(4). https://doi.org/10.1029/2005JD006319

Koppmann, R., Von Czapiewski, K., & Reid, J. S. (2005). A review of biomass burning emissions, part I A review of biomass burning emissions, part I: gaseous emissions of carbon monoxide, methane, volatile organic compounds, and nitrogen containing compounds A review of biomass burning emissions, part I A revie. *Atmos. Chem. Phys. Discuss*, *5*, 10455–10516. Retrieved from www.atmos-chem-phys.org/acpd/5/10455/SRef-ID:1680-7375/acpd/2005-5-10455EuropeanGeosciencesUnion

Koss, A. R., Sekimoto, K., Gilman, J. B., Selimovic, V., Coggon, M. M., Zarzana, K. J., et al. (2018). Non-methane organic gas emissions from biomass burning: identification, quantification, and emission factors from PTR-ToF during the FIREX 2016 laboratory experiment. *Atmos. Chem. Phys*, *18*, 3299–3319. https://doi.org/10.5194/acp-18-3299-2018

Kwok, C. Y., Laurent, O., Guemri, A., Philippon, C., Wastine, B., Rella, C. W., et al. (2015). Comprehensive laboratory and field testing of cavity ring-down spectroscopy analyzers measuring H2O, CO2, CH4 and CO. *Atmos. Meas. Tech*, *8*, 3867–3892. https://doi.org/10.5194/amt-8-3867-2015

Lee, B. H., Lopez-Hilfiker, F. D., Mohr, C., Kurtén, T., Worsnop, D. R., & Thornton, J. A. (2014). An iodide-adduct high-resolution time-of-flight chemical-ionization mass spectrometer: Application to atmospheric inorganic and organic compounds. *Environmental Science and Technology*, *48*(11), 6309–6317. https://doi.org/10.1021/es500362a

Lee, B. H., Lopez-Hilfiker, F. D., Veres, P. R., McDuffie, E. E., Fibiger, D. L., Sparks, T. L., et al. (2018). Flight Deployment of a High-Resolution Time-of-Flight Chemical Ionization Mass Spectrometer: Observations of Reactive Halogen and Nitrogen Oxide Species. *Journal of Geophysical Research: Atmospheres*, *123*(14), 7670–7686. https://doi.org/10.1029/2017JD028082

Leppälahti, J., & Koljonen, T. (1995). Nitrogen evolution from coal, peat and wood during gasification: Literature review. *Fuel Processing Technology*, *43*(1), 1–45. https://doi.org/10.1016/0378-3820(94)00123-B

Li, Y. Q., Schwab, J. J., & Demerjian, K. L. (2008). Fast time response measurements of gaseous nitrous acid using a tunable diode laser absorption spectrometer: HONO emission source from vehicle exhausts. *Geophysical Research Letters*, *35*(4). https://doi.org/10.1029/2007GL031218

Liu, Z., Wang, Y., Gu, D., Zhao, C., Huey, L. G., Stickel, R., et al. (2012). Summertime photochemistry during CAREBeijing-2007: RO x budgets and O 3 formation. *Atmos. Chem. Phys*, *12*, 7737–7752. https://doi.org/10.5194/acp-12-7737-2012

May, A. A., Lee, T., Mcmeeking, G. R., Akagi, S., Sullivan, A. P., Urbanski, S., et al. (2015).

Observations and analysis of organic aerosol evolution in some prescribed fire smoke plumes, *15*(11), 6323–6335. https://doi.org/10.5194/acp-15-6323-2015

McMeeking, G. R., Kreidenweis, S. M., Baker, S., Carrico, C. M., Chow, J. C., Collett, J. L., et al. (2009). Emissions of trace gases and aerosols during the open combustion of biomass in the laboratory. *Journal of Geophysical Research Atmospheres*, *114*(19). https://doi.org/10.1029/2009JD011836

Müller, M., Anderson, B. E., Beyersdorf, A. J., Crawford, J. H., Diskin, G. S., Eichler, P., et al. (2016). In situ measurements and modeling of reactive trace gases in a small biomass burning plume. *Atmospheric Chemistry and Physics*, *16*(6), 3813–3824. https://doi.org/10.5194/acp-16-3813-2016

Neuman, J. A., Trainer, M., Brown, S. S., Min, K.-E., Nowak, J. B., Parrish, D. D., et al. (2016). HONO emission and production determined from airborne measurements over the Southeast U.S. *Journal of Geophysical Research: Atmospheres*, *121*(15), 9237–9250. https://doi.org/10.1002/2016JD025197

Palm, B. B., Liu, X., Jimenez, J. L., & Thornton, J. A. (2019). Performance of a new coaxial ion-molecule reaction region for low-pressure chemical ionization mass spectrometry with reduced instrument wall interactions. *Atmos. Meas. Tech*, *12*, 5829–5844. https://doi.org/10.5194/amt-12-5829-2019

Pollack, I. B., Lindaas, J., Roscioli, J. R., Agnese, M., Permar, W., Hu, L., & Fischer, E. V. (2019). Evaluation of ambient ammonia measurements from a research aircraft using a closed-path QC-TILDAS operated with active continuous passivation. *Atmos. Meas. Tech*, *12*, 3717–3742. https://doi.org/10.5194/amt-12-3717-2019

Ridley, B. A., & Grahek, F. E. (1990). A Small, Low Flow, High Sensitivity Reaction Vessel for NO Chemiluminescence Detectors. *Journal of Atmospheric and Oceanic Technology*, *7*(2), 307–311. https://doi.org/10.1175/1520-0426(1990)007<0307:aslfhs>2.0.co;2

Ridley, B. A., Grahek, F. E., & Walega, J. G. (1992). A small, high-sensitivity, medium-response ozone detector suitable for measurements from light aircraft. *Journal of Atmospheric & Oceanic Technology*, *9*(2), 142–148. https://doi.org/10.1175/1520-0426(1992)009<0142:ASHSMR>2.0.CO;2

Scharko, N. K., Oeck, A. M., Myers, T. L., Tonkyn, R. G., Banach, C. A., Baker, S. P., et al. (2019). Gas-phase pyrolysis products emitted by prescribed fires in pine forests with a shrub understory in the southeastern United States. *Atmospheric Chemistry and Physics*, *19*(15), 9681–9698. https://doi.org/10.5194/acp-19-9681-2019

Sekimoto, K., Koss, A. R., Gilman, J. B., Selimovic, V., Coggon, M. M., Zarzana, K. J., et al. (2018). High-and low-temperature pyrolysis profiles describe volatile organic compound emissions from western US wildfire fuels. *Atmos. Chem. Phys*, *18*, 9263–9281. https://doi.org/10.5194/acp-18-9263-2018

Selimovic, V., Yokelson, R. J., Warneke, C., Roberts, J. M., De Gouw, J., Reardon, J., & Griffith, D. W. T. (2018). Aerosol optical properties and trace gas emissions by PAX and OP-FTIR for laboratory-simulated western US wildfires during FIREX. *Atmos. Chem. Phys*, *18*, 2929–2948. https://doi.org/10.5194/acp-18-2929-2018

Shetter, R. E., & Müller, M. (1999). Photolysis frequency measurements using actinic flux spectroradiometry during the PEM-Tropics mission: Instrumentation description and some results. *Journal of Geophysical Research: Atmospheres*, *104*(D5), 5647–5661. https://doi.org/10.1029/98JD01381

Stockwell, C. E., Yokelson, R. J., Kreidenweis, S. M., Robinson, A. L., Demott, P. J., Sullivan,

R. C., et al. (2014). Trace gas emissions from combustion of peat, crop residue, domestic biofuels, grasses, and other fuels: configuration and Fourier transform infrared (FTIR) component of the fourth Fire Lab at Missoula Experiment (FLAME-4). *Atmos. Chem. Phys*, *14*, 9727–9754. https://doi.org/10.5194/acp-14-9727-2014

Stockwell, W. R., & Calvert, J. G. (1978). The near ultraviolet absorption spectrum of gaseous HONO and N2O3. *Journal of Photochemistry*, *8*(2), 193–203. https://doi.org/10.1016/0047-2670(78)80019-7

Trentmann, J., Yokelson, R. J., Hobbs, P. V., Winterrath, T., Christian, T. J., Andreae, M. O., & Mason, S. A. (2005). An analysis of the chemical processes in the smoke plume from a savanna fire. *Journal of Geophysical Research D: Atmospheres*, *110*(12), 1–20. https://doi.org/10.1029/2004JD005628

Urbanski, S. (2014). Wildland fire emissions, carbon, and climate: Emission factors. *Forest Ecology and Management*, *317*, 51–60. https://doi.org/10.1016/j.foreco.2013.05.045

Veres, P., Roberts, J. M., Burling, I. R., Warneke, C., De Gouw, J., & Yokelson, R. J. (2010). Measurements of gas-phase inorganic and organic acids from biomass fires by negative-ion proton-transfer chemical-ionization mass spectrometry. *Journal of Geophysical Research Atmospheres*, *115*(23), D23302. https://doi.org/10.1029/2010JD014033

Wang, S., Hornbrook, R. S., Hills, A., Emmons, L. K., Tilmes, S., Lamarque, J. F., et al. (2019). Atmospheric Acetaldehyde: Importance of Air-Sea Exchange and a Missing Source in the Remote Troposphere. *Geophysical Research Letters*, *46*(10), 5601–5613. https://doi.org/10.1029/2019GL082034

Ward, D. E., & Radke, L. F. (1993). Emissions Measurements from Vegetation Fires : A Comparative Evaluation of Methods and Results, Fire in the Environment: The Ecological, Atmospheric, and Climatic Importance of Vegetation Fires, edited by: In *Crutzen, P. J. and Goldammer, J. G., JohnWiley, New York* (pp. 53–76).

Xue, Z., Wu, Z., & Han, S. (2012). A selective fluorogenic sensor for visual detection of nitrite. *Analytical Methods*, *4*(7), 2021–2026. https://doi.org/10.1039/c2ay25107h

Ye, C., Zhou, X., Pu, D., Stutz, J., Festa, J., Spolaor, M., et al. (2016). Rapid cycling of reactive nitrogen in the marine boundary layer. *Nature*, *532*(7600), 489–491. https://doi.org/10.1038/nature17195

Yokelson, R. J., Goode, J. G., Ward, D. E., Susott, R. A., Babbitt, R. E., Wade, D. D., et al. (1999). Emissions of formaldehyde, acetic acid, methanol, and other trace gases from biomass fires in North Carolina measured by airborne Fourier transform infrared spectroscopy. *Journal of Geophysical Research: Atmospheres*, *104*(D23), 30109–30125. https://doi.org/10.1029/1999JD900817

Yokelson, R. J., Karl, T., Artaxo, P., Blake, D. R., Christian, T. J., Griffith, D. W. T., et al. (2007). The tropical forest and fire emissions experiment: Overview and airborne fire emission factor measurements. *Atmospheric Chemistry and Physics*, *7*(19), 5175–5196. https://doi.org/10.5194/acp-7-5175-2007

Yokelson, R. J., Christian, T. J., Karl, T. G., & Guenther, A. (2008). The tropical forest and fire emissions experiment: Laboratory fire measurements and synthesis of campaign data. *Atmospheric Chemistry and Physics*, *8*(13), 3509–3527. https://doi.org/10.5194/acp-8-3509-2008

Yokelson, R. J., Andreae, M. O., & Akagi, S. K. (2013). Pitfalls with the use of enhancement ratios or normalized excess mixing ratios measured in plumes to characterize pollution sources and aging. *Atmospheric Measurement Techniques*, *6*(8), 2155–2158.

https://doi.org/10.5194/amt-6-2155-2013
Yokelson, Robert J., Griffith, D. W. T., & Ward, D. E. (1996). Open-path fourier transform infrared studies of large-scale laboratory biomass fires. *Journal of Geophysical Research Atmospheres*, *101*(15), 21067–21080. https://doi.org/10.1029/96jd01800

2.7. TABLES

Table S2.1. Summary of selected chemical and meteorological variables measured aboard the C-130 aircraft in WE-CAN. WS-PCRDAS: Wavelength-scanned Picarro Cavity Ring-Down Absorption Spectroscopy; CLD: Chemiluminescence Detector with 400 nm LED for NO2 photolysis to NO; PTR-ToF-MS: Proton Transfer Reaction Time of Flight Mass Spectrometer; TOGA: Trace Organic Gas Analzyer; QC-TILDAS: Quantum-cascade Tunable Infrared Laser Direct Absorption Spectrometer; HARP: HIAPER Airborne Radiation Package

Measurement	Technique	Accuracy	Sample Interval	References
CO_2 CO	WS-PCRDAS	100 ppbv 50 ppbv	1s	Kwok et al., 2015)
NO NO_2 O_3	2-channel blue light CLD	3% 4% 2%	1s	Ridley & Grahek, 1990; Ridley et al., 1992
CH_3CN HCHO	PTR-ToF-MS	15%	0.2-0.5 s	Hu et al., 2015
HNO_3 HCOOH HONO HCN HNCO	UW HRToF-CIMS	30% 30% 30% 30% 30%	0.5 s	Lee et al., 2018; Palm et al., 2019
Alkenes CH_3CHO	TOGA	20%	1.75 min	Apel et al., 2015; Wang et al., 2019
NH_3	QC-TILDAS	12%	1s	Pollack et al., 2019
j_{HONO} j_{O3} j_{HCHO} j_{HNO3} j_{CH3CHO}	HARP	15% 25% 15% 15% 15%	3s	Shetter & Müller, 1999

Table S2.2. Calibration factors, method, and associated uncertainties for species measured by HRToF-CIMS in WE-CAN.

Compound	HONO	HCN	HNCO	HNO_3	HCOOH
Calibration factor[a]	2.1	0.2	0.2	7.4	4
IMR water vapor correction parameters, [*a*,*b*,*c*][b]	[-13.189, 8.9376, 1.0856]	[-58.91, -59.33, 0.006862]	n/a	[10.225, 7.6624, 1.9611]	[-5.0193, 3.7592, 1.0136]
Uncertainty	±30%	±30%	±30%	±30%	±30%
Method	$HCl_{(g)}$ + $NaNO_{2(s)}$ → $NaCl_{(s)}$ + $HNO_{2(g)}$	Gas standard (Airgas)	Assume same calibration factor as HCN	Permeation tube	Permeation tube

[a]Calibration factors when the signal ratio $I(H_2O)^-/I^-$ is equal to 0.5, for the tuning conditions used during WE-CAN.

[b]IMR water vapor corrections are relative sensitivities in the form of Relative Sensitivity = $a - be^{(-cx)}$, with the exception of HCOOH which uses Relative Sensitivity = $ax^2 + bx + c$. In both equations, x is equal to the ratio of $I(H_2O)^-/I^-$ signal measured in the CIMS, which is a measure of the water vapor concentration in the IMR, but is also dependent on the specific tuning of the mass spectrometer voltages due to declustering effects.

Table S2.3. HONO to CO emission ratios and quantification methods used in this work and past publications.

Akagi et al., 2011	Akagi et al., 2011	Veres et al., 2010b	Yokelson et al., 2009	Yokelson et al., 2007a	this work	this work
fire-integrated excess values over entire plume	fire-integrated excess values over entire plume	fire-integrated excess values over entire plume	fire-integrated excess values over entire plume	fire-integrated excess values over entire plume	fire-integrated excess values over entire plume	fire-average excess values over the highest 5% [HONO] in each plume
5.9 to 10.7	1.8 to 7.0	2.6 ± 0.95 (southwest fuels) 3.4 ± 1.4	2.8 ± 0.4	1.5	0.41 to 11.8	0.65 to 17.2
-	-	-	< 30 min	less than several minutes old	18 – 60 min	18 – 60 min
Tropical forests	temperate forests	mixed fuels	biomass burning in the Yucatan	pasture fire	Mixed fuels	Mixed fuels
field	field	lab	field	field	field	field
-	-	-	0.907 –0.945	0.910 ± 0.021	0.91 ± 0.03	0.91 ± 0.03

Paper	Koss et al., 2018	Neuman et al., 2016	Müller et al., 2016	Burling et al., 2011
Method to quantify plume-average NEMR	fire-integrated excess values over entire plume	Slope of linear least square fit	Slope of linear least square fit	Slope of linear least square fit
HONO to CO NEMR (pptv ppbv^{-1})	4.1 ± 1.8	from 1.3 to 5.2	2.0 ± 0.7	4.1
Age (min)	5 to 20 min	-	within 21 min	less than several minutes old
Fuel type/eco-region		agricultural burning	small forest understory fire	conifer forest understory burns
Lab/field	lab	field	field	field
Average MCE	-	0.92 - 0.96	0.90 ± 0.02	0.936 ± 0.024

Table S2.4. HONO to NOx emission ratios and quantification methods used in this work and past publications.

Selimovic et al., 2018	Stockwell et al., 2014	Burling et al., 2011	Burling et al., 2010	Yokelson et al., 2009	Keene et al., 2006	Trentmann et al., 2005	this work	this work
fire-integrated excess values over entire plume	fire-integrated excess values over entire plume	Slope of linear least square fit	fire-integrated excess values over entire plume	fire-integrated excess values over entire plume	fire-integrated excess values over entire plume	-	fire-integrated excess values over entire plume	fire-average excess values over the highest 5% [HONO] in each plume
0.90	0.13	0.077 to 0.22	0.03 to 0.20	0.14	0.048 (grass), 0.23 (shrubs), 0.067	0.03	0.21 to 1.11	0.25 to 1.4
a few minutes to half an	less than several minutes	less than several minutes	-	< 30 min	-	less than several minutes	0.3–1.0 h	0.3 – 1.0 h
Engelman n spruce	cooking fires	conifer forest understory ; oak	Mixed fuels	biomass burning in the Yucatan	southern African biomass	savanna	Mixed fuels	Mixed fuels
lab	lab	field	lab	field	lab	field	field	field
0.94 ± 0.02	0.968 ± 0.004	0.936 ± 0.024	0.945 ± 0.014	0.907 – 0.945	0.94	-	0.91 ± 0.03	0.91 ± 0.03

Paper	Selimovic et al., 2018
Method to quantify plume-average NEMR	fire-integrated excess values over entire plume
HONO to NO_x NEMR (pptv $pptv^{-1}$)	0.21 ± 0.13
Age (min)	a few minutes to half an
Fuel type/eco-region	mixed
Lab/field	lab
Average MCE	0.92 - 0.96

2.8. FIGURES

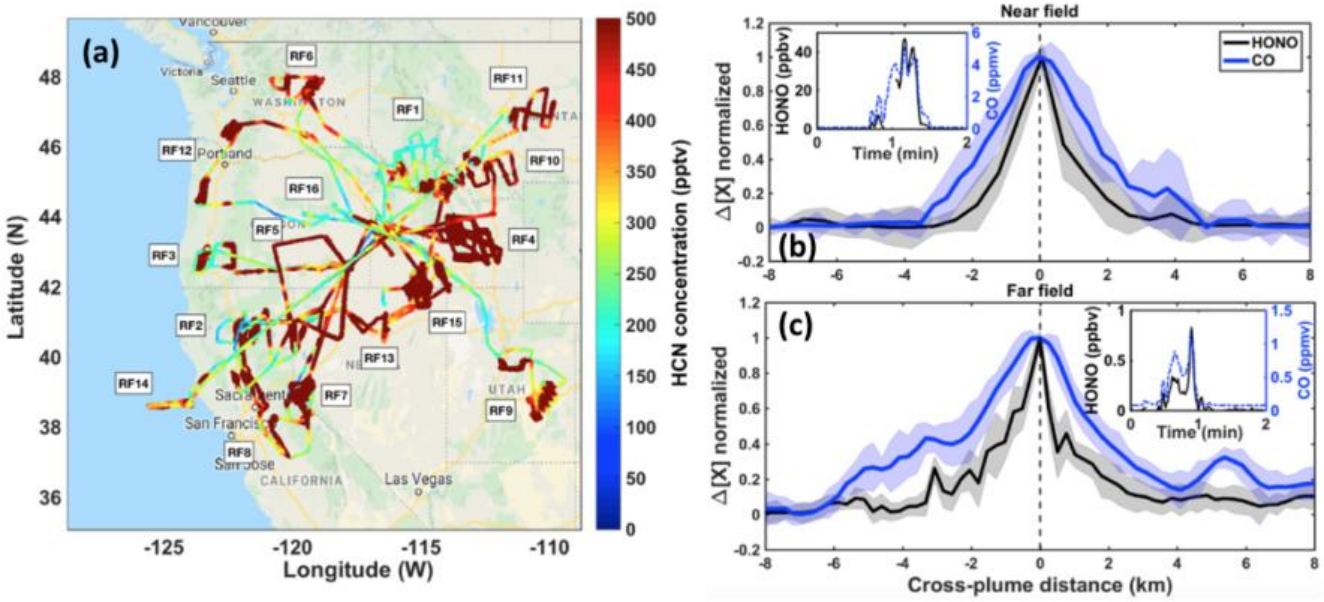

Figure 2.1. (left) WE-CAN flight tracks colored and sized by HCN mixing ratios. For symbols with HCN mixing ratios greater than 500 pptv, the color scale stays the same. The map is plotted using static Google Maps API which could be downloaded from https://www.mathworks.com/matlabcentral/fileexchange/27627-zoharby-plot_google_map.

(right) Binned, averaged, and normalized horizontal plume transects of HONO and CO excess mixing ratios in the near field (upper panel, physical age < 40 min) and far field (lower panel, physical age > 1 h) plumes. The plume cross-sections have been aligned so that their maxima define the plume center (distance = 0). The mean physical age is 28 min for the near-field plumes and 137 min for far field plumes. Shading represents the standard deviations for each bin. The average aircraft speed is ~ 128 m/s. In both cases, HONO plume widths are narrower than those for CO, likely due to the faster photolysis of HONO at the plume edges (see text). The insets show the absolute mixing ratios for example near-field (top) and far-field (bottom) plume transects from RF 3.

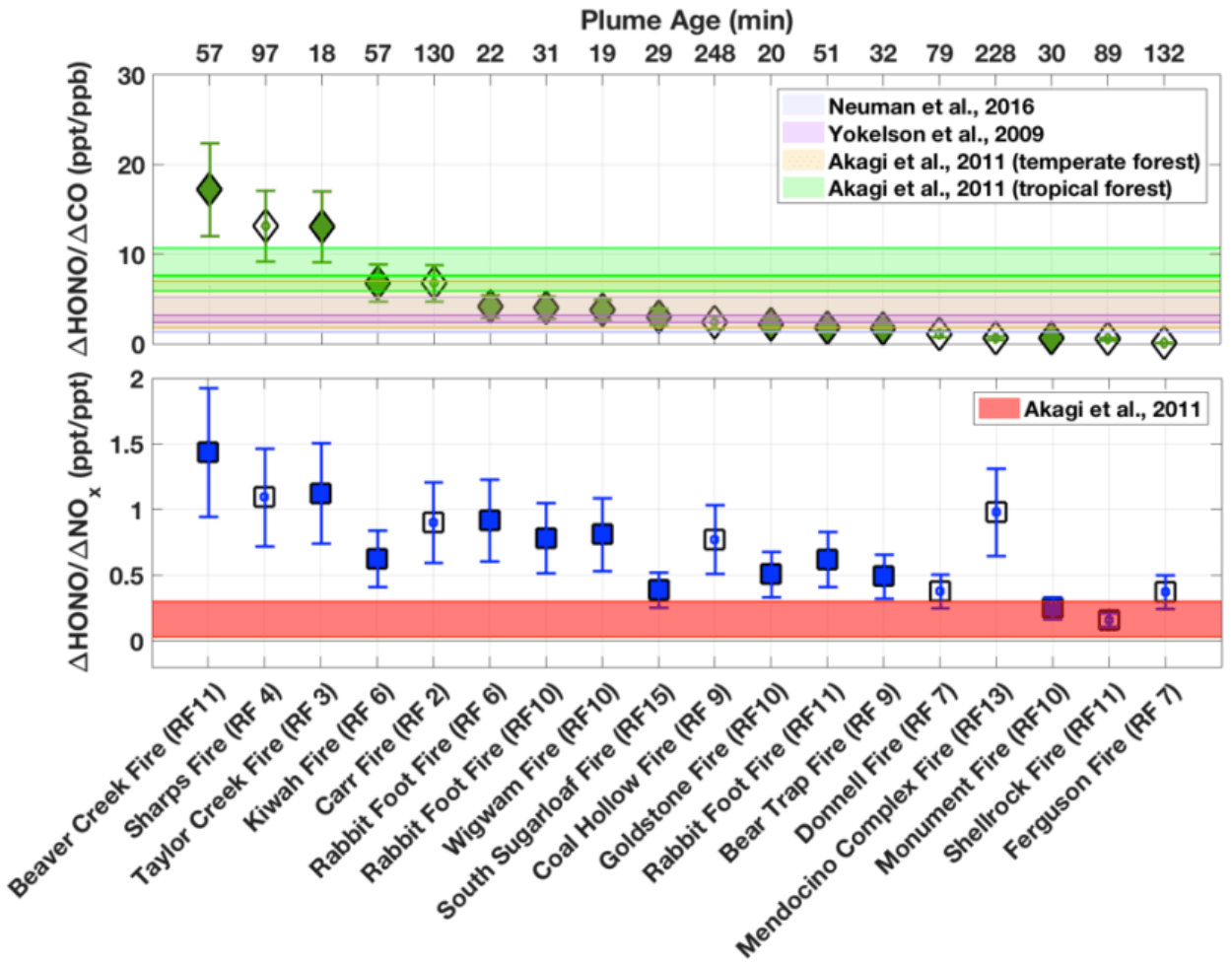

Figure 2.2. HONO enhancement ratios (derived from maximum enhancement method) relative to CO (top) and NO_x (bottom) in the freshest plume pass for each fire sampled, sorted in descending order of HONO to CO NEMR. The error bars represent the combined instrumental uncertainties summed in quadrature. The top axis shows the respective plume age. Selected reference HONO NEMR ranges from past campaigns are denoted for comparison. Plumes with physical ages greater than 1 h are shown in open markers.

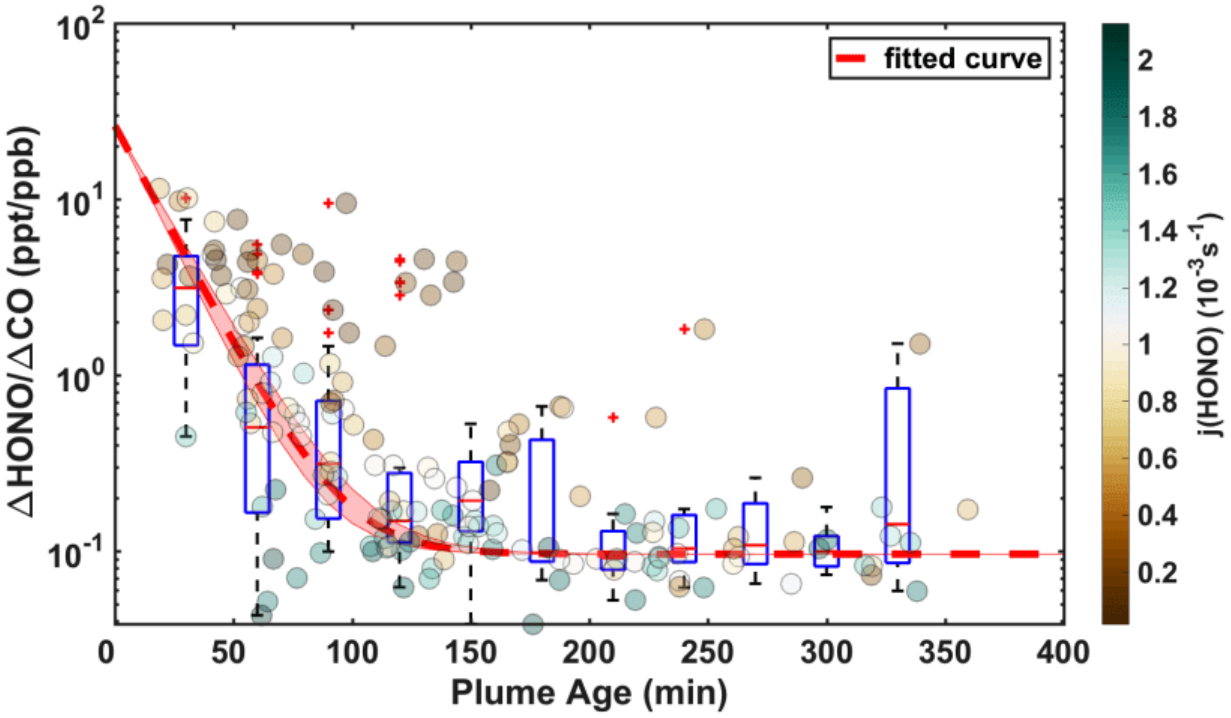

Figure 2.3. Campaign-wide ΔHONO/ΔCO enhancement ratio evolution with plume age colored by HONO photolysis frequency. Box-and-whisker plots (boxes: 25th and 75th percentiles; whiskers: 10th and 90th percentiles; horizontal lines: median) represent 30-minute binned data. The red curve is an exponential fit, with constant offset, to the median ΔHONO/ΔCO in each age bin. The shading is the 95% confidence bounds of the fitted curve.

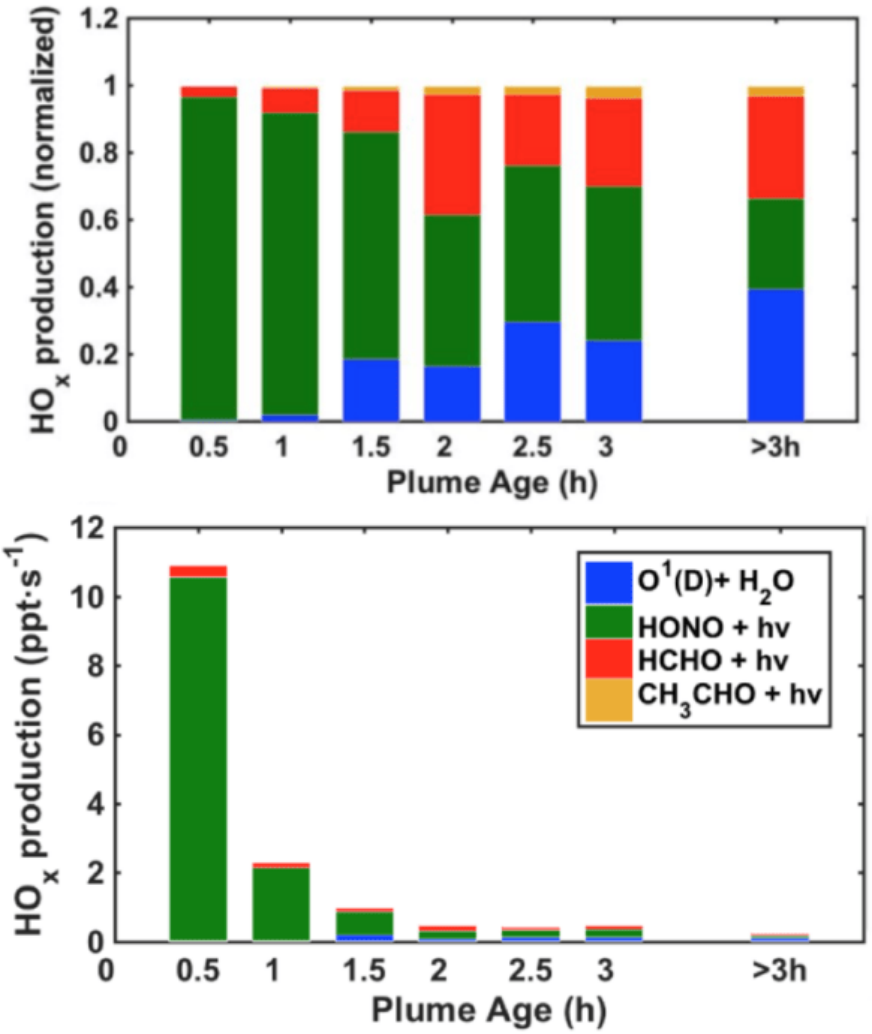

Figure 2.4. (top) Average relative contribution of different radical sources to HOx radicals versus plume age of all western wildfire plumes sampled in WE-CAN; (bottom) HOx production rate of different radical sources versus plume age.

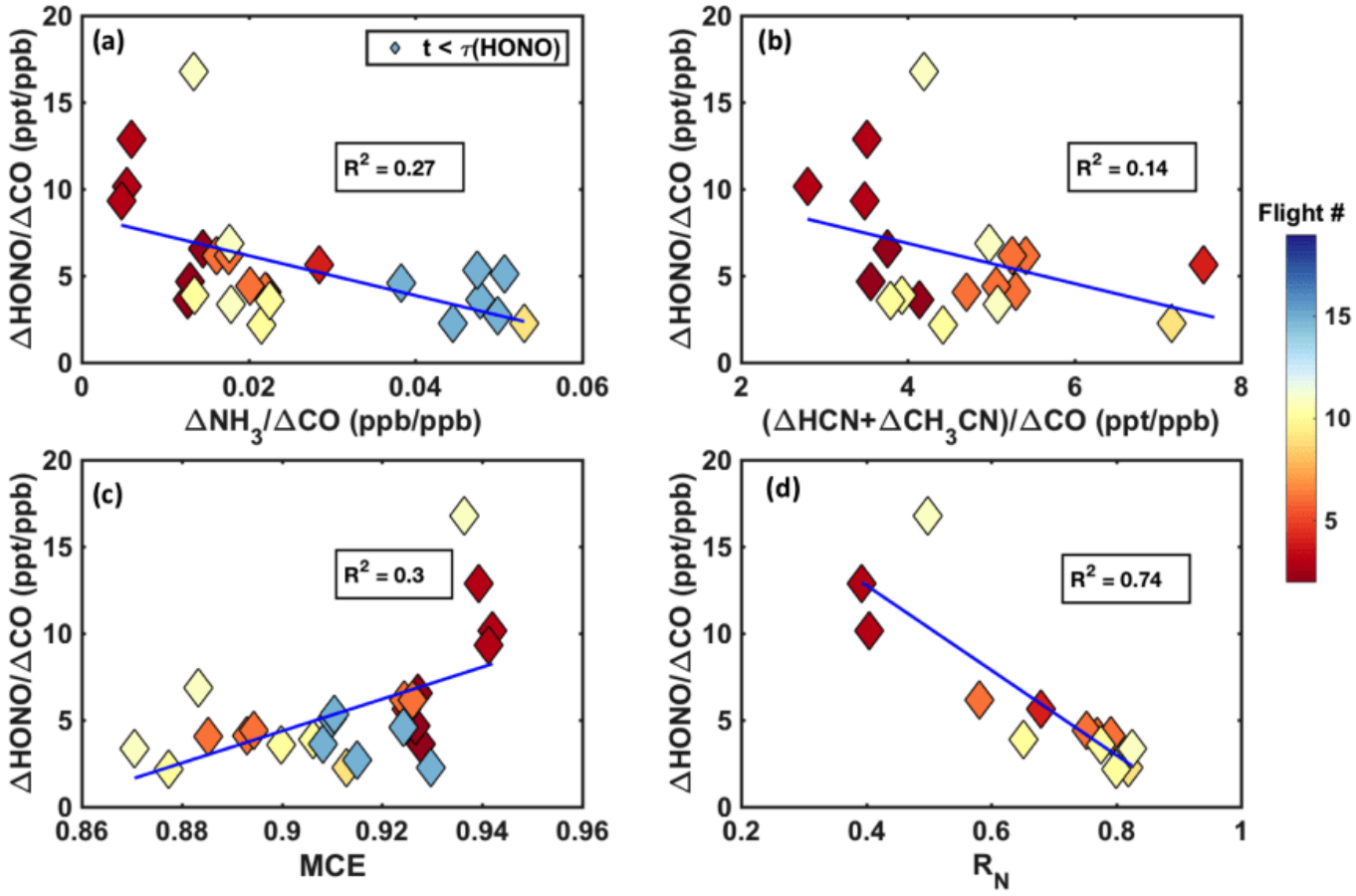

Figure 2.5. Scatter plots of HONO NEMR versus different tracers: (a) NH_3/CO, (b) (HCN+CH_3CN)/CO, (c) MCE, (d) (HCN+CH_3CN+NH_x)/(HCN+CH_3CN+NH_x +HNCO+NO_x+(NO_z-HONO), for fresh plumes within HONO photolysis lifetime derived from *j*(HONO) measurements. Correlation coefficients (R^2) were derived from bivariate linear regressions of all plotted data.

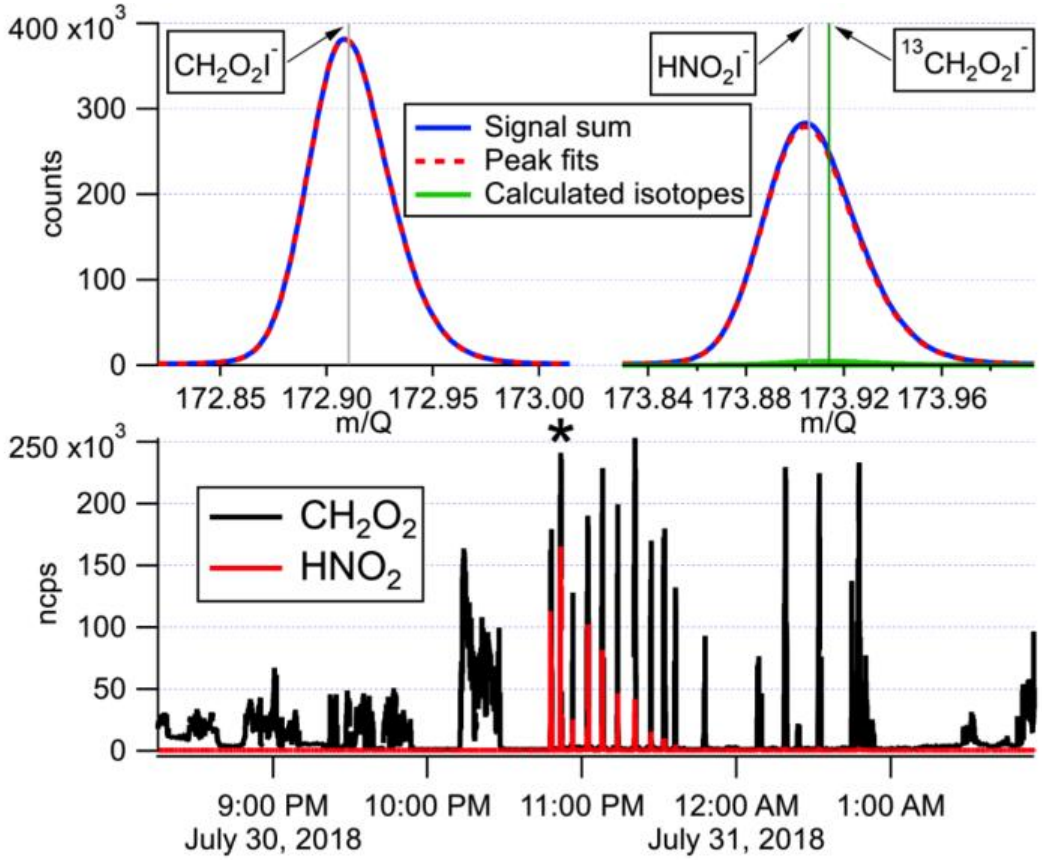

Figure S2.1. (top) High resolution mass spectrum of the HCOOH, and H^{13}COOH and HONO peaks; (bottom) time series of formic acid and HONO from Taylor Creek Fire (RF03). The data for the mass spectrum in the upper panel came from the time marked with the asterisk.

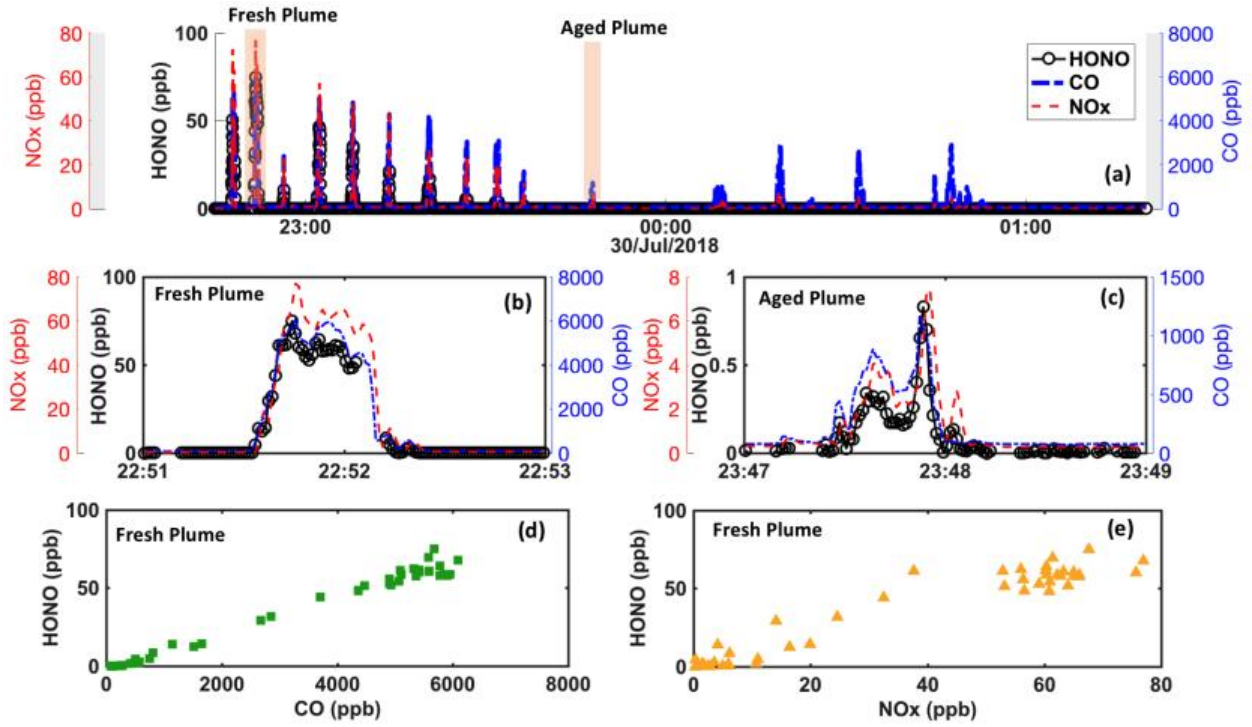

Figure S2.2. (a) A subset of time series of NO_x, HONO and CO in Taylor Creek fire, 30 July 2018 (RF03). One fresh plume and one aged plume are highlighted and labelled for comparison. (b-c) magnified plume intercepts. (d) Scatter plot of HONO versus CO in the fresh plume. (e) Scatter plot of HONO versus NO_x in the fresh plume.

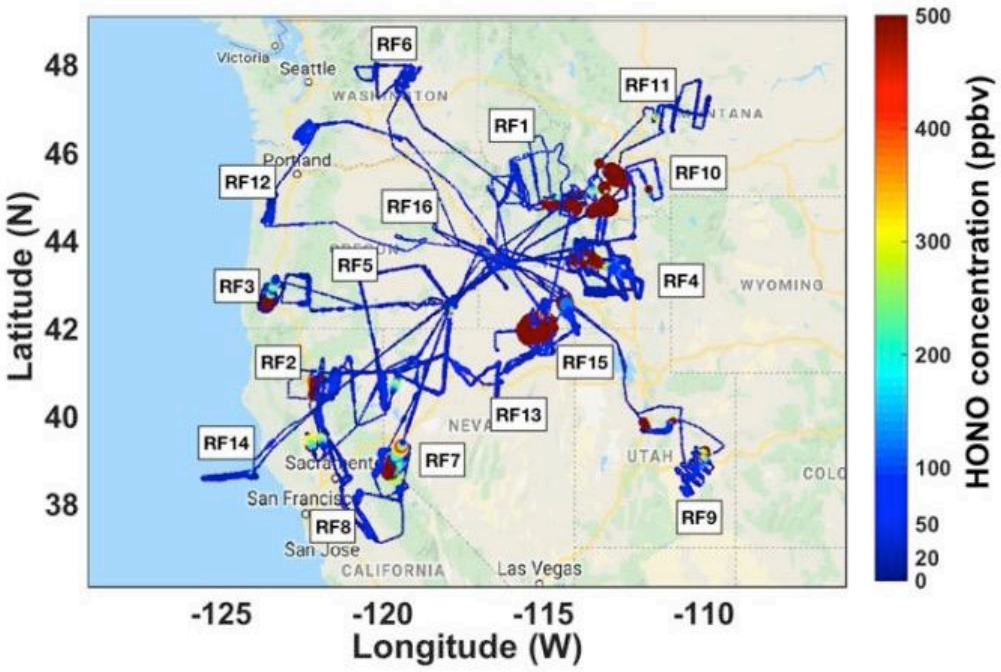

Figure S2.3. WE-CAN flight tracks colored and sized by HONO mixing ratios. For symbols with HONO mixing ratios greater than 500 pptv, the color scale stays the same. The map is plotted using static Google Maps API which could be downloaded from https://www.mathworks.com/matlabcentral/fileexchange/27627-zoharby-plot_google_map.

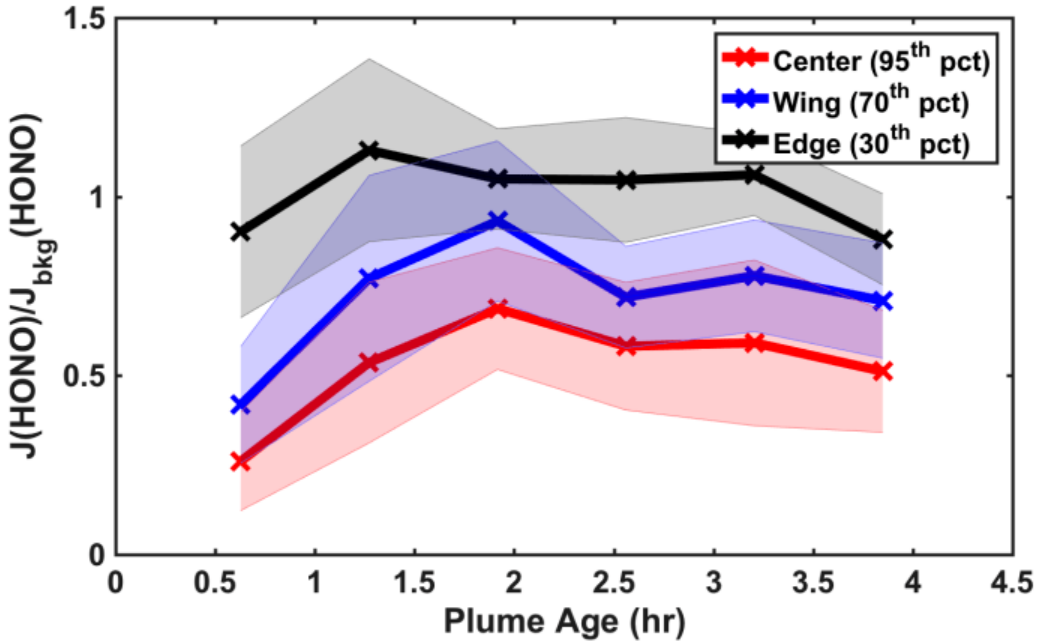

Figure S2.4. The photolysis rates of HONO relative to background air in different position of the plumes as a function of plume age. Each data point represents the 40-minute binned median of campaign-wide HONO photolysis rates relative to the background.

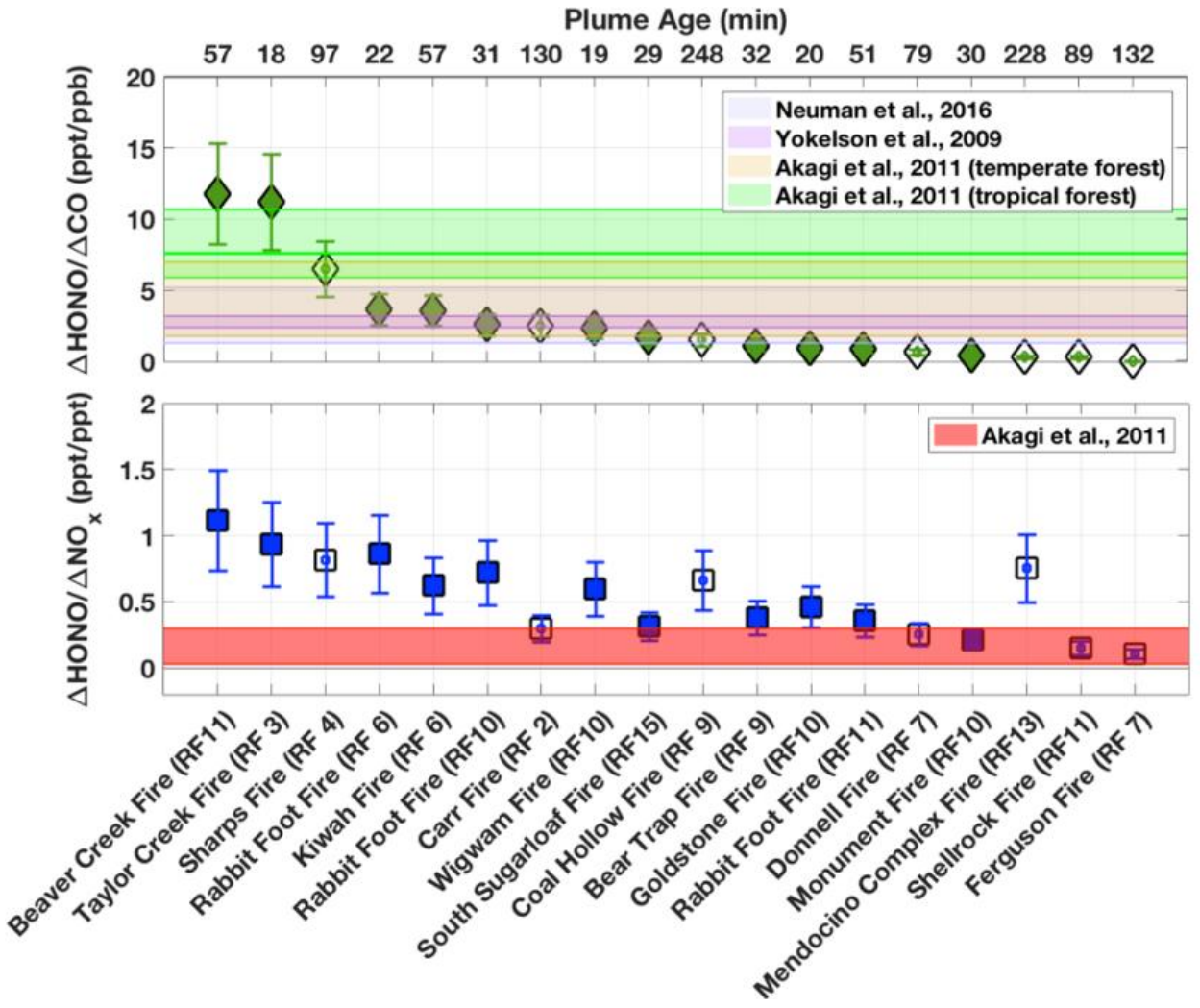

Figure S2.5. HONO enhancement ratios (derived from entire plume integration) relative to (top) CO and (bottom) NO_x in the freshest plume pass for each fire sampled, sorted in descending order of HONO to CO NEMR. The error bars represent the combined instrumental uncertainties summed in quadrature. The top axis shows the respective plume age. Selected reference HONO NEMR ranges from past campaigns are denoted for comparison. Plumes with physical ages above 1 h are shown in blank markers.

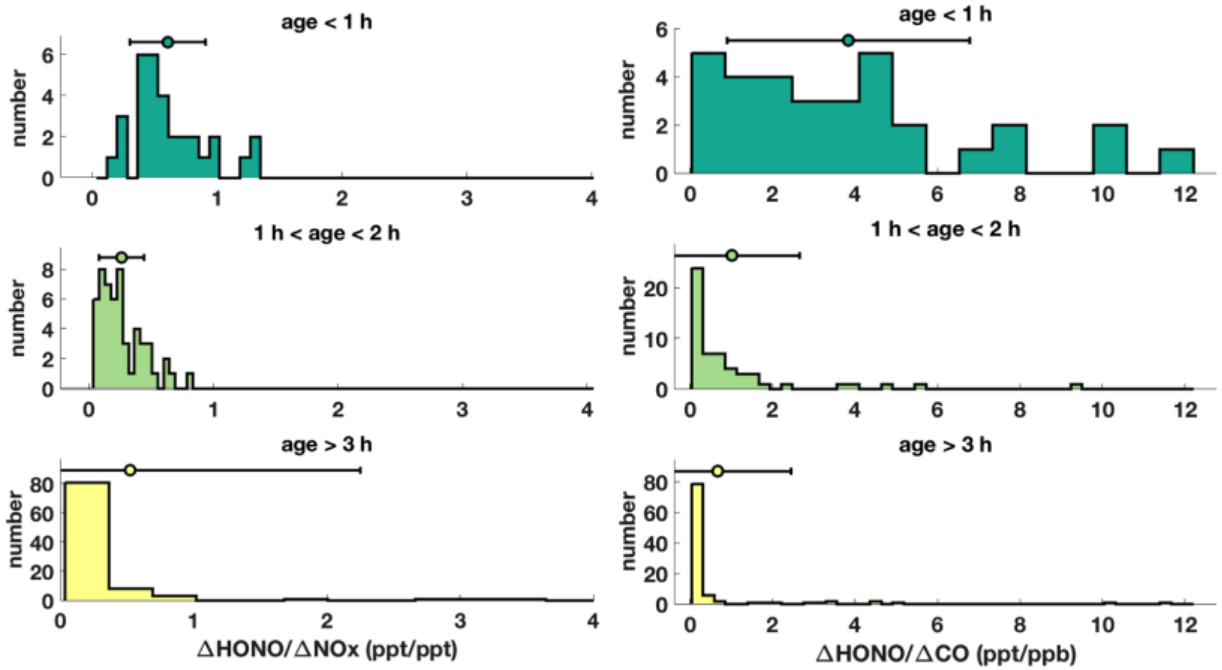

Figure S2.6. Histogram of HONO NEMR distribution across different age ranges.

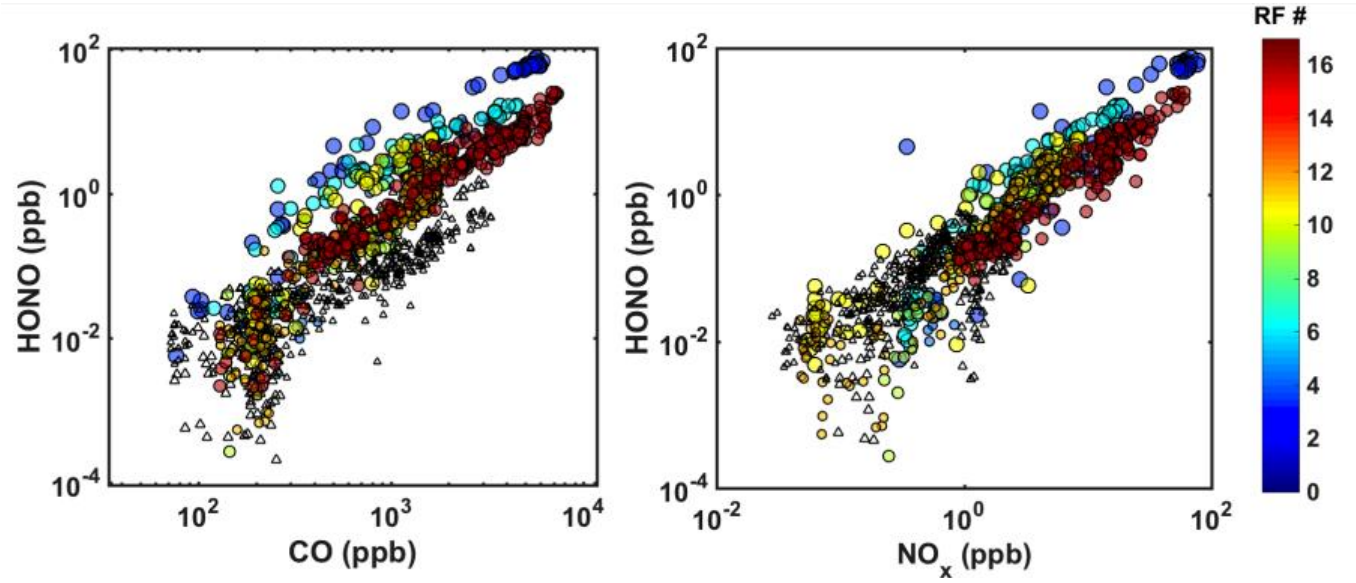

Figure S2.7. Scatter plot of (left) HONO to CO and (right) HONO to NO_x for the closest plume transect in each fire during the campaign. The symbols are sized inversely by age and colored by flight number. Plumes with physical ages greater than 1 hour are not colored (open triangles).

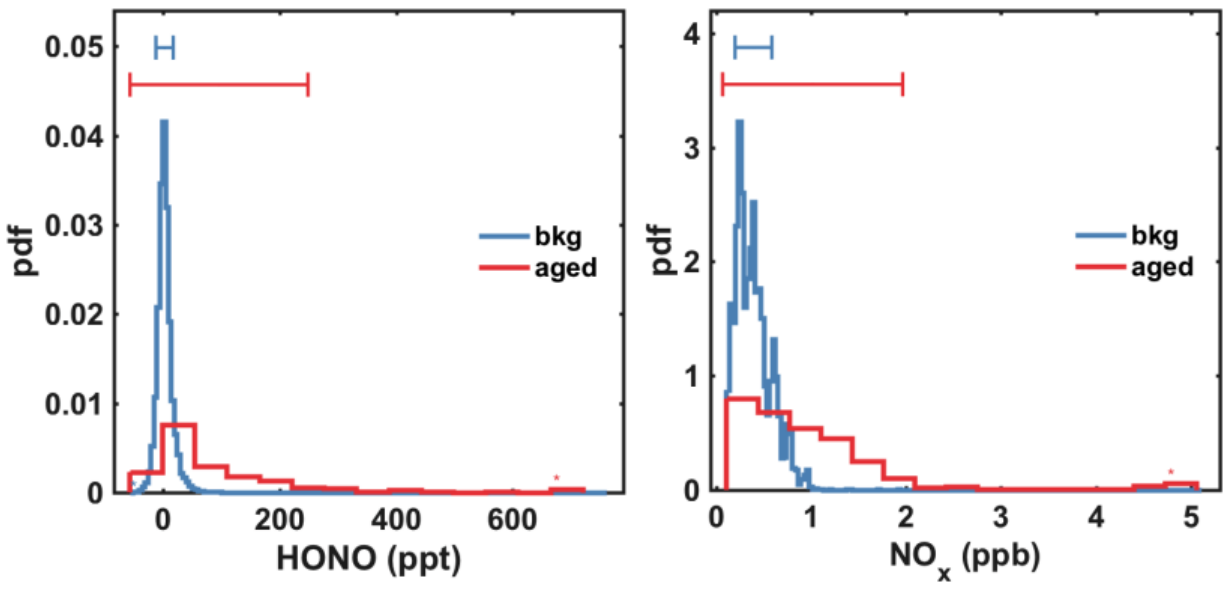

Figure S2.8. Frequency distribution histograms of (a) HONO and (b) NO_x of aged (>120 min) plume observations (green lines), and all background observations (blue lines) in RF03.

CHAPTER 3. OBSERVATIONS AND MODELING OF NO_X PHOTOCHEMISTRY AND FATE IN FRESH WILDFIRE PLUMES[2]

3.1 INTRODUCTION

Wildfires emit a wide variety of reactive trace gases and particulate matter (PM) that influence tropospheric chemistry, atmospheric radiation budgets, and air quality. The physical and chemical processes affecting the evolution of wildfire emissions are complex, and mechanistic-level understanding of the processes involved remains limited. In addition to being major sources of long-lived trace gases, such as methane (CH_4) and carbon dioxide (CO_2), wildfires typically emit a large amount of short-lived nitrogen-containing gases, such as nitrogen oxides (NO_x = NO + NO_2) and nitrous acid (HONO), carbon monoxide (CO) (Urbanski, 2014), volatile organic compounds (VOCs) (Evtyugina et al., 2013; Garcia-Hurtado et al., 2014) and particulate components such as organic aerosol (OA) (Garofalo et al., 2019; Liu et al., 2016; Palm et al., 2020) and black carbon (BC) among others (Kondo et al., 2011).

The release of reactive nitrogen species has a significant impact on the evolution of fire plume composition, by regulating the formation of secondary pollutants such as O_3 and particulate nitrate in biomass burning plumes (M. J. Alvarado et al., 2010; Arnold et al., 2015). The photochemical tendency of O_3 in wildfire plumes is complex, and the extent to which wildfires are considered net sources of tropospheric O_3 remains debated (Jaffe & Wigder, 2012). Part of the uncertainty stems from rapid near-field reactive nitrogen chemistry, often occurring at spatial and

[2] Reprinted with permission from Peng, Q., Palm, B. B., Fredrickson, C. D., Lee, B. H., Hall, S. R., Ullmann, K., et al. (2021). Observations and Modeling of NOx Photochemistry and Fate in Fresh Wildfire Plumes. *ACS Earth and Space Chemistry*, *5*(10), 2652–2667. https://doi.org/10.1021/acsearthspacechem.1c00086. Copyright 2021 American Chemical Society

temporal scales not represented in chemical transport models or accessed by observational platforms. In the near-field, large emissions of nitric oxide (NO) in an optically thick fire plume can lead to reaction or even titration of O_3 into nitrogen dioxide (NO_2) (McClure & Jaffe, 2018). Subsequent photochemistry, driven in part by HONO photolysis to release hydroxyl radicals (OH) and NO can fuel catalytic O_3 production that depends non-linearly on the total and relative concentrations of NO_x and VOCs, which are rapidly changing as the plume is advected and diluted with background air (He et al., 2020; Schroeder et al., 2017). Ozone production rates may be initially limited by either VOC or by NO_x, depending on the intensity of the fire and fuel being combusted, and then ultimately transition to NO_x limitation within the first few hours due to dilution and chemical conversion of the NO_x into species such as peroxyacetyl nitrate (PAN), other organic nitrates (OrgN), and nitric acid (HNO_3) in both the gas and particulate phases (Ditto et al., 2021; Juncosa Calahorrano et al., 2020; Roberts et al., 2020). The oxidation of NO_x into longer-lived temporary reservoir species, such as PAN, can lead to hemispheric scale impacts of wildfires on atmospheric oxidizing capacity, and tropospheric O_3 production, due to its ability to undergo long-range transport(M. J. Alvarado et al., 2010; Real et al., 2007). Therefore, understanding the fate of NO_x in the near field and how it depends upon fire conditions is critical to the prediction of O_3 production rates, oxidation capacity, and particulate matter evolution on regional and global scales (Lelieveld et al., 2016).

The photochemistry of biomass burning plumes has been studied previously in a number of field and laboratory studies. The photochemical evolution of wildfire plumes is challenging to comprehensively evaluate, in part because large suites of reactive species are generally not measured near enough to fires, and measurements made at remote downwind sites may miss photochemical regimes of early fire plume evolution (Tanimoto et al., 2015). Moreover, different

from urban or industrial plumes, wildfire plumes contain much higher PM and short-lived oxidant precursors (e.g., HONO), especially in the early stages of evolution. Several studies have explored wildfire emissions as well as partitioning of reactive nitrogen compounds, and showed substantial variability in emission factors and fractionation (Castellanos et al., 2014; Juncosa Calahorrano et al., 2020; Lindaas et al., 2021; Mebust et al., 2011). Alvarado et al. (2010) observed rapid PAN formation in a boreal smoke plume, with 40% of the initial NO_x emissions converted to PAN within 4 hours, while obtaining little clear evidence for O_3 formation. Similarly, Jacob et al. (1992) showed that the fraction of PAN in the sum of oxidized nitrogen (NO_y) increases with photochemical processing to about 30% in 3 hours in a boreal fire. However, Alvarado and Prinn (2009) simulated an Alaskan fire plume and found a low PAN/NO_y ratio of only 4% after 3 h. Alvarado et al. (2010) suggests that the significantly different fractions of PAN may stem from the different emission ratios of NO_x in the smoke plumes, where the initial value of NO_x/CO of 4% was an order of magnitude higher in Alvarado & Prinn (2009) compared to that in Jacob et al. (1992). Parrington et al. (2013) observed greater production of the sum of alkyl nitrates (ΣAN) compared to O_3 in boreal biomass burning plumes as O_3 production in the younger plumes was inhibited by high aerosol loading. Additional challenges to understanding fire plume chemistry and to developing broadly useful characterizations of it include changing combustion conditions, and thus emission rates and speciation over a given fire's lifecycle, heterogeneous fuel types and properties such as moisture content across different locations and with season for the same location.

Relatively few observational data sets are available with pseudo-Lagrangian sampling of near-field wildfire plume composition. Measurements of speciated reactive VOC, which will affect the production of PAN and ΣAN, and thus NO_x fate in fresh wildfire plumes, are rare and have

been relatively less well studied in part due to the analytical challenges associated with such measurements. Akagi et al. (2012) measured a prescribed fire plume in the first ~4 h after emission and observed rapid photochemical transformations where NO_x was converted to PAN at a rate twice as fast as that of oxidation to nitrate. In a later study, Akagi et al. (2013) further expanded the sampling conditions with a wider range of weather and fuel types, and observed large variability in initial emissions and photochemical O_3 production. Hodgson et al. (2018) profiled trace gas and particulate emissions from near-field measurements of discrete smoke plumes in Brazil, and illustrated that initial fire conditions can lead to substantial differences in emissions of chemical components. Observations made from single locations or otherwise in a spatially sparse manner may not be able to account for many of the non-linear physical and chemical changes that take place early within a smoke plume (Akagi et al., 2011; Hodshire et al., 2019). Given the challenge of sampling near-field wildfire plumes, plume modeling is critical to extend interpretation of limited field observations to other locations and time periods, as well as to better understand and predict the chemical transformations downwind. A combination of observation-based analyses and modeling techniques is thus needed for effectively interpreting how photochemical processes and other factors affect fire plume chemistry.

In this study, we use a suite of high time resolution *in situ* measurements of particles, trace gases, and meteorological variables collected with an instrumented National Center for Atmospheric Research (NCAR)/National Science Foundation (NSF) C-130 aircraft during the Western wildfire Experiment for Cloud chemistry, Aerosol absorption and Nitrogen (WE-CAN) campaign in summer 2018. We systematically examine the rapid daytime post-emission changes of reactive nitrogen, and use these observations to constrain and evaluate predictions from an explicit zero-dimensional chemical model of smoke photochemistry. We evaluate the model

results with emphasis on NO_x fate and the formation of secondary pollutants such as PAN, total nitrate, and O_3 in the first few hours of plume evolution. We focus on four research flights which most closely approximate Lagrangian sampling and provide a range of initial smoke chemical and physical conditions. We investigate the possible causes of model-observation disagreement and conduct sensitivity studies where initialization or chemical processes are altered in the model to examine the effects of model and measurement uncertainties on predictions. We conclude with a discussion of the major sinks of NO_x in different fires, and implications for model mechanisms.

3.2 METHODS

3.2.1 Site and measurement

The WE-CAN campaign used the NCAR/NSF C-130 research aircraft to investigate wildfire emissions and chemistry over the western United States from July 22 to September 14, 2018. It included observations of a large suite of trace gases and aerosol species, particle size distributions and optical properties, spectrally resolved solar actinic radiation, as well as meteorological variables such as 3-D winds, temperature, and humidity. Our analysis focuses on the portion of the campaign which took place from July 24 to August 31, 2018 when the C-130 aircraft was based out of Boise, ID. During this time, 258 smoke plume intercepts were conducted across 14 different research flights. Most research flights took off at ~14:00 local time and lasted for approximately 6 hours. Detailed descriptions of the sampling protocol and characteristics of the instrumentation have been published previously (Garofalo et al., 2019; Lindaas et al., 2021; Palm et al., 2020; Peng et al., 2020). Briefly, the NCAR Chemical Ionization Mass Spectrometer (CIMS) on board was operated to detect PAN and peroxypropionyl nitrate (PPN) by thermal dissociation followed by charge transfer reaction with iodide ions as described previously (Zheng et al., 2011). A proton-transfer-reaction time-of-flight mass spectrometer (PTR-ToF-MS) was

deployed to measure a suite of trace gases with measured ion m/z from 15 to 400 at 2 or 5 Hz frequency. More details on the instrument and analysis methods can be found in Permar et al. (2021). A high-resolution time-of-flight aerosol mass spectrometer (HR-ToF-AMS) was used to measure chemically-resolved submicron nonrefractory aerosol mass at 5 s time resolution (DeCarlo et al., 2006; Garofalo et al., 2019). The Advanced Whole Air Sampler (AWAS) collects VOCs for off-line analysis with up to 46 canister samples per flight during WE-CAN. The canisters took 2-5 seconds to fill, and were typically filled outside the smoke and then once close to the center of the plume intercept. More details on the instrument and analysis methods can be found in Benedict et al. (2019) Measurements of a suite of gas phase nitrogen-containing organic compounds (referred to as organic nitrate hereafter) were conducted by the University of Washington Iodide adduct Chemical Ionization Mass Spectrometer (UW-CIMS), as described in detail previously (Juncosa Calahorrano et al., 2020; Lee et al., 2014, 2018; Palm et al., 2019). In addition, UW-CIMS also detects a range of signals presumed to be VOCs including C_6H_6O and $C_6H_6O_2$, which may correspond to phenol and catechol, respectively (Palm et al., 2020). In the following sections, we will refer to these signals by their compound names for simplicity. Here, we define observed oxidized nitrogen compounds (ΣNO_y) as the sum of measured reactive nitrogen species from different instruments (ΣNO_y = NO_x + HONO + HNO_3 + pNO_3 + PAN + UW-CIMS organic nitrate).

3.2.2 Flight strategy

WE-CAN sampled over 20 major wildfires with a set of different fire sizes, fuel types, and burning conditions. The fuelbeds that burned during each of the WE-CAN flights were characterized using the Fuel Characteristic Classification System (FCCS) (Lindaas et al., 2021). The Modified Combustion Efficiency (MCE) has been widely adopted as a proxy of burning

conditions, and was calculated as $\Delta CO_2/(\Delta CO_2+\Delta CO)$ using the slope method following Lindaas et al. (2021). MCE values for the sampled plumes fall within the range of 0.85-0.95, implying mixed burning conditions including both flaming and smoldering. The plume-average wind speed is ~8.5 m s^{-1} indicating sufficient turbulence. During the campaign, 12 out of 23 fires were sampled in a pseudo-Lagrangian style, where the aircraft sampled the smoke through multiple downwind plume transects in a lawnmower pattern as it was transported downwind. *In situ* wind speed and wind direction measurements were used to position the aircraft to closely track the plume evolution. We focus here on four selected fires, for which we obtained the best approximation of Lagrangian measurements during the day: Taylor Creek Fire, sampled on research flight 3 (RF 3 on July 30), Sharps Fire (RF 4 on July 31), Donnell Fire (RF 7 on August 6), and Bear Trap Fire (RF 9 on August 9). The Taylor Creek Fire produced a particularly distinguishable and well-isolated plume that was injected above the boundary layer and entrained into the free-tropospheric flow while the C-130 aircraft was in the immediate vicinity. Thus, the smoke evolved without influence from factors such as clouds, deposition, or mixing with plumes from other sources. The Donnell Fire serves as an example of a more complicated sampling condition where multiple fires were active nearby. The pseudo-Lagrangian time since emission, also known as physical plume age, for each plume intercept is derived from the average observed wind speed in the plume and the distance of the aircraft sampling location at the plume intercept from the fire location. This approach is common among aircraft measurements of point sources and has been applied to other studies analyzing WE-CAN observations (Garofalo et al., 2019; Juncosa Calahorrano et al., 2020; Lindaas et al., 2021; Palm et al., 2020). The correlations between the physical plume ages and sampling time for the four fires are presented in Figure S3.1. It is found that the physical plume ages for Taylor Creek Fire plumes increases at nearly the same rate as the sampling time, which is

indicative of good pseudo-Lagrangian sampling. Potential biases in other fires are that the fire itself may be spatially extended such that different parts of the plume have originated from different fuels or undergone different trajectories and thus aging prior to being sampled, and the average wind speed (and direction) of the plume may not reflect the specific history experienced by the portion sampled. In some cases there may be multiple fire plumes in the region, and fire emissions may not be constant in time, such that the initial conditions may vary for each plume intercept. Thus, Lagrangian sampling of a single fire plume is a major assumption affecting interpretation of model–observation comparisons in our study, and other similar studies in the literature, and its validity is discussed in each of the four flight cases below.

3.2.3 Model setup

We use the Framework for 0-D Atmospheric Modeling (F0AM) box model with the Master Chemical Mechanism (MCM) v3.3.1 chemical mechanism, augmented with additional mechanisms and altered parameters as discussed below. Detailed descriptions of the model framework can be found in Wolfe et al. (2016) The MCM is a near-explicit chemical mechanism with detailed gas-phase chemical processes for a variety of compounds including 142 primarily emitted non-methane VOCs and its oxidation by different oxidants including OH, O_3, NO_3, and Cl. The MCM in its latest version 3.3.1 was adopted in this study (Jenkin et al., 2015). Additional mechanisms include the recent mechanism development from laboratory measurements for heterocyclic hydrocarbons (e.g., furans) and phenolics, which are found to significantly contribute to secondary product formation (Coggon et al., 2019; Decker et al., 2019; Joo et al., 2019).

The model was initialized for each of the four plume cases using the observed mixing ratios of O_3, NO, NO_2, CO, and various VOC using the maximum enhancement method (average mixing ratios over the plume core as identified by the highest 5% of CO for the transect) for measurements

obtained closest to the fire location as described in Peng et al. (2020) For species measured by AWAS, we used average mixing ratios from the youngest pass of each fire and average CO within the sampling time to calculate the relative abundance, and then multiply by the initialization CO mixing ratio to get the value for model initialization. The mixing ratios of selected trace gases used to initialize the model are presented in Table 3.1, and the full model initializations are shown in Table S3.1. We also used emission inventories to infer the concentrations of wildfire-emitted VOCs not measured by the suite of instruments onboard by scaling the reported biomass burning emission ratios by measured CO in the youngest plume (Hatch et al., 2018; Koss et al., 2018). 22 additional VOCs from the inventory which are also described in the model mechanisms including pentane, propene, and glyoxal are included in the model initialization (Table S3.2). The model simulates detailed gas photochemistry including 5832 species in 17224 reactions. A dynamic time-step solver available in MATLAB is used to integrate the rate equations (Wolfe et al., 2016). Physical parameters such as photolysis frequencies, temperature and pressure are constrained to measured values at each model step and held constant for model integration periods while chemical rate equations are evaluated. As the photolysis frequencies can be highly variable in time, we manually adjusted photolysis frequencies for NO_2 (j_{NO2}) in cases where the modeled NO/NO_2 could not agree to observations within uncertainty. Then the physical parameters are updated to the next closest set of observations in plume age and the process is repeated. Model predicted concentrations are written out every 380-750 seconds of plume evolution depending on the sampling duration and plume crossing intervals in the specific flight.

Figure 3.1 presents a schematic of NO_x fates in biomass burning plumes. During the day, oxidation of VOCs by OH leads to formation of an alkyl radical (R), which immediately reacts with O_2 to form a peroxy radical (RO_2). NO_x is subject to reactions with RO_x radicals ($RO_x = HO_2$

+ RO_2 + OH), the majority of which is produced through photolytic reactions of precursors such as HONO, and formaldehyde (HCHO) on the timescales of interest here (Peng et al., 2020). In low light and low NO conditions like in the core of dense plumes, dark reactions may also occur where NO_x is oxidized to NO_3 and subsequent oxidized nitrogen compounds. In MCM v3.3.1, RO_2 reactions with NO lead to either formation of alkyl nitrates ($RONO_2$) or RO and NO_2, and the yield of $RONO_2$ is dependent on the specific RO_2 species, with larger molecules tending to have higher yields. RO_2 reactions with NO_2 lead to formation of peroxynitrates (RO_2NO_2) with a subset being PAN-like acyl peroxynitrates that establish a thermal equilibrium with NO_2, allowing NO_x to be rereleased back to the atmosphere with subsequent air mass warming. NO_3 can be an important NO_x intermediate in the low light plume core. NO_3 can react with another NO_2 molecule to form N_2O_5, or alternatively, react with VOCs including alkenes and aldehydes to generate $RONO_2$ or nitric acid (HNO_3), respectively. Upon collision with aerosol, N_2O_5 can hydrolyze to form HNO_3, nitryl chloride ($ClNO_2$) in chlorine-laden aerosol (Goldberger et al., 2019; Thornton et al., 2010), or other organic nitrogen products (Ryder et al., 2015). The hydrolysis reaction of N_2O_5 is included in the default MCM with a fixed reaction rate, while in our simulations we updated the reaction rates with that derived from observational fits of N_2O_5 kinetics (Goldberger et al., 2019), and set the $ClNO_2$ yield to be <0.5, as would be likely for biomass burning plumes.

Plume dilution effects are described in the model by using a pseudo-first order dilution rate constant, k_{dil}, as equation 1 below:

$$d[X]/dt|_{dilution} = -k_{dil}([X]_t - [X]_{bg}) \quad \text{(Eq. 1)}$$

Regional background concentrations, $[X]_{bg}$, for each model species are obtained from observations made immediately adjacent to each plume intercept, as described in Peng et al. (2020), or default to zero if not observed. In the simulations, the $[X]_{bg}$ were updated to observed values at each model

time step. Plume dilution rates likely vary in time and across the plume, due to varying turbulence and out-of-plume concentrations, such that imposing a single dilution rate coefficient in the model may be inadequate. However, simulating dilution rates on a finer temporal and spatial scale requires a multi-dimensional modeling scheme that might sacrifice chemical complexity. We therefore derived the dilution rate coefficients (k_{dil}) by minimizing the root mean square error between the modeled and observed CO concentration decay, and applied the k_{dil} to all species in the model. This method assumes CO is a conserved tracer given the long CO chemical lifetime of 1 to 3 months and negligible secondary production (Griffin et al., 2007), which we confirmed with the model. An additional implicit assumption is that fire burning conditions, and thus CO emissions, were relatively constant over the timescales we examine here. This assumption is evaluated further in subsequent sections.

The uncertainty for the model simulations due to initial conditions was estimated to be around ±30% from sensitivity analyses varying initial HONO concentrations (Figure S3.2), and the observational uncertainties were calculated from the sum in quadrature of each corresponding instrument uncertainties. The uncertainty of plume ages is derived using standard deviations of wind speed measurements for each plume age bin.

3.3 Results and discussion

3.3.1 Box model baseline simulations for four fires

The flight tracks and locations of four fire plumes targeted in this study are summarized in Figure 3.2. The time series of CO and CH_3CN (acetonitrile) as typical biomass burning tracers are also shown. The drastically different emission intensity for the four fires is caused by a range of factors including fire intensity, fuel type, plume age, atmospheric conditions, etc. Burning conditions (e.g., flaming, smoldering) also influence the composition of smoke, as emissions of

VOCs and nitrogen compounds depend systematically on fire temperature (Roberts et al., 2020; Sekimoto et al., 2018). Flaming is a high temperature combustion phenomenon and is linked to more complete oxidation in biomass burning, while smoldering is the low-temperature form of combustion with incomplete oxidation of the fuel carbon and hydrogen, from which VOCs are predominantly emitted. The evolution of MCEs for the four fires are shown in Figure S3.3. The NO_x/CO ratio is a function of fire conditions since CO is a smoldering product, while NO_x is primarily produced in the flaming stage. As a result, these fires represent a set of different NO_x and VOC reactivities which enable examination of reactive nitrogen photochemistry across different chemical regimes. The interactions between NO_x and VOCs influence the absolute production rate of ozone by setting the NO/NO_2 ratio and peroxy radical abundance, which in turn affects the lifetime of NO_x and its conversion into reservoirs and thus the O_3 production efficiency of a fire plume (Ayres et al., 2015; Browne et al., 2013). The simulation of these different fire scenarios therefore allows us to classify different smoke plume observations in terms of the average plume conditions and chemistry, and to evaluate how the formation of secondary pollutants varies with fire conditions.

Figure 3.3 compares the first few hours of reactive nitrogen species evolution from both the baseline model and observations for the four selected fires. The lines represent the box model simulations, and diamonds denote observations, with shading and bars representing associated uncertainty in each, respectively. Two different simulations were run for the Sharps Fire where two sets of transects were sampled approximately 30 min apart, and the black curves and open diamonds represent the simulation and measurements during the second set of transects. A key difference among these four fires is the initial abundance of NO_x, i.e. that measured closest to the fire, and its ratio to VOC. Taylor Creek Fire and Sharps Fire are high in NO_x with a measured non-

methane VOC/NO_x ratio of ~6 and ~12, respectively; while Donnell Fire and Bear Trap Fire have relatively higher VOC abundances, with non-methane VOC/NO_x ratio of ~68 and ~50, respectively. Both chemical aging and/or fire-to-fire differences in emissions can play a role in the observed abundance of VOC and nitrogen compounds. The VOC/NO_x ratios may be dictated by NO_x loss to oxidation in plumes sampled at more than ~30 minutes of aging. The VOC/ΣNO_y is expected to be a more conservative tracer, especially in plumes having little contact with the surface. The VOC/ΣNO_y ratios are ~2.8, 6.0, 21, 16 in the youngest plume pass of Taylor Creek Fire, Sharps Fire, Donnell Fire, and Bear Trap Fire, respectively. In addition, the average HONO concentration which can play a vital part in the chemical evolution, varies across the fires sampled.(Palm et al., 2020) For example, in Taylor Creek Fire and Sharps Fire, the plume-average HONO/CO enhancement ratios are an order of magnitude larger than in Donnell Fire and Bear Trap Fire (~ 2.5 ppt/ppb *vs.*~ 0.3 ppt/ppb, respectively). Differences in the earliest plume age sampled cannot account for all of these differences, especially for example, Taylor Creek Fire vs. Bear Trap Fire, and thus emission characteristics between these fires are the likely cause.

The levels of O_3 precursors and their relative abundance revealed significant differences in the photochemical conditions of these fires, and may lead to large variations in the secondary products. As shown in Figure 3.3, we found in the four fires, HONO is well simulated for the rapid decay of its initial concentration spanning over 2 orders of magnitude, suggesting that HONO could potentially serve as an accurate photochemical clock in early stages of daytime plume transport. As plumes become more aged, the model tends to underestimate observed HONO, which implies possible secondary HONO sources not accounted for in the mechanisms, systematic biases in photolysis frequencies used in the model, deviations from sampling the center of plumes, or contributions from nearby fires mixing into the plume being studied. Additional secondary sources

of HONO are beyond the scope of this manuscript but certainly may impact multi-day aging of wildfire plumes. The main NO_x oxidation products ($NO_z = \Sigma NO_y - NO_x$) downwind of the fires are total (gas + particulate) nitrate ($TNO_3 = HNO_3 + pNO_3$) and PAN, accounting for over half of the total measured oxidized nitrogen after 1 h of aging on average, and the model simulations capture the trends and magnitude of both to within uncertainties. That said, the baseline model tends to overestimate NO_x mixing ratios with plume age possibly due to missing loss pathways, such as organic nitrate yields that are too low, or NO_2 reactive uptake, etc. This issue is explored in detail below.

In Figure 3.4, we show observations and model predictions of the same set of reactive nitrogen species as in Figure 3.3 but normalized by the observed or modeled CO mixing ratio, respectively, to isolate effects of chemical transformation from dilution. Observed plume transect data show that in all four fires, within 2 hours transport downwind from the transect location closest to the fire, NO_x in the plume was more than 80% lower than that measured in the youngest plume pass after dilution correction. The model reasonably reproduces the CO-normalized evolution of HONO, PAN, TNO_3, O_3, and HCHO for the different fire plumes as shown in Figure 3.4. Taylor Creek Fire and Sharps Fire produced more dilution-normalized TNO_3, and Bear Trap Fire plumes had comparable amounts of PAN formation as Taylor Creek Fire and Sharps Fire despite a much smaller NO_x/CO ratio. Consistent with past field studies (Akagi et al., 2012; M. J. Alvarado et al., 2010; Liu et al., 2016), the production rate of PAN ranged from 0.6 – 2 pptv/ppbv CO hr^{-1}. In the Taylor Creek Fire, PAN formation was observed to be approximately twice as fast as in the other plumes, a result of higher OH production with higher initial HONO abundance. Ratios of VOC pairs were used to evaluate how VOCs with different reactivity and lifetime varies with oxidant source. The toluene/benzene ratio is well captured for the four fire plumes, but the

decay of catechol/phenol ratios are generally underestimated, suggesting the possible underestimate of near-field OH and/or NO_3 concentrations in the model. However, the model significantly overestimates the observed NO_x/CO ratio by over a factor of 2 for the fire plumes sampled in Taylor Creek Fire and Sharps Fire, implying the model is either overestimating NO_x sources downwind of the fires, or that the model might be missing chemical sinks of NO_x that, while small compared to dilution, are nonetheless important for understanding the fate of reactive nitrogen compounds. We provide hypotheses and recommendations for improving the simulated NO_x decay relative to CO as a case study in the following section.

3.3.2 Case study of Taylor Creek Fire

We found that NO_x decay was not well reproduced by the box model in cases when we normalize both observation and simulations to CO, especially for high NO_x/VOC conditions as in Taylor Creek Fire and Sharps Fire. This mismatch may be caused by a change of NO_x emissions by fires over the time the plumes were sampled, or by a misrepresentation of NO_x loss and recycling such as through alkyl or peroxy nitrate chemistry. In addition, HONO was observed to be a large fraction of initial NO_x, and an error in instrument calibration could lead to NO_x in the model being biased high as the input HONO undergoes photolysis. However, the mismatch of NO_x occurred well after HONO is depleted (>0.8 h) (Figure 3.3), and varying the initial HONO by factors of 2 or more did not correct the model overestimate of NO_x/CO at plume ages > 1 hr, and too little HONO in the model led to underestimates of PAN, TNO_3 and O_3 (Figure S3.1). Thus, we dismiss this hypothesis. In this section, we investigate a set of possibilities that may lead to the NO_x discrepancy, using the Taylor Creek Fire as a representative case study. The hypotheses probed in this section may also apply in other flights and include time-varying emissions of NO_x

relative to CO, missing VOC from the model which might impact alkyl or peroxy nitrate formation, and inaccurate descriptions of alkyl or peroxy nitrate formation and decomposition rates.

3.3.2.1 Differential dilution and time-varying emissions

In wildfires, burning conditions change both temporally and spatially, which may lead to changing emissions, and aircraft studies that track a single plume in a pseudo-Lagrangian sense are unlikely to sufficiently sample a plume with changing burning conditions (Hodshire et al., 2019). Jolleys et al. (2015) noted that during the airborne measurements of boreal fire plumes, the fresh smoke appeared to be coming from more smoldering conditions, while the aged smoke appeared to be coming from more flaming conditions. The Taylor Creek Fire intensified as the C-130 aircraft was in the vicinity and a fresh isolated smoke plume was produced aloft of the boundary layer where smoke had not been present prior allowing for as close to Lagrangian sampling as possible. However, non-Lagrangian behaviors which include changing combustion or fuel conditions during the sampling period and old smoke lofted with the fresher plume, may still impact the observations and not be captured by our box model. Here, we evaluate changes in dilution and/or emissions that would be needed to explain observed NO_x/CO evolution by running multiple simulations having different initial concentrations of certain species, photolysis frequencies, and dilution rates.

The NEMR of total oxidized nitrogen could be considered as an indicator of overall nitrogen emissions from the fires. We constrain possible variations in nitrogen emissions from fires by showing the NEMR of total observed oxidized nitrogen with plume age for the four fires in this study (Figure S3.4). A notable decrease of 18% in $\Delta NO_y/(\Delta CO + \Delta CO_2)$ was found in Taylor Creek Fire between the youngest and most aged plume sampled, which can partly, yet not fully explain the more rapid loss of NO_x observed but not replicated by our base model run. Moreover,

this fire plume was the result of a rapid intensification of the burning conditions with a plume injection into the free troposphere observed in real time. As shown in the SI, the NO_x/CO emission ratio at the time of intensification and plume injection into the free troposphere would need to be nearly half that which occurred later after the plume was first injected. The MCE for each plume intercept of the Taylor Creek Fire (Figure S3.3) was nearly identical suggesting burn conditions were unlikely to have changed systematically to give lower NO_x/CO for the first emitted portion of the plume.

An additional complication to interpretation of this plume is the possibility that the plume dilution was more erratic such that a single diffusion time constant could not adequately describe dilution. We further investigated the role of differential dilution by separately modeling the subsets of plume intercepts to isolate the varying meteorology and background concentrations (see SI). We found that the simulation for the early plume transects (age < 1 h) exhibits similar degree of NO_x discrepancy as in the default model (Figure 3.4) despite using segment-optimal dilution rate coefficient (Figure S3.11), though the discrepancy decreases greatly for the separate simulation of later plume transects (age > 1h) possibly due to the removal of a large fraction of NO_x in the early stage (Figure S3.12). Therefore, time varying dilution alone is also not enough to explain the overestimates in NO_x, and additional photochemical sinks of NO_x are needed in the model to close the gap.

3.3.2.2 Missing RO_2 chemistry influencing organic nitrate formation

The relative importance of NO_x sinks may affect the production efficiency of O_3. When $RONO_2$ chemistry dominates NO_x sinks, O_3 production and NO_x loss (sequestration in organic nitrate) are essentially linked by their shared dependence on the RO_2 + NO reaction (Romer et al., 2018), and the production efficiency of O_3 per NO_x emitted will depend on the branching to

$RONO_2$. The model-observation discrepancy in the evolution of NO_x/CO may result from missing or underestimated alkyl and (acyl) peroxynitrate formation. Measurements of a suite of gas-phase oxygenated organic nitrogen compounds by UW-CIMS motivate this hypothesis.(Juncosa Calahorrano et al., 2020) We observe linear correlations between the observed enhancement ratios of these oxygenated organic nitrogen compounds and that of O_3, as shown in Figure 3.5, consistent with $RONO_2$ formation from the RO_2 + NO reaction which also net produces O_3. Given the strong correlation between their plume enhancement ratios with those of O_3, which we would not expect for reduced N (e.g. amines) compounds, we assume these oxygenated organic nitrogen compounds are organic nitrates, most likely $RONO_2$ but they could also include acyl and non-acyl peroxynitrates. Assuming mostly $RONO_2$ due to low instrument response of UW-CIMS to PAN observed in field tests, and applying a calibration value determined for isoprene-derived hydroxy nitrate, we calculated the net branching ratio for ΣAN from RO_2 reactions with NO in the smoke based on the slope of the correlation between O_3 and the sum over UW-CIMS detected organic nitrogen compounds as well as the modeled $[HO_2]/[RO_2]$ ratio. The observation-derived branching ratios for ΣAN were comparable for Taylor Creek Fire and Sharps Fire (~7%), while considerably higher in Donnell Fire (~15%). The observed correlations in Bear Trap Fire show larger variance due to changes in photolysis and plume conditions, and the branching ratios were calculated for the bifurcated portions separately, with the upper lobe ($\Delta O_3/\Delta CO > 0.04$ ppbv/ppbv) yield of ~7% and lower lobe ($\Delta O_3/\Delta CO < 0.04$ ppbv/ppbv) yield of ~19%. A summary spectrum of these nitrates is presented and discussed below, and their contribution to reactive nitrogen during WE-CAN have been discussed in Juncosa Calahorrano et al. (2020).

To summarize, the default model misses NO_x chemical sinks for the Taylor Creek Fire, but likely for the others discussed above as well. The model predicted organic nitrates are much lower

and of differing composition than those measured by the UW-CIMS. While calibration uncertainty in the UW-CIMS for such a wide suite of organic nitrates limits the comparison, the model predicted concentrations are more than a factor of 10 lower than that estimated by our calibration approach. It is unlikely the UW-CIMS is more than a factor of 10 more sensitive to organic nitrates than we assume here given physical constraints on ionization efficiency (Lopez-Hilfiker et al., 2016). Thus, we assume missing NO_x losses are related to organic nitrate formation. The default mechanism for furan and related compounds from Coggon et al. (2019) does not include organic nitrate formation pathways. We included organic nitrate formation into this subset but found furans, as measured, were not sufficient for explaining the missing NO_x loss. The default model includes explicit nitro-phenol formation, updated with the mechanism of Decker et al. (2019), for phenol, catechol, syringol etc and constrained with phenolic compounds observed by the UW-CIMS and the PTR-ToF-MS. Nitrophenolic formation is a potentially important source of organic aerosol mass and BrC in this plume, as we have previously shown but alone cannot account for the missing NO_x chemical sinks, unless there are other unmeasured phenolic precursors present at concentrations a factor of ~47 than catechol. While not impossible, it seems unlikely such a component would be unmeasured by both instruments at such a concentration. Moreover, we expect nitrophenolic compounds to strongly partition to aerosol and be measured at least partially as particulate nitrate by the AMS, which we can mostly explain with modeled inorganic nitrate as shown in Figure 3.6.

The vast majority of wildfire-emitted VOCs and oxygenated VOCs are not included in standard chemical mechanisms, and as such missing some RO_2 and, more importantly, associated organic nitrate formation is reasonable to expect. To incorporate unmeasured or unidentified VOC reactivity into the model, we included a lumped proxy RO_2 (XO_2 hereafter) with reaction pathways

of a generic RO_2. XO_2 reacts with NO to form alkyl nitrates ($XONO_2$) with a yield of 20% and/or forms peroxynitrates (XO_2NO_2) with similar formation and decomposition rates as those of methyl peroxynitrate. For these runs, NO/NO_2 ratios have been constrained to observation by adjusting NO_2 photolysis rates accordingly, though relaxing this constraint does not change the overall conclusions.

As shown in Figure 3.6, a constant 70 ppt XO_2 in the model which forms $XONO_2$ at 20% yield can correct the NO_x/CO discrepancy in the Taylor Creek plume. The evolution of NEMRs is shown in Figure S3.5. This added radical source represents a majority (50.5% - 90.8%) of total RO_2 during the ~2 h of aging. The associated reactivity affects the NO_x lifetime significantly, and changes the formation of PAN, TNO_3, and O_3, with a sequestration of NO_x in the form of alkyl nitrate of up to 12 ppb/ppm CO that was not represented in the default MCM mechanisms. The changes of species other than NO_x are mostly within the uncertainties of observation and model, and interestingly predictions of VOC ratios (e.g. phenol, furan, etc) are systematically improved relative to CO, yet the ratios of the VOC pairs remain largely unchanged, suggesting that reproducing the NO_x decay is necessary to simulating OH concentrations across the extent of plume aging. The enhancement of O_3 is relatively small despite addition of 70 ppt XO_2, as the effect of increased RO_2 is partly offset by the decreasing NO_x as well as the rapid transitioning between different NO_x regimes as the plume ages. Such a large pool of missing RO_2 seems unlikely, although the base model predictions certainly underestimate the variety and likely amounts of organic nitrates detected by the UW-CIMS. Adding an evaporative source of VOC from primary organic aerosol as an unmeasured RO_2 source was unable to produce enough missing RO_2 to reach that needed for XO_2, unless such RO_2 had $RONO_2$ yields >> 20% which is unlikely. However, the default model may well have $RONO_2$ formation rates that are too low for the suite

of RO_2 already represented in the model and as such XO_2 is solving both those underestimated existing pathways as well as missing VOC that have higher $RONO_2$ yields than the average RO_2 in the model. The model simulations of $\Delta OrgN/\Delta CO$ versus $\Delta O_3/\Delta CO$ in Figure 3.5 closely replicated the observed correlations, suggesting the inclusion of additional XO_2 and/or much higher $RONO_2$ yields is critical to account for the missing nitrogen reservoir in the model mechanisms.

To identify the possible NO_x loss pathways not accurately represented in the model, we compared the mass spectrum of measured and simulated organic nitrate for a selected downwind plume in Taylor Creek Fire as shown in Figure 3.7. Overall, the measured organic nitrates are almost an order of magnitude higher compared to the model output, suggesting that a significant portion of OrgN was not represented in the model mechanisms, especially the C4 nitrates, which are likely furan derivatives or fragmentation products from isoprene oxidations. Current furan reaction schemes developed in the laboratory did not include the alkyl nitrate pathways (Coggon et al., 2019; Decker et al., 2019), and increasing the alkyl nitrate yields in the model alone is not sufficient to account for the measured nitrate as well as the rapid NO_x loss, with the majority of observed OrgN absent from the model. Thus, introducing OrgN-forming XO_2 is necessary to help resolve this discrepancy by better representing the reservoir that the default model mechanisms fail to capture.

Organic nitrate detected by the UW-CIMS constitutes a substantial part (~20%) of ΣNO_y for the fires we investigated, as described in Juncosa Calahorrano et al. (2020) The sensitivity to individual organic nitrates in the UW-CIMS likely varies significantly (Lee et al., 2014; Slusher, 2004), and our use of a single average calibration factor for the UW-CIMS organic nitrates could explain some of the missing NO_y if our choice overestimates the instrument response to the average

organic nitrates present. There is a factor of 2 uncertainty in the measurement of organic nitrate, which may yield different assumptions of the importance of alkyl nitrate chemistry in wildfire plumes. However, taking into account the large overestimates in modeled NO_x, we have to invoke additional RO_2 reactivities to explain the rapid NO_x decay, consistent with the measured organic nitrate reservoir which is not represented by MCM mechanisms. We found that C4 and C5 compounds together explain over half of the observed organic nitrate, highlighting the importance of C4 and C5 precursor VOCs which are assumed to be mainly derivatives of furans and isoprene. In addition, the signal intensity of the *m/z* detected by CIMS that may correspond to hydroxy furanone ($C_4H_4O_3$) and methyl hydroxy furanone ($C_5H_6O_3$) were found to dominate in C4/C5 non-nitrate groups, respectively, which are major products formed from the oxidation of furan-type compounds (Aschmann et al., 2011, 2014; Coggon et al., 2019). This may imply that the oxidation of furan compounds is an important contributor to the formation of organic nitrates, but is currently lacking in the majority of model mechanisms, and as a result, the fate of NO_x.

The NO_x/CO discrepancy could also be resolved with a constant 2 ppt XO_2 that reacts with NO_2 to make peroxynitrates with formation and decomposition rates similar to that of PAN, i.e. the model could be missing acyl peroxynitrates (APN). This alternative produces a smaller, even negligible perturbation to total RO_2 in the model and therefore minor changes to predicted HO_x, TNO_3 and O_3. The updated model with acyl peroxynitrate-forming XO_2 predicts nearly equal amounts of acyl peroxynitrate (XO_2NO_2) as PAN by the end of the simulation, while other model-predicted APN (including PPN, APAN, etc) sums up to less than 30% of PAN and is not of sufficient abundance to explain the measured organic nitrates by UW-CIMS.

Our observations are not able to clearly distinguish between these two cases, or some combination of additional alkyl and peroxy nitrate formation over the base model. The observed

relationships between O_3 enhancements and that of PAN and the UW-CIMS organic nitrates compared to those predicted by the model suggest enhanced alkyl nitrate formation over peroxynitrate formation, given the stronger linear correlation observed between O_3 and organic nitrates for each individual flight, which is also predicted by the model. The NCAR CIMS did not quantify any APNs other than PAN and PPN during WE-CAN. Model simulations suggest that APN other than PAN, such as PPN or MPAN, could not account for the additional 12 ppb of XO_2NO_2 per ppm CO required to explain the NO_x/CO discrepancy. Thus, we conclude that the base simulation is significantly underestimating organic nitrate formation, equivalent in importance to PAN itself, both in the form of alkyl and acyl peroxynitrates other than PAN, PPN, and APN.

3.3.2.3 Heterogeneous Uptake of NO_2 and Other NO_x Loss Pathways

A third hypothesis for the NO_x/CO discrepancy is that the base model is missing heterogeneous uptake of NO_2 or other NO_x reservoirs to biomass burning aerosol particles. Considering the tremendous aerosol particle surface area in fresh wildfire plumes, the conversion of NO_x through reactive uptake could be non-negligible even if the reaction probability, γ, which describes the net loss per collision with aerosol particles, is small.

NO_2 reactive uptake to a variety of aerosol particle types has been measured and evaluated under laboratory conditions, with γ_{NO2} varying by 3 orders of magnitude (10^{-7}–10^{-4}) across different particle types (Ammann et al., 2005; Stemmler et al., 2007; Yabushita et al., 2009). We implemented NO_2 reactive uptake to aerosol particles following reaction R1 and Equation 2, which represents the pseudo-first order rate constant of NO2 reactive uptake to aerosol particles:

$$NO_2 + \text{particles} \rightarrow 0.5HONO + 0.5HNO_3 \quad \text{(R1)}$$

$$k_{NO2\_het} = 1/4 \cdot \gamma_{NO2} \cdot SA \cdot \omega \quad \text{(Eq. 2)}$$

where SA is the observed (dry) aerosol particle surface area concentration (cm^2 cm^{-3}) and ω is the mean molecular speed of NO_2. We prescribed the reaction products to be $0.5HNO_3$ + 0.5HONO based on Jacob (2000). Uncertainties associated with this assumption are discussed further below. Figure S3.6 shows that adding the NO_2 uptake mechanism significantly improves the simulation of NO_x/CO with plume age if γ_{NO2} is ~ $1x10^{-3}$, which is order(s) of magnitude higher than values reported in the literature. However, although the NO_x decay is better simulated, predictions of TNO_3 and of VOC decays are notably affected with systematic biases of excess TNO_3 and faster VOC decay than supported by the observations. If HONO is the only product of NO_2 reactive uptake, then OH is clearly too high throughout the simulation as indicated by significantly underpredicted furan and phenol mixing ratios. If HNO_3 is the sole product, predicted TNO_3 is almost doubled, and no longer consistent with the observations. Thus, NO_2 reactive uptake rapid enough to explain the observed NO_x/CO evolution with plume age is inconsistent with the observations if HONO and/or HNO_3 are the main products. If the NO_2 reactive uptake were to produce mostly particulate nitroaromatics, it is possible that the N in these would not be detected by the aerosol mass spectrometer (AMS) as particulate nitrate (Cheng et al., 2020; Farmer et al., 2010). However, we know of no evidence supporting such rapid aromatic nitration through NO_2 reactive uptake.

We have also explored other approaches to explaining the NO_x/CO discrepancy, including additional multi-phase chemistry of N_2O_5 and HO_2NO_2, as well as missing NO_3 reactivity or changing HO_2NO_2 thermal decomposition rates. However, these changes either had minimal effects on modeled NO_x decay rates, and/or the amount of changes needed to improve NO_x/CO predictions were either not supported by the suite of related observations and/or required changes well outside the uncertainty of recommended kinetic parameters.

In conclusion, our model results show that missing organic nitrate formation is the most likely explanation to the extent that changing fire conditions is not an option. We extended the above chemical changes to other fires (e.g. Sharps Fire) and found similar improvements in the model simulation suggesting that missing organic nitrate formation is likely a robust conclusion beyond our case study of Taylor Creek Fire. For the following sections, XO_2 chemistry leading to alkyl nitrate formation is introduced in the model simulations for Taylor Creek Fire and Sharps Fire to better approximate the observed NO_x decay for evaluation of NO_x fate.

3.3.3 Fates of reactive nitrogen in the fire plumes

Here, we examine the NO_y partitioning and evolution from both observational and modeling perspective for the four fires discussed above and assess how efficiently NO_x was converted to different reservoir products with different photochemical regimes across fires. In Figure 3.8, we show the sum of measured oxidized nitrogen compounds, ΣNO_y, for each fire in comparison to modeled NO_y speciation. In general, 87% of model-predicted NO_y values were within 20% of observations. Model simulations with XO_2 chemistry improved the agreement with measured ΣNO_y, particularly for the early plume transects when the sampling was supposed to be more Lagrangian. The model overestimate of ΣNO_y in the aged plumes in Taylor Creek Fire may be partially due to greater dilution as discussed in Section 3.2.1 while using a constant dilution rate coefficient in the model. The dilution-corrected ΣNO_y observation in aged plume intercepts was generally less than that observed in the intercepts closest to the fire, with the exception of Bear Trap Fire where the starting ΣNO_y (~ 22 ppb) is significantly lower compared to other fires investigated here (Figure S3.7). The measured ΣNO_y with dilution correction exhibits an overall decreasing trend with age for Taylor Creek Fire, Sharps Fire, and Donnell Fire at a rate of ~ 2-16 ppb h^{-1} suggesting missing or underestimated NO_y components.

In the model, the loss of NO_x to RO_2, in the form of PAN and other organic nitrates, is the dominant sink after dilution, and relatively more prominent in Donnell Fire and Bear Trap Fire which are VOC-rich. The observations of rapid PAN formation are in line with the model result which showed PAN/NO_y in smoke plumes increasing to 20% - 30% within 3 hours. Inorganic nitrate formation was the next most important NO_x loss pathway in all studied plumes implying an important coupling between OH sources and NO_x removal even in fresh wildfire plumes. VOC oxidation by NO_3 to form HNO_3 or organic nitrates represented a small, but perhaps non-negligible sink of NO_x, especially in NO_x-rich fires like the Taylor Creek Fire where modeled average NO_x loss rate to VOC-NO_3 reactions was ~1.9 ppbv h^{-1}, compared to the modeled average total NO_x chemical loss rate of ~27 ppbv h^{-1}, or in nighttime plumes which were not represented in this study. The VOCs contributing most to the NO_3 sink are catechol, syringol, and methylfuran.

3.4. Conclusion

We applied a near-explicit zero-dimensional chemical box model to simulate near-source photochemistry within wildfire smoke plumes from four fires sampled in a pseudo-Lagrangian manner during the WE-CAN campaign. A comprehensive data set with high time/spatial resolution collected during WE-CAN was used to initialize the model and to evaluate its ability to simulate the near field chemical transformations of reactive nitrogen in fresh wildfire plumes. Together the observations and modeling show that after dilution, formation of PAN and inorganic nitrate constitute major fates for NO_x, accounting for approximately 27% and 29% of NO_x conversion, respectively, across the four fires studied, consistent with previous research. In addition, the modeling supports an important role for HONO as a dominant radical source in fresh wildfire plumes, with concentrations reported by Peng et al.(Peng et al., 2020), necessary to capture the

observed decays of reactive VOC and formation rates of secondary products such as PAN, TNO_3, and O_3.

The default model setup significantly underestimated the dilution-corrected decay rate of NO_x in the two plumes with the highest NO_x, especially those sampled in Taylor Creek Fire. An evaluation of several possibilities together with the suite of observations suggests that the MCM-based F0AM model has inadequate descriptions of organic nitrate formation in fresh wildfire plumes. We showed that enhancing the abundance of organic nitrate-forming RO_2 (possibly from unidentified VOCs emitted by the fire) could resolve the model-measurement discrepancy in dilution-corrected NO_x loss. The implication being that an organic nitrate reservoir on the order of the same magnitude of PAN, either as other APN and/or $RONO_2$, was missing from the model. Observations from the UW-CIMS support a significant additional reservoir of C_2, C_3, C_4, and C_5 organic nitrates, among others, but the absolute abundance remains uncertain. The importance of the missing VOC reactivities may also depend on the photochemical schemes of the plume of interest, as plumes with higher NO_x/VOC ratios may be more sensitive to the missing VOCs in the model. Our analyses rule out other possibilities such as aerosol uptake of NO_2, N_2O_5, and HO_2NO_2 to form HONO and/or HNO_3 and missing NO_3-VOC reactivity. The magnitude of the discrepancy between the model simulations and the field observations depended somewhat on uncertainties related to plume dilution rates and time-varying emissions, but attempts to account for these aspects without additional NO_x loss pathways could not remove the discrepancy.

The series of modeling experiments constrained by observations helps increase our understanding of the factors determining the near-field chemical evolution of wildfire plumes, especially that of NO_x. Such evaluations can be used to incorporate the effects of sub grid-scale wildfire plume chemistry into regional and global scale chemical transport models as a means to

carry out higher-resolution chemistry simulations in the larger scale chemical transport model. Further studies would be required to represent photochemistry in plume-dispersing direction (e.g. cross-plume profiling) and understand the complex 3-D variations in the chemical processing of wildfire plumes to reproduce the highly non-linear chemistry.

3.5. SUPPLEMENTAL INFORMATION

3.5.1 Sensitivity analysis on the importance of HONO

In this section, we present sensitivity analysis on smoke modeling that helps isolate how initial HONO abundance affects plume chemistry.

By adjusting the HONO mixing ratios, we changed the oxidant strength, which controls the fates of VOCs. We varied the initial radical source strength by dividing the HONO mixing ratio by 2 and 4, respectively, to evaluate its role in driving photochemical evolutions in different fire plumes. Several box model studies have stressed the importance of HONO photolysis to the HO_x budget and found it to be particularly important for the formation of ozone and nitrogen reservoir species (Elshorbany et al., 2009). HONO represents a major source of OH particularly in fresh wildfire plumes, the photolysis of which contributed more than half of the total primary HO_x sources (Peng et al., 2020). While HONO photolysis can enhance the formation of NO and the general level of photochemistry within a smoke plume, therefore acting to increase O_3 production, they can also accelerate the oxidation of NO_x into stable nitrogen reservoir (e.g. HNO_3) via $OH+NO_x$ termination reactions resulting in the slowing of O_3 production. Thus, the net impact of directly emitted HONO on O_3 depends on the balance between these two effects. Results of sensitivity studies suggest that initial HONO concentration is an important factor in constraining photochemical processes. Striking differences can be found in the model simulation results with or without constraining observed HONO as shown in Figure S3.1, and the baseline model resulted

in overall better agreements with observations. Model results for Taylor Creek Fire and Sharps Fire from lower HONO indicate significantly smaller concentrations of PAN and nitrate than the concentrations calculated from the base model. Model results for Donnell Fire and Bear Trap Fire which are in a low HONO and NO_x environment did not show such significant changes. The modelled NO_x decay is significantly slower compared to observations, possibly owing to missing RO_2 sources.

3.5.2 Plume source back-extrapolations

To probe the chemistry and emissions that can explain the observations in the eight plume transects made closest to the fire, corresponding to physical plume ages ranging from 21 min to 2.3 hours, we used the freshest plume transect as the model initial condition, and set dilution to be the rate derived from observed CO decay. Initial NO/NO_2 and $HONO/NO_2$ ratios were set equal to those in the freshest plume pass and held constant for subsequent simulations which varied initial HONO or NO_x concentrations. Seven simulations were run, each aiming to match the observations in one of the next seven downwind plume intercepts by adjusting dilution rates, HONO photolysis frequency and initial HONO and NO_x in the model until the observation-model agreement was achieved for CO and HONO (Figure S3.8). The detailed initial conditions in the model that brought the best agreement with observations in each downwind transect are included in Table S3.4. As shown in Figure S3.8, we found that the plume intercepts could be separated into two categories of evolution overall, where the early transects (physical age < 0.8 h) converge to a state with relatively slower NO_x decay rates and higher O_3 and PAN formation, while later transects were subject to faster NO_x decay and resulted in less PAN and O_3 production. The initial NO_x mixing ratios required to match NO_x in later plume transects ranged from 30-39 ppb (Figure S3.8), or a NO_x/CO emission ratio of 5.3-6.9 pptv/ppbv, while those required for the fresher plume

transects were ~51-61 ppb, or NO_x/CO emission ratios of 9.1-10.8 pptv/ppbv. This inferred shift of NO_x/CO emission ratios is possible if old smoke, possibly from smoldering conditions with a much lower NO_x/CO ratio, was mixed throughout the boundary layer and then lofted to higher altitudes with the fresher plume originating from intensification of the fire to flaming conditions. A box model as we employ would not be able to replicate such a situation and thus could be the cause of the NO_x/CO discrepancy in the model at the furthest downwind edge of the Taylor Creek Fire plume.

3.6 TABLES

Table 3.1. Model initialization of select trace gases for four selected fires sampled in a pseudo-Lagrangian way. Additional trace gases are used as inputs where available and listed in Table S3.1 and S3.2.

Compounds (ppbv)	Taylor Creek Fire	Sharps Fire, set 1	Sharps Fire, set 2	Donnell Fire	Bear Trap Fire
CO	5630	2550	2921	3562	1883
NO	8.1	1.0	6.9	1.5	1.2
NO_2	56.5	28.6	17.7	8.6	5.1
HONO	72.4	32.3	10.6	3.8	3.0
O_3	92.1	49.1	61.7	136.0	68.1
C_4H_4O (Furan)	6.1	3.4	3.5	3.5	3.1
C_6H_6 (Benzene)	7.2	3.8	4.9	7.4	3.0

HNO_3	21.0	10.0	11.8	16.3	4.6
$C_7H_8O_2$ (Guaiacol)	1.3	0.4	0.26	0.04	0.25
PAN	6.2	2.1	4.2	6.8	3.8
C_5H_8 (Isoprene)	1.9	1.6	1.6	1.2	1.1
C_2H_4 (Ethene)	80.8	30.4	11.1	67.0	22.6
$C_6H_6O_2$ (Catechol)	2.1	0.66	0.42	0.07	0.4

Table S3.1. Model initialization for four selected fires sampled in a pseudo-Lagrangian way.

Compounds (ppbv)	Taylor Creek Fire	Sharps Fire, set 1	Sharps Fire, set 2	Donnell Fire	Bear Trap Fire
CO	5630	2550	2921	3562	1883
CH_4	2218	2077	2132	2148	2105
NO	8.1	1.0	6.9	1.5	1.2
NO_2	56.5	28.6	17.7	8.6	5.1
HONO	72.4	32.3	10.6	3.8	3.0
O_3	92.1	49.1	61.7	136.0	68.1
C_4H_4O (Furan)	6.1	3.4	3.5	3.5	3.1
C_6H_6 (Benzene)	7.2	3.79	4.9	7.44	3.0
HNO_3	21.0	10.0	11.8	16.3	4.6
$C_7H_8O_2$ (Guaiacol)	1.3	0.41	0.26	0.04	0.25

PAN	6.2	2.1	4.2	6.8	3.8
C_5H_8 (Isoprene)	1.9	1.6	1.6	1.2	1.1
C_2H_4 (Ethene)	80.8	30.4	11.1	67.0	22.6
$C_6H_6O_2$ (Catechol)	2.1	0.66	0.42	0.07	0.4
Syringol	1.3	0.4	0.26	0.04	0.25
M3F (3-methylfuran)	2.6	2.0	2.1	1.5	1.9
HCHO	52.3	14.7	16.4	38.6	11.5
CH_3CHO	50.5	28.2	34.1	37.2	20.3
C_2H_5CHO	7.9	7.6	7.6	12.5	5.3
MVK	3.4	1.5	1.5	2.0	1.2
MACR	1.7	0.8	0.78	1.1	0.7
PPN	0.84	0.2	0.49	0.8	0.4
Phenol	1.5	1.4	1.2	0.9	0.5
o-Xylene	0.7	0.3	0.3	0.4	0.2
a-pinene	1.4	0.6	0.6	0.01	1.1
p-Xylene	0.66	0.43	0.18	0.61	0.56
Cresol	0.3	0.1	0.16	0.2	0.1
1-butene	3.8	1.9	0.55	1.7	1.4
n-butane	0.9	1.0	0.45	1.7	1.1

Table S3.2. Inferred VOC mixing ratios from emission inventories used to initialize the box model.

Compounds (ppbv)	Taylor Creek Fire	Sharps Fire, set 1	Sharps Fire, set 2	Donnell Fire	Bear Trap Fire
Ethylbenzene	0.89	0.40	0.46	0.56	0.30
1,2,3-trimethyl-Benzene	0.24	0.11	0.12	0.15	0.08

Styrene	1.59	0.72	0.82	1.01	0.53
Benzaldehyde	0.79	0.36	0.41	0.50	0.26
Pentane	1.05	0.48	0.54	0.66	0.35
Hexane	0.66	0.30	0.34	0.42	0.22
Heptane	0.38	0.17	0.20	0.24	0.13
Octane	0.28	0.13	0.15	0.18	0.09
3-methyl-1-butene	0.63	0.29	0.33	0.40	0.21
1-Hexene	1.69	0.77	0.88	1.07	0.57
b-pinene	2	0.91	1.04	1.27	0.67
Acrolein	5.5	2.49	2.85	3.48	1.84
2-Butenal	2.54	1.15	1.32	1.61	0.85
Butanal	0.51	0.23	0.26	0.32	0.17
Pentanal	0.38	0.17	0.20	0.24	0.13
Propene	25.4	11.50	13.18	16.07	8.50
Butadienes	10.2	4.62	5.29	6.45	3.41
Glyoxal	9.6	4.35	4.98	6.07	3.21
Sesquiterpenes	0.85	0.38	0.44	0.54	0.28
Methylglyoxal	2.1	0.95	1.09	1.33	0.70
Biacetyl	2.6	1.18	1.35	1.64	0.87
Acetol	2.2	1.00	1.14	1.39	0.74

Table S3.3. Molecular composition of selected organic nitrate compounds and their corresponding MCM name and molecular weight.

Molecular composition	MCM name	Molecular Weight
$C_5H_9NO_4$	ISOPBNO3	147.1
$C_4H_7NO_5$	MVKNO3	149.1
$C_2H_2N_2O_8$	NO3CH2PAN	182.0
$C_9H_{15}NO_4$	C96NO3	201.2

$C_{10}H_{17}NO_4$	APINANO3	215.2
$C_{10}H_{16}NO_5$	APINNO3	230.2
$C_7H_8NO_8$	NCRESO2	234.1

Table S3.4. Model initial conditions to back-extrapolate the seven youngest plume intercepts in Taylor Creek Fire.

plume #	1	2	3	4	5	6	7
CO (ppb)	5630						
NO (ppb)	7.6	6.2	6.4	4.0	4.9	3.7	3.9
NO_2 (ppb)	53.1	43.5	44.6	27.7	33.9	26.0	27.1
HONO (ppb)	68.1	55.8	57.2	35.5	43.5	33.3	34.8
j(HONO) s^{-1}	4.87e-4	3.65e-4	4.87e-4	3.05e-4	5.18e-4	5.18e-4	5.24e-4
kdil (s^{-1})	2.4e-4	2e-4	2e-4	3.4e-4	3.4e-4	2.9e-4	4.7e-4

3.7. FIGURES

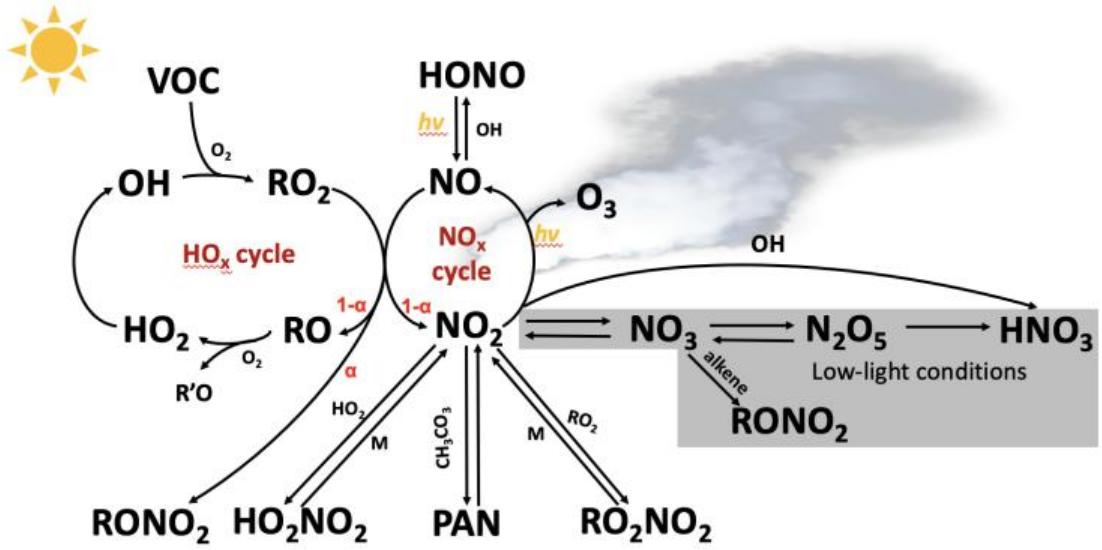

Figure 3.1. Schematic of NO_x fates in fire plumes.

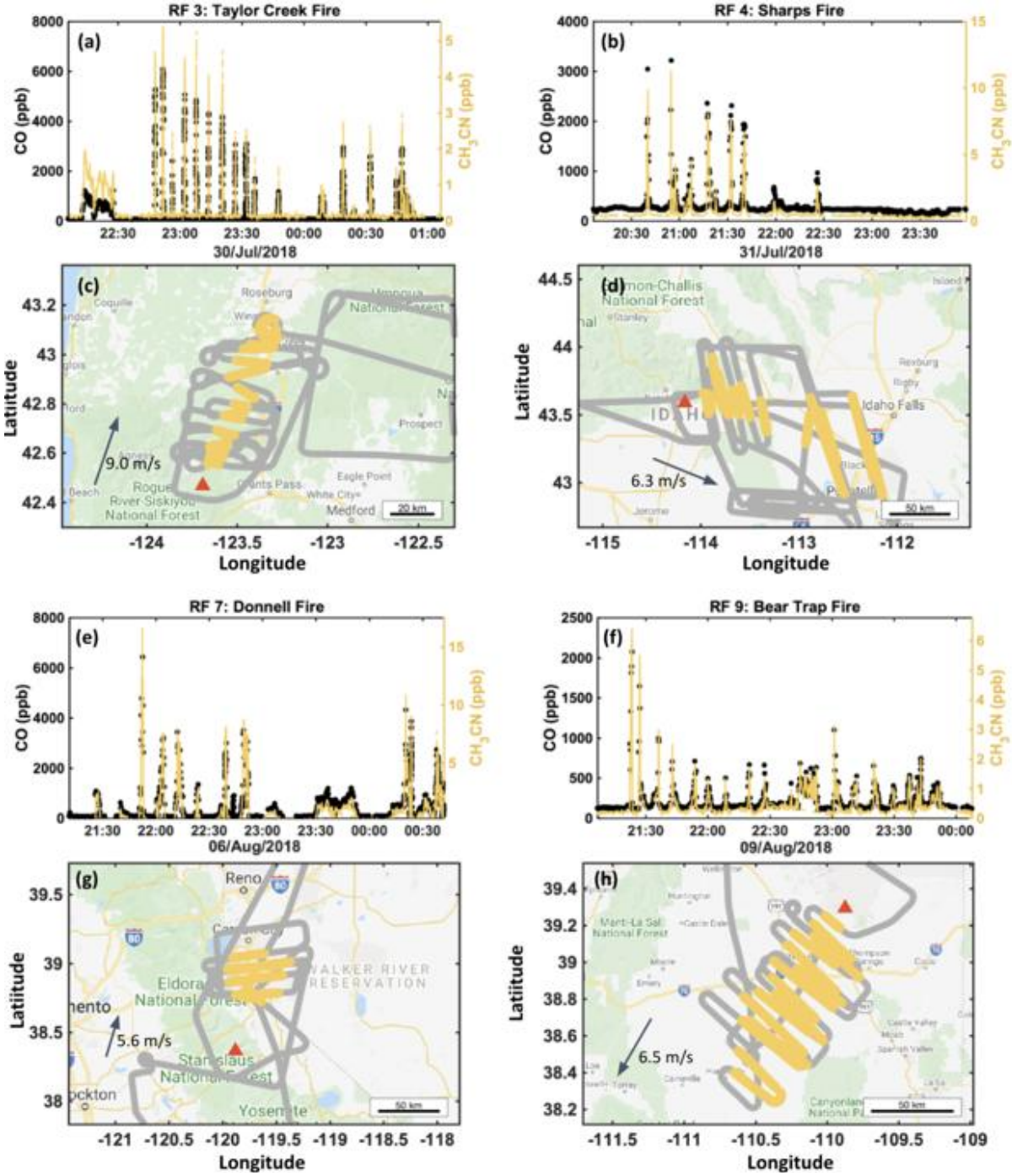

Figure 3.2. Time series (UTC time) of CO mixing ratios and CH_3CN mixing ratios for four different fires sampled during WE-CAN: (a) Taylor Creek Fire, (b) Sharps Fire, (e) Donnell Fire, (f) Bear Trap Fire. Corresponding maps ((c), (d), (g), (h)) with flight tracks (gray) are enclosed, and plumes identified to be close to pseudo-Lagrangian are shown in yellow. Approximate fire locations are denoted with red triangle symbols. Average in-plume wind directions and speed as well as distance scales are shown for each fire.

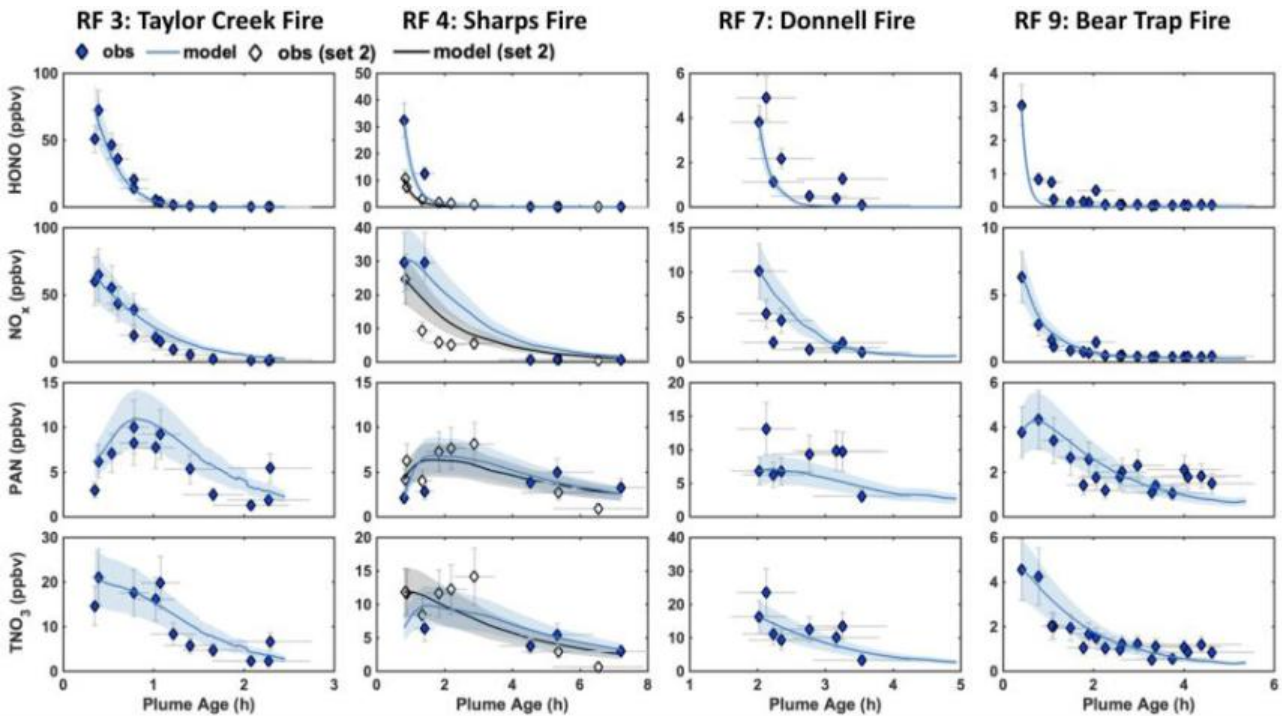

Figure 3.3. Baseline box model simulation (curves) and field observations (diamond) of reactive nitrogen compounds mixing ratios (ppbv) for the four fires. Two simulations were run for Sharps Fire where the fire was sampled at two sets of transects. Note that the y-axis scales are different across the fires. The horizontal error bar represents the uncertainty in the smoke ages derived from the standard deviations of wind speed, and the vertical error bar denotes the measurement uncertainties derived from the sum in quadrature of instrument uncertainties.

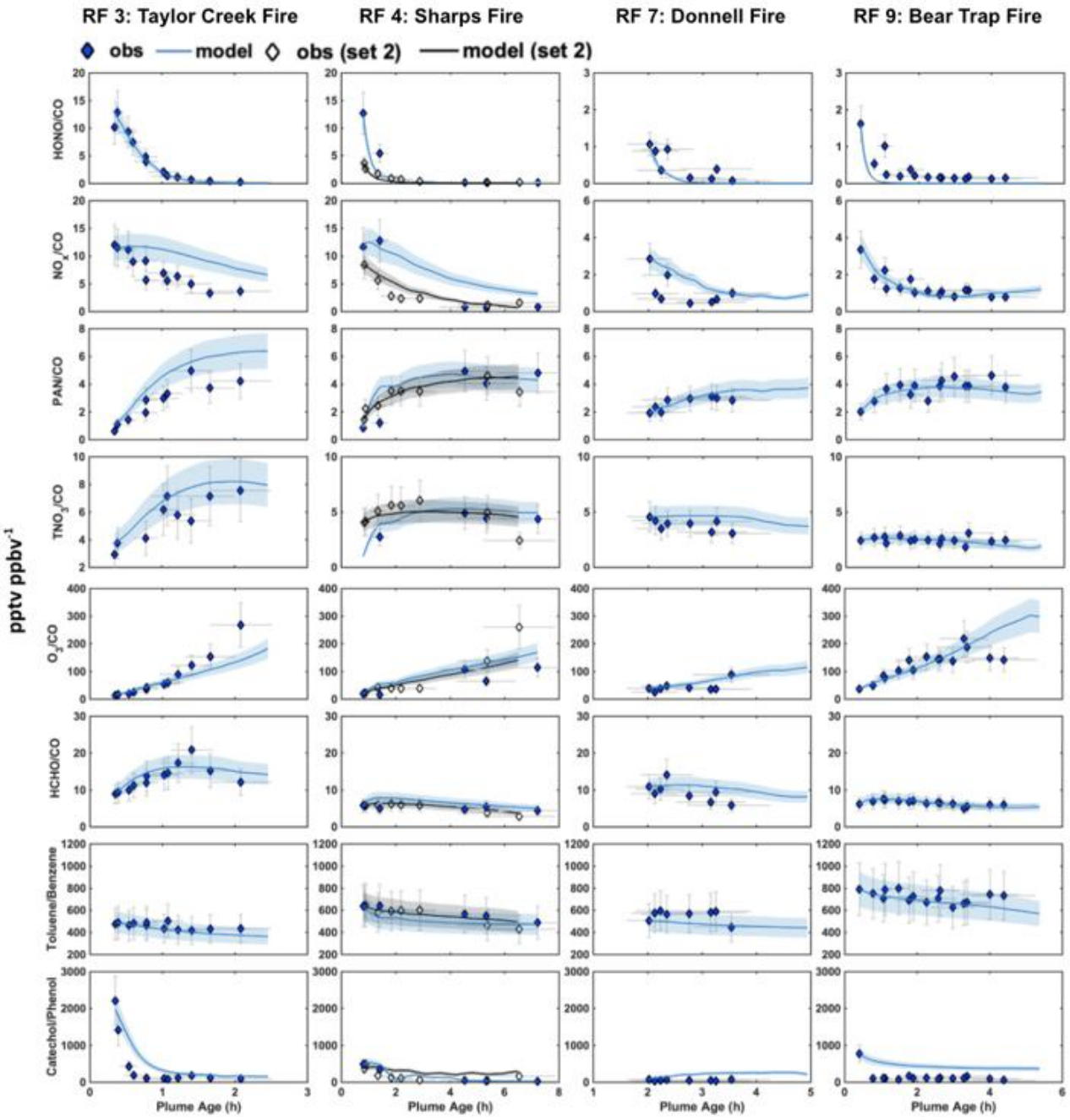

Figure 3.4. Box model simulation (curves) and field observations (diamond) of the CO-normalized reactive nitrogen compounds mixing ratios, secondary products, and ratios of selected VOC pairs (pptv/ppbv) for the four fires. Note the y-scale differs across panels. The horizontal error bar represents the uncertainty in the smoke ages derived from the standard deviations of wind speed, and the vertical error bar denotes the measurement uncertainties derived from the sum in quadrature of instrument uncertainties.

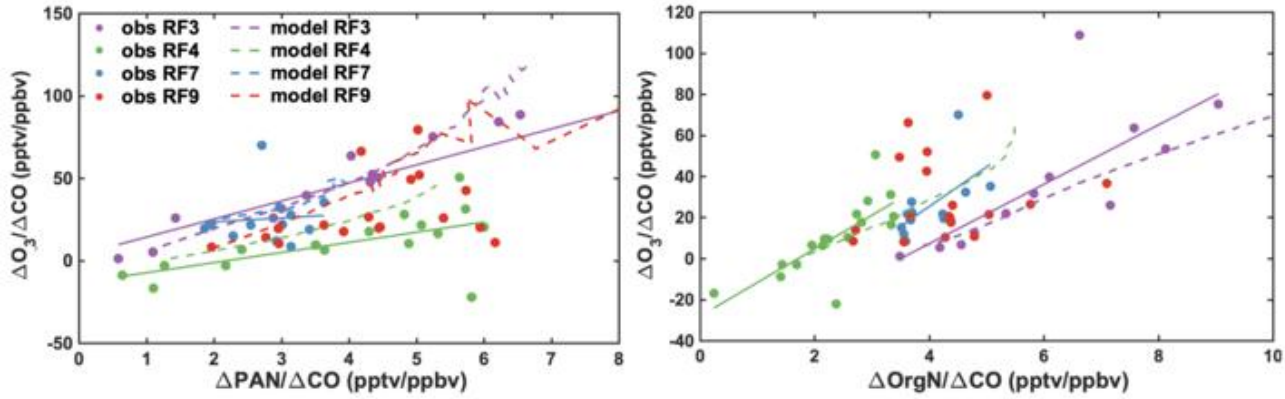

Figure 3.5. Correlation between O_3 enhancement ratios and enhancement ratios of PAN (left) and organic nitrate (right) for all four fires. The first set of transects were used for constraining Sharps Fire simulation. Linear fits (solid line) were applied to the observations (dot), and modeled correlations with additional peroxy radical XO_2 (dashed line) were included for comparison. Simulations for Donnell Fire and Bear Trap Fire were omitted in the plot here as the linear correlations in these plumes were relatively low, likely due to two different regimes sampled in those plumes (with higher or lower VOC/NO_x).

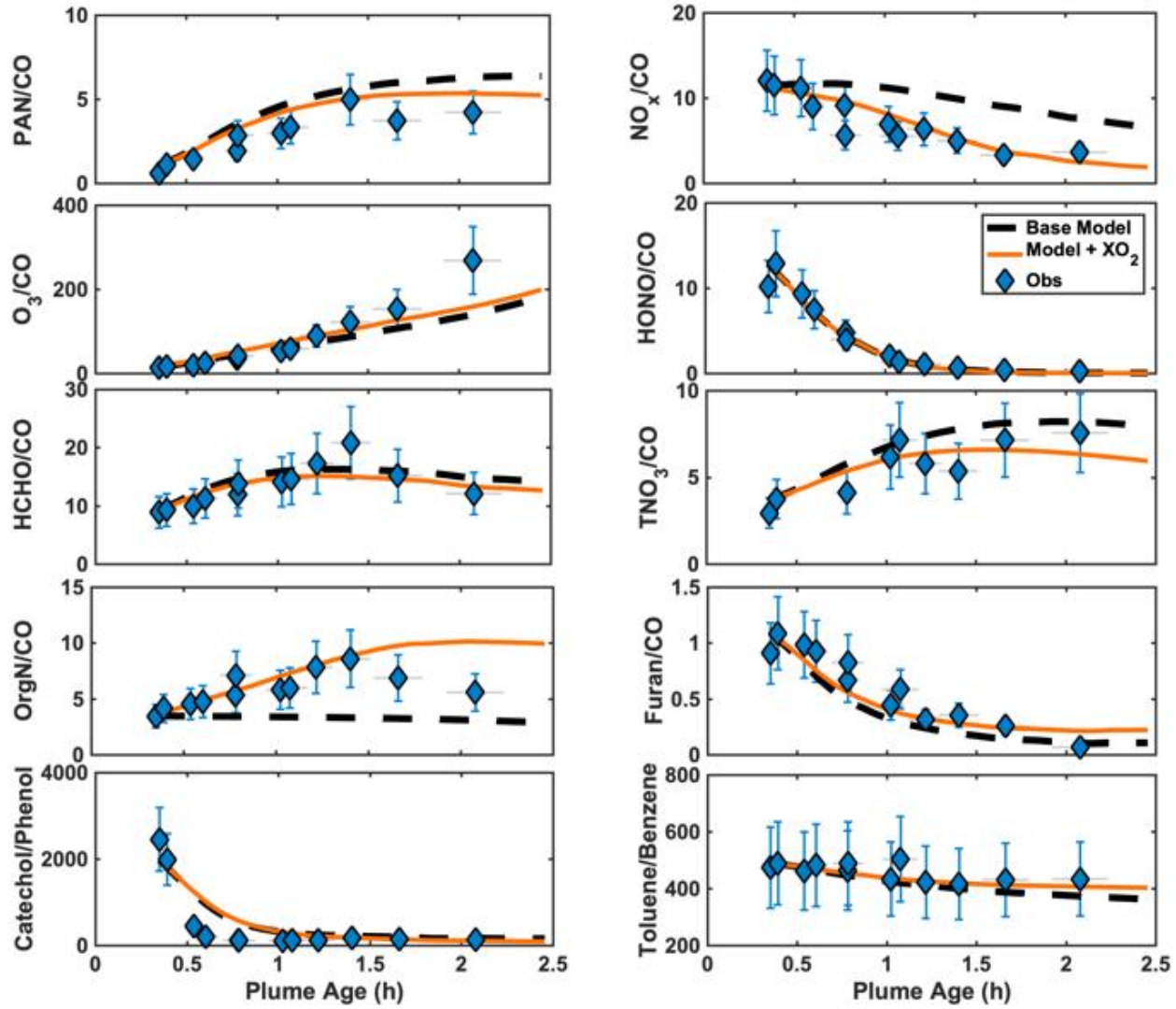

Figure 3.6. Comparisons of CO-normalized mixing ratios and ratios of selected VOC pairs (pptv/ppbv) in base model simulation (dashed black curve) and nudged model with a constant source of 70 ppt XO_2 addition with an effective organic nitrate yield of 20% (orange curve). Blue diamonds denote field observations of plume transect mixing ratios for Taylor Creek Fire.

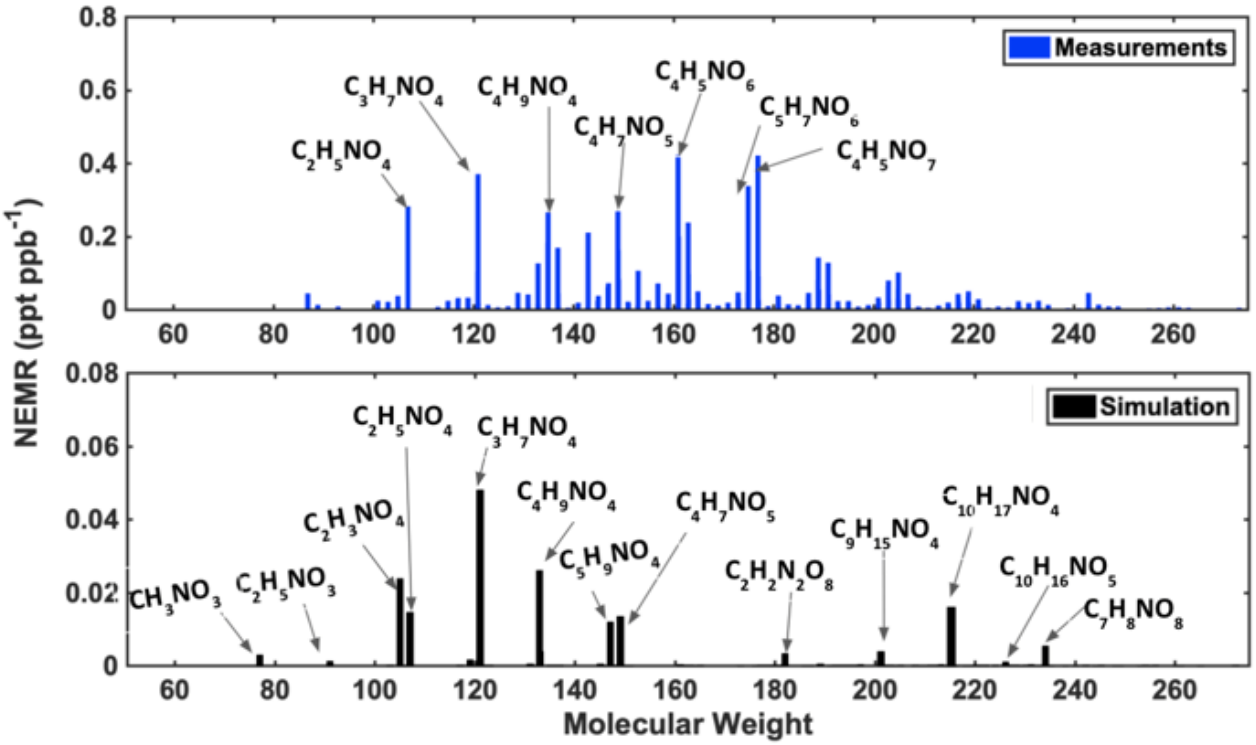

Figure 3.7. (a) Summary of mass spectrum showing NEMR for organic nitrogen signals relative to CO in aged smoke in the UW-CIMS during the Taylor Creek Fire. The masses with highest NEMRs are labeled. (b) modeled mass spectrum for organic nitrates at the same plume age in Taylor Creek Fire. The MCM names for specific nitrate compounds are summarized in Table S4.

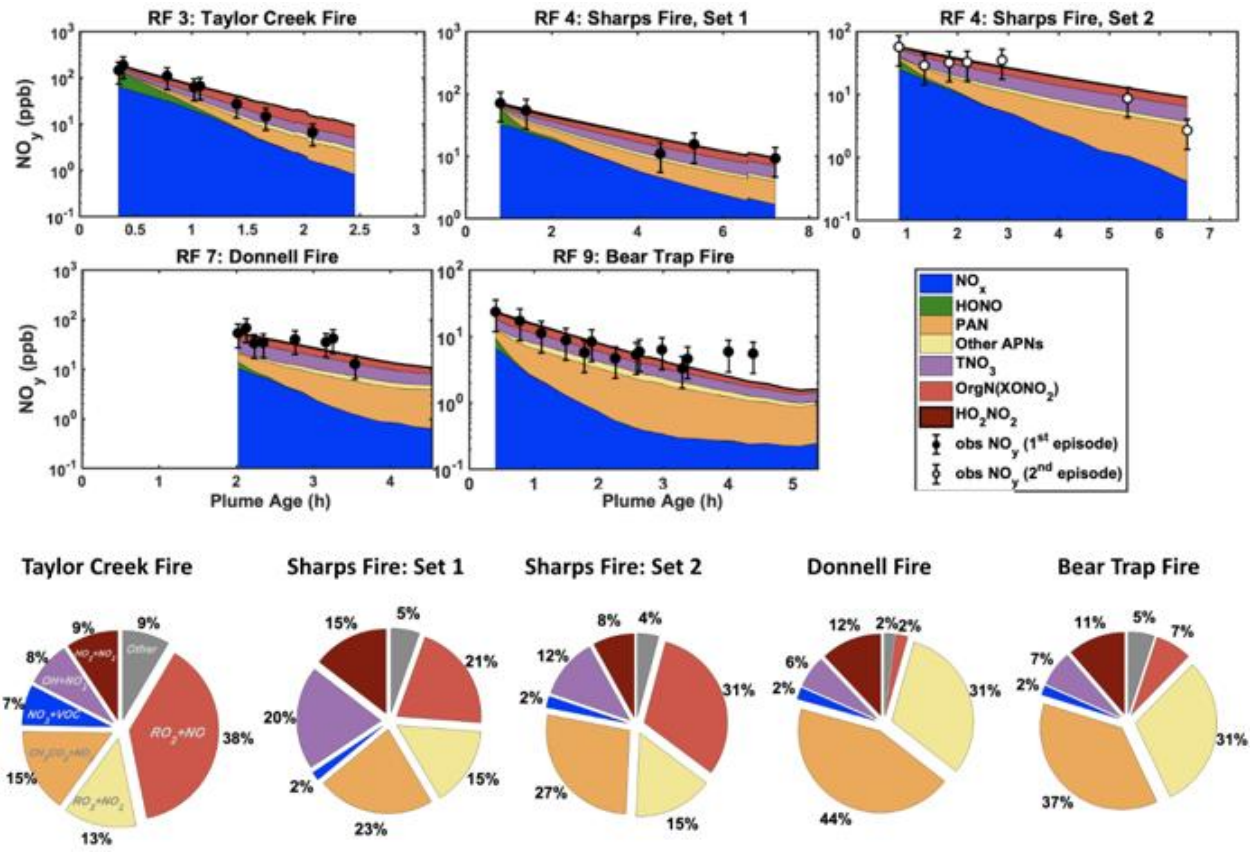

Figure 3.8. Modeled NO_y partitioning and observed $\sum NO_y$ in four fires. Black dots denote field observations of mixing ratios of $\sum NO_y$ measurements; blank symbols denote the second set of measurements in Sharps Fire. The pie charts show the flight-average modeled NO_x sink rates for the corresponding fires.

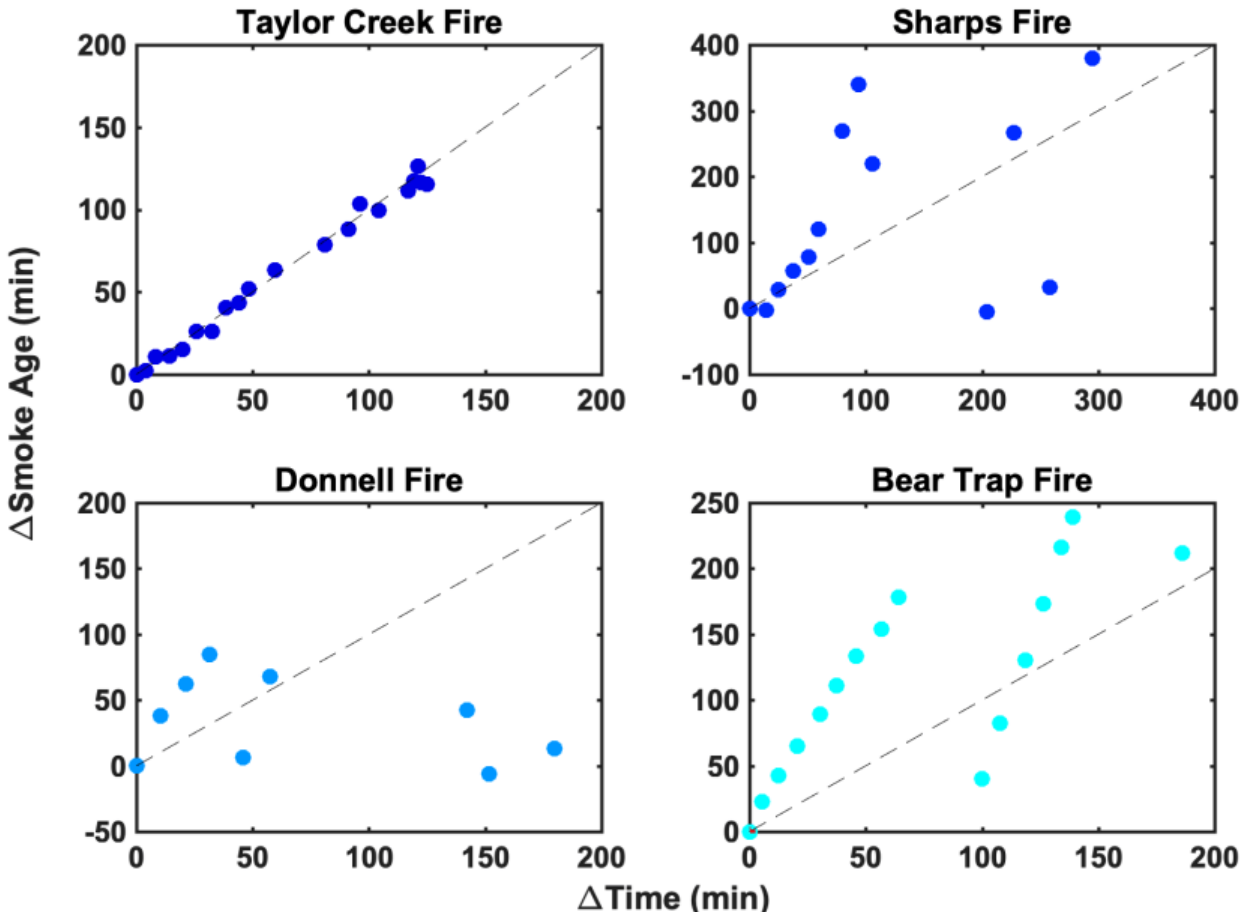

Figure S3.1. Correlations between physical plume age and sampling time for the four fires. The black dashed line is a reference 1:1 line.

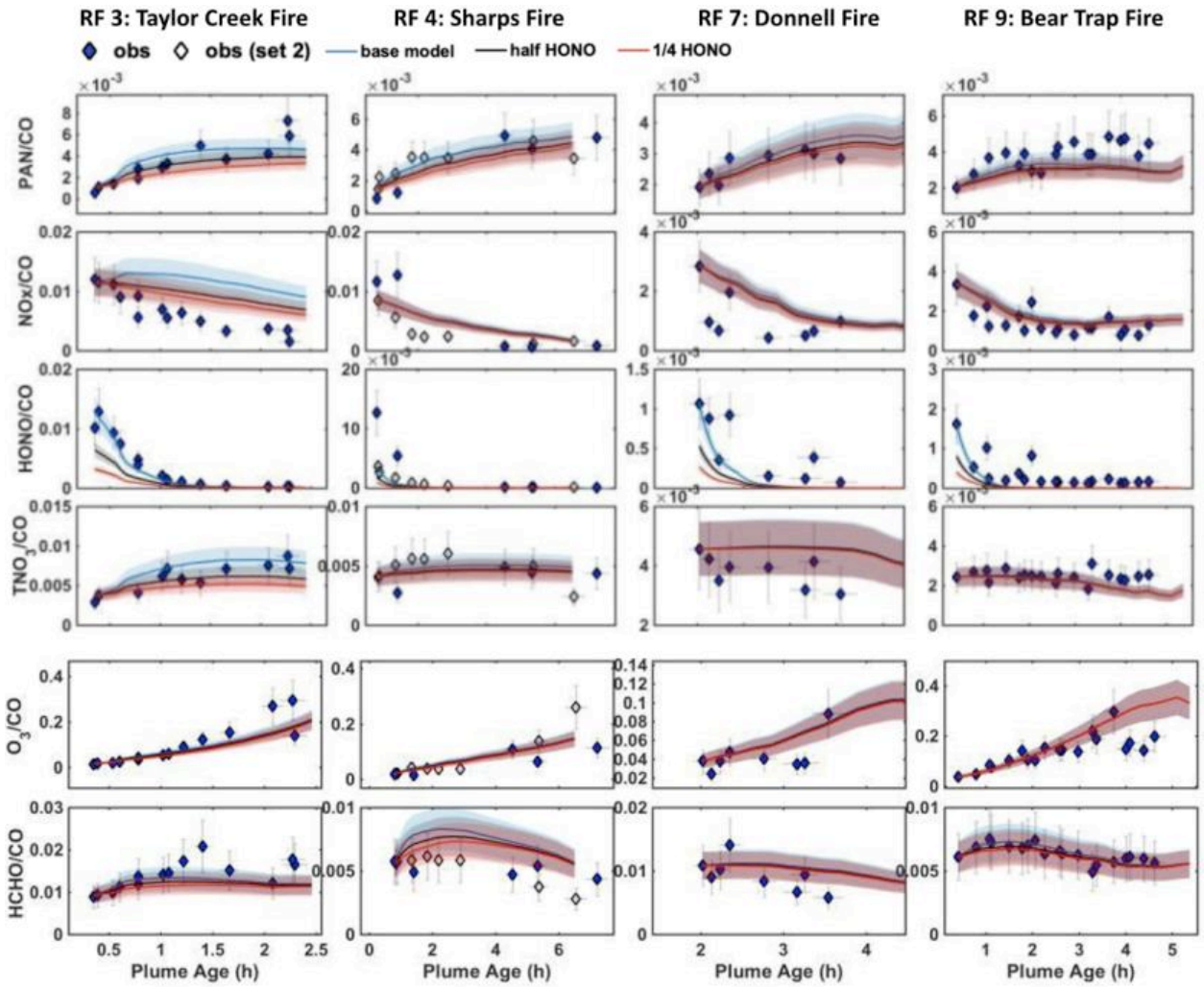

Figure S3.2. Box model simulation (blue: base case; black: ½ HONO initialization; red: ¼ HONO initialization) and field observations (closed diamond: first set of transects; open diamond: second set of transects) of normalized mixing ratios (ppbv ppbv^{-1}) for the four fires. Shading indicates ± 20% uncertainty for corresponding runs.

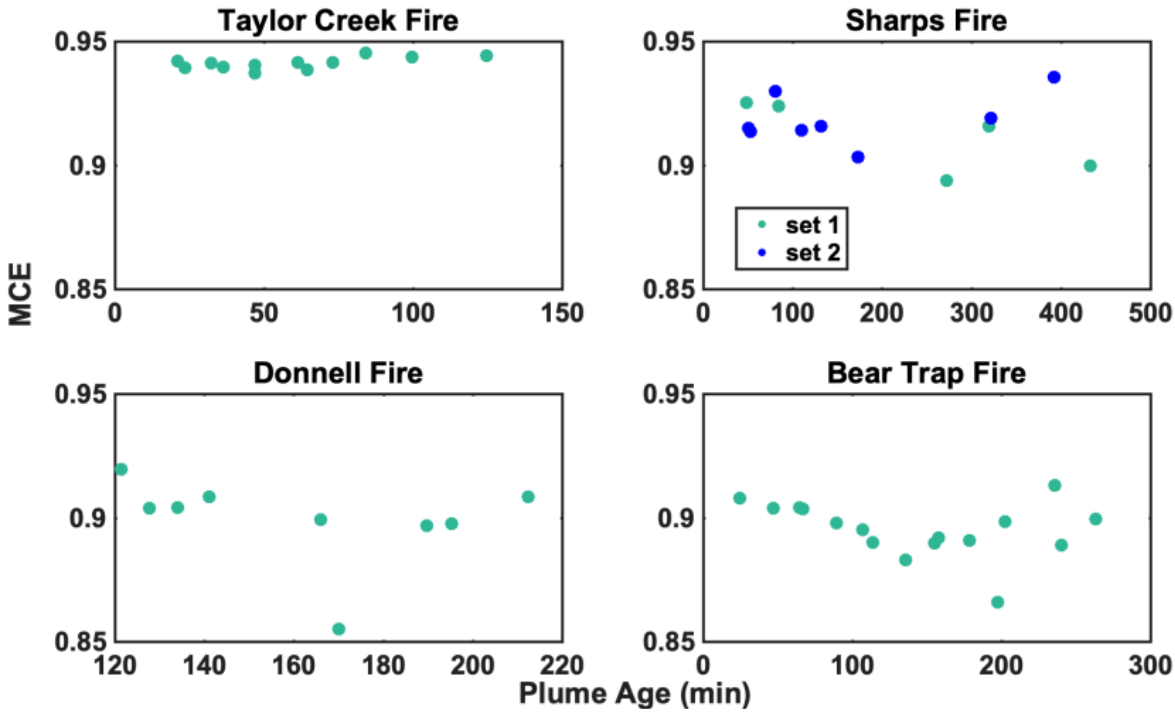

Figure S3.3. Evolution of MCE with plume age for the four fires.

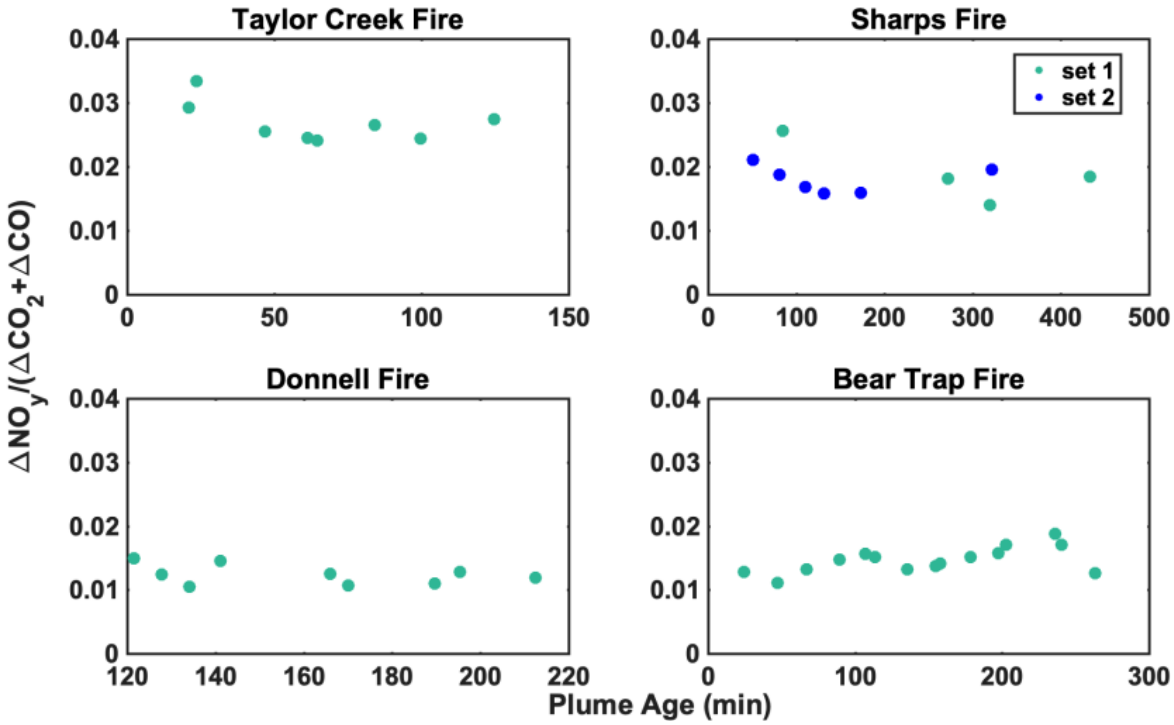

Figure S3.4. Evolution of $\Delta NO_y/(\Delta CO + \Delta CO_2)$ with plume age for the four fires.

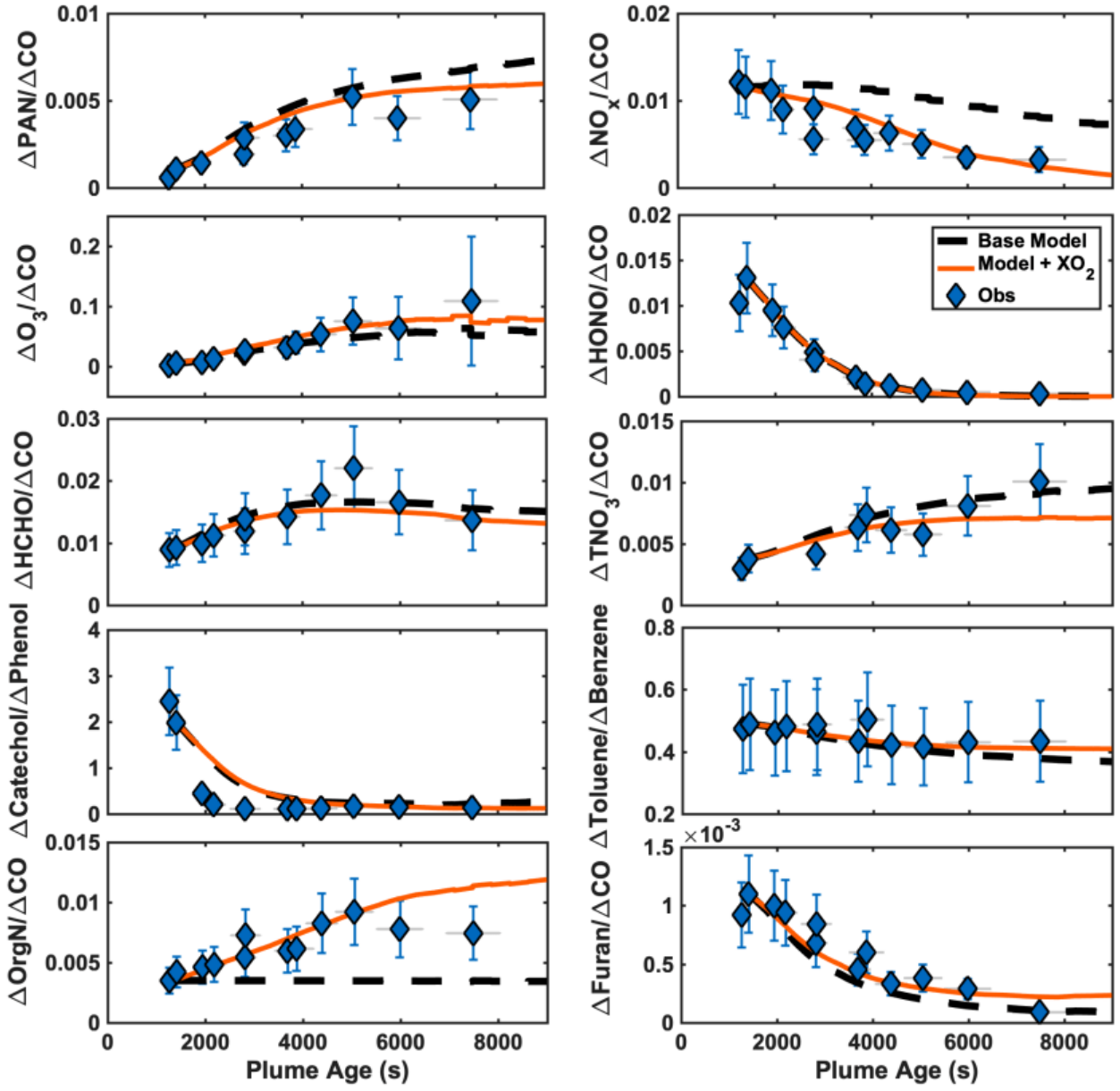

Figure S3.5. Comparison of NEMRs (ppbv/ppbv) from base model simulation (dashed black curve) and nudged model with a constant source of 70 ppt XO_2 addition with an effective organic nitrate yield of 20% (orange curve). Blue diamonds denote field observations of plume transect mixing ratios for Taylor Creek Fire.

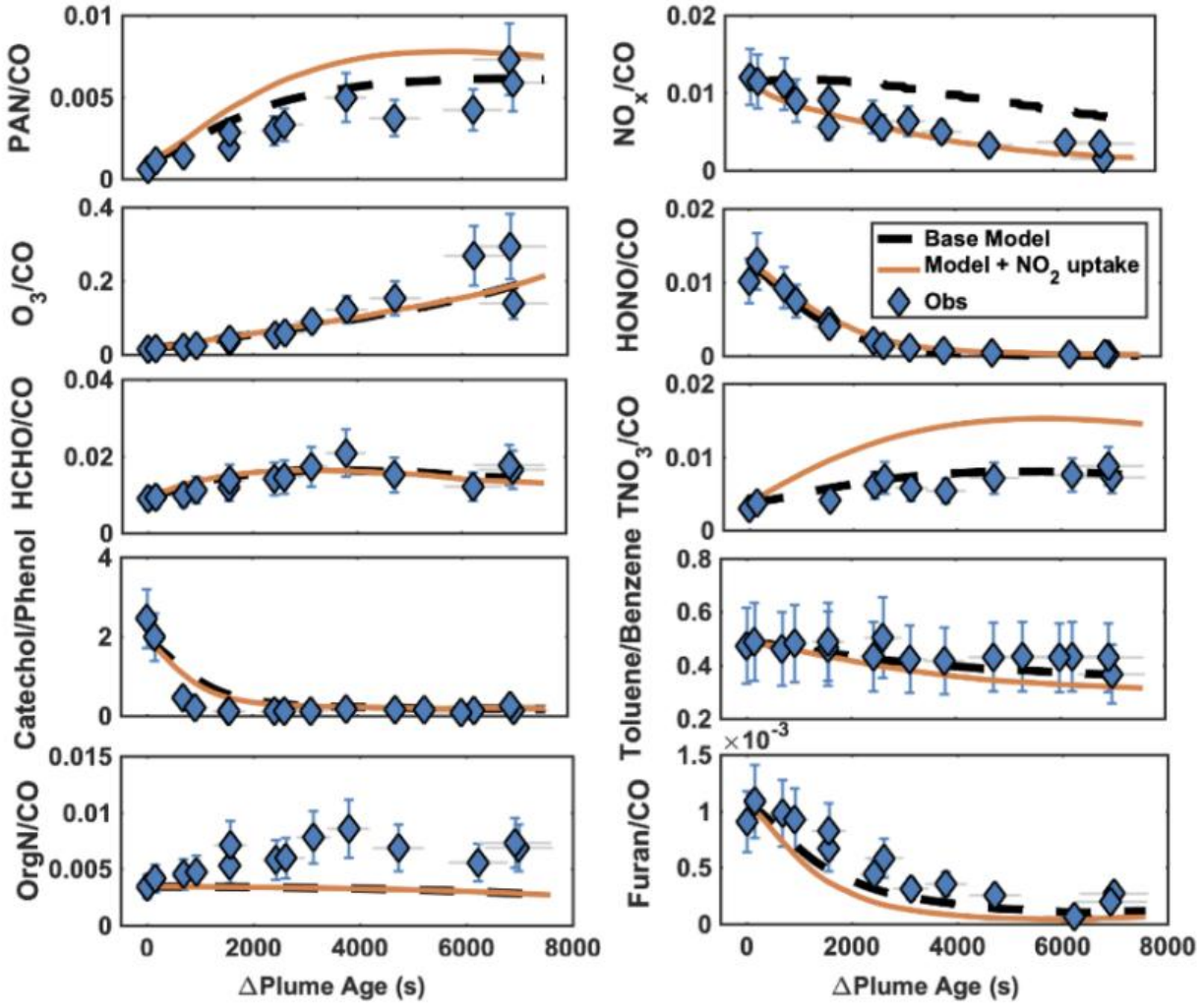

Figure S3.6. Comparison of CO-normalized mixing ratios (ppbv/ppbv) from base model simulation (dashed black curve) and nudged model with heterogeneous uptake of NO_2 (orange curve). Blue diamonds denote field observations of plume transect mixing ratios for Taylor Creek Fire.

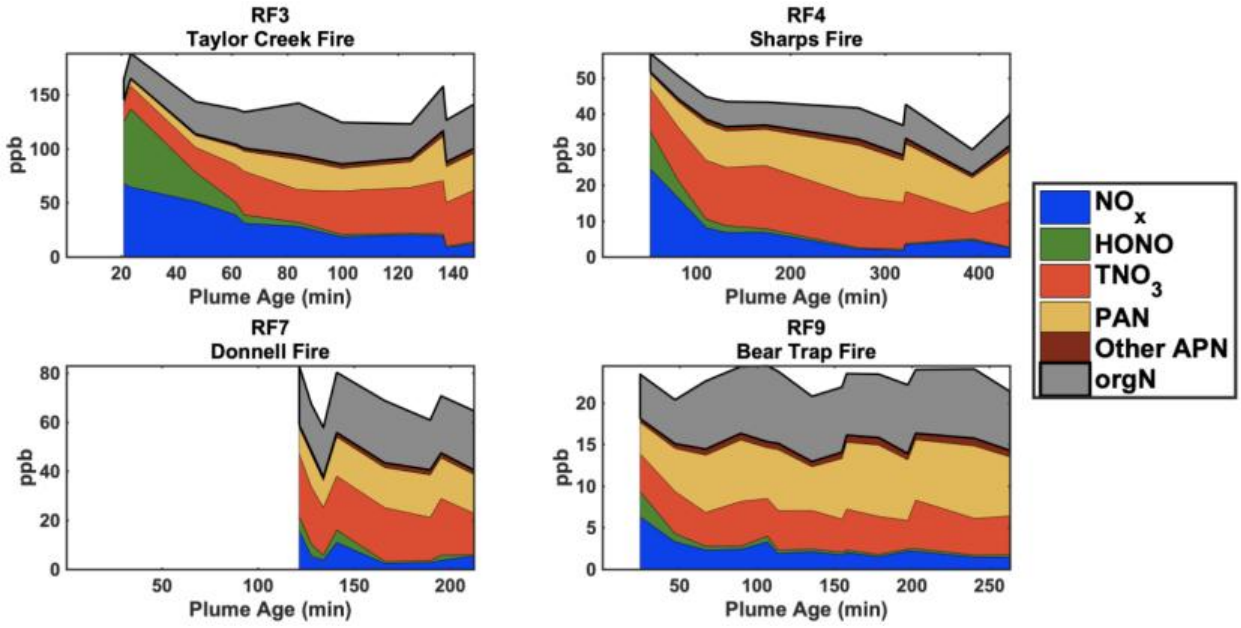

Figure S3.7. Evolution of dilution-corrected observed NO_y partitioning for the four fires.

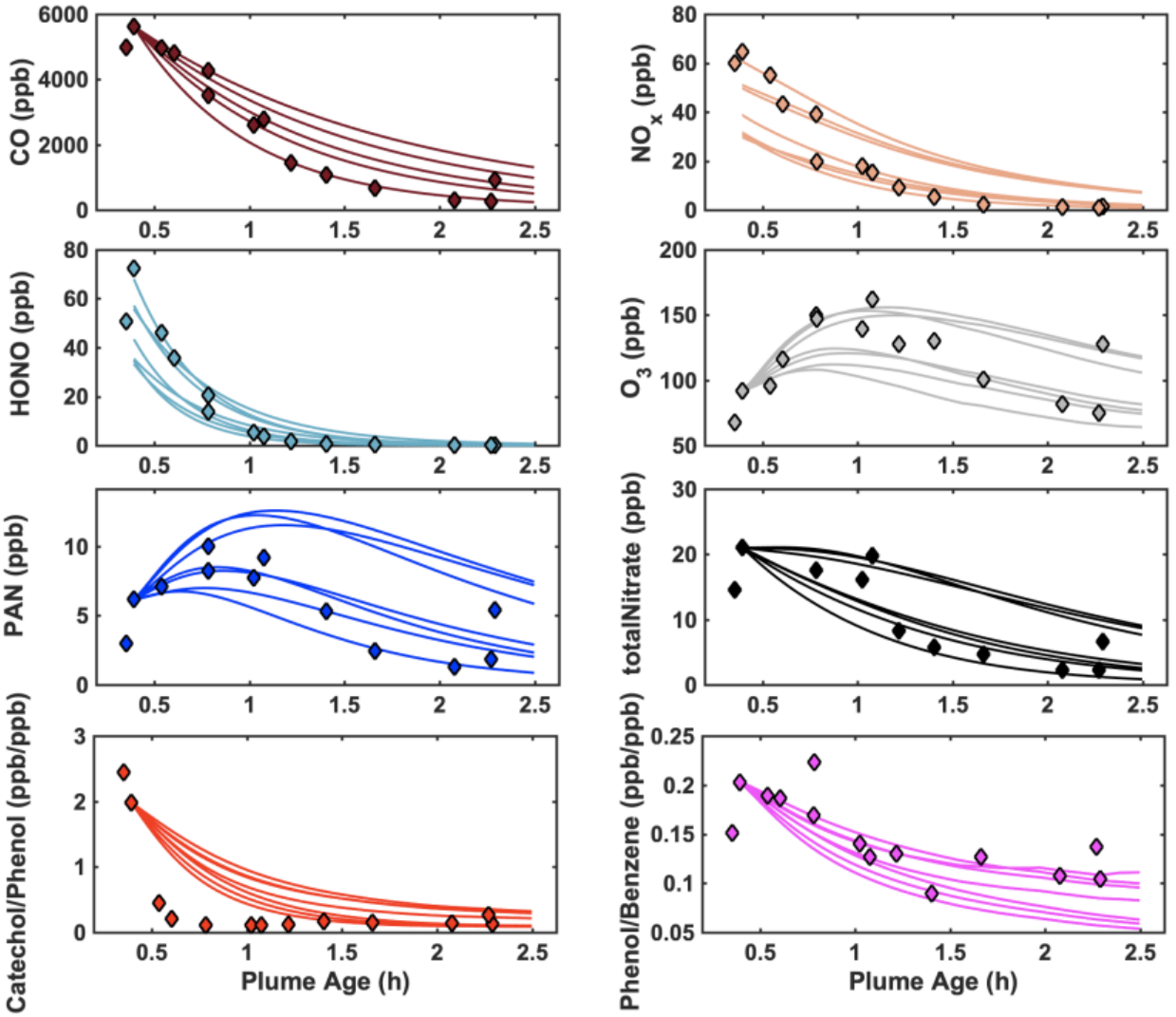

Figure S3.8. Back-extrapolating observations to the freshest pass for different species (encoded with different colors) from the next seven youngest plume intercepts in Taylor Creek Fire.

3.8. REFERENCES

Akagi, S. K., Yokelson, R. J., Wiedinmyer, C., Alvarado, M. J., Reid, J. S., Karl, T., et al. (2011). Atmospheric Chemistry and Physics Emission factors for open and domestic biomass burning for use in atmospheric models. *Atmos. Chem. Phys*, *11*, 4039–4072. https://doi.org/10.5194/acp-11-4039-2011

Akagi, S. K., Craven, J. S., Taylor, J. W., Mcmeeking, G. R., Yokelson, R. J., Burling, I. R., et al. (2012). Evolution of trace gases and particles emitted by a chaparral fire in California. *Atmos. Chem. Phys*, *12*, 1397–1421. https://doi.org/10.5194/acp-12-1397-2012

Akagi, S. K., Yokelson, R. J., Burling, I. R., Meinardi, S., Simpson, I., Blake, D. R., et al. (2013). Measurements of reactive trace gases and variable O 3 formation rates in some South Carolina biomass burning plumes. *Atmospheric Chemistry and Physics*, *13*(3), 1141–1165. https://doi.org/10.5194/acp-13-1141-2013

Alvarado, M. J., Logan, J. A., Mao, J., Apel, E., Riemer, D., Blake, D., et al. (2010). Nitrogen oxides and PAN in plumes from boreal fires during ARCTAS-B and their impact on ozone: an integrated analysis of aircraft and satellite observations. *Atmospheric Chemistry and Physics*, *10*(20), 9739–9760. https://doi.org/10.5194/acp-10-9739-2010

Alvarado, Matthew James, & Prinn, R. G. (2009). Formation of ozone and growth of aerosols in young smoke plumes from biomass burning: 1. Lagrangian parcel studies. *Journal of Geophysical Research*, *114*(D9), D09306. https://doi.org/10.1029/2008JD011144

Ammann, M., Rössler, E., Strekowskit, R., & George, C. (2005). Nitrogen dioxide multiphase chemistry: Uptake kinetics on aqueous solutions containing phenolic compounds. *Physical Chemistry Chemical Physics*, *7*(12), 2513–2518. https://doi.org/10.1039/b501808k

Andrews, S. J., Carpenter, L. J., Apel, E. C., Atlas, E., Donets, V., Hopkins, J. R., et al. (2016). A comparison of very short lived halocarbon (VSLS) and DMS aircraft measurements in the tropical west Pacific from CAST, ATTREX and CONTRAST. *Atmospheric Measurement Techniques*, *9*(10), 5213–5225. https://doi.org/10.5194/amt-9-5213-2016

Arnold, S. R., Emmons, L. K., Monks, S. A., Law, K. S., Ridley, D. A., Turquety, S., et al. (2015). Biomass burning influence on high-latitude tropospheric ozone and reactive nitrogen in summer 2008: a multi-model analysis based on POLMIP simulations. *Atmos. Chem. Phys*, *15*, 6047–6068. https://doi.org/10.5194/acp-15-6047-2015

Aschmann, S. M., Nishino, N., Arey, J., & Atkinson, R. (2011). Kinetics of the reactions of OH radicals with 2-and 3-methylfuran, 2,3-and 2,5-dimethylfuran, and e -and Z -3-hexene-2,5-dione, and products of OH + 2,5-dimethylfuran. *Environmental Science and Technology*, *45*(5), 1859–1865. https://doi.org/10.1021/es103207k

Aschmann, S. M., Nishino, N., Arey, J., & Atkinson, R. (2014). Products of the OH radical-initiated reactions of furan, 2- and 3-methylfuran, and 2,3- and 2,5-dimethylfuran in the presence of NO. *Journal of Physical Chemistry A*, *118*(2), 457–466. https://doi.org/10.1021/jp410345k

Ayres, B. R., Allen, H. M., Draper, D. C., Brown, S. S., Wild, R. J., Jimenez, J. L., et al. (2015). Organic nitrate aerosol formation via NO₃ + biogenic volatile organic compounds in the southeastern United States. *Atmospheric Chemistry and Physics*, *15*(23), 13377–13392. https://doi.org/10.5194/acp-15-13377-2015

Benedict, K. B., Zhou, Y., Sive, B. C., Prenni, A. J., Gebhart, K. A., Fischer, E. V., et al. (2019). Volatile organic compounds and ozone in Rocky Mountain National Park during FRAPPÉ. *Atmospheric Chemistry and Physics*, *19*(1), 499–521. https://doi.org/10.5194/acp-19-499-

2019

Browne, E. C., Min, K.-E., Wooldridge, P. J., Apel, E., Blake, D. R., Brune, W. H., et al. (2013). Observations of total RONO2 over the boreal forest: NOx sinks and HNO3 sources. *Atmospheric Chemistry and Physics*, *13*(9), 4543–4562. https://doi.org/10.5194/acp-13-4543-2013

Castellanos, P., Boersma, K. F., & Van Der Werf, G. R. (2014). Satellite observations indicate substantial spatiotemporal variability in biomass burning NOx emission factors for South America. *Atmospheric Chemistry and Physics*, *14*(8), 3929–3943. https://doi.org/10.5194/acp-14-3929-2014

Cheng, Z., Atwi, K. M., Yu, Z., Avery, A., Fortner, E. C., Williams, L., et al. (2020). Evolution of the light-absorption properties of combustion brown carbon aerosols following reaction with nitrate radicals. *Aerosol Science and Technology*, *54*(7), 849–863. https://doi.org/10.1080/02786826.2020.1726867

Coggon, M. M., Lim, C. Y., Koss, A. R., Sekimoto, K., Yuan, B., Gilman, J. B., et al. (2019). OH chemistry of non-methane organic gases (NMOGs) emitted from laboratory and ambient biomass burning smoke: evaluating the influence of furans and oxygenated aromatics on ozone and secondary NMOG formation. *Atmospheric Chemistry and Physics*, *19*(23), 14875–14899. https://doi.org/10.5194/acp-19-14875-2019

DeCarlo, P. F., Kimmel, J. R., Trimborn, A., Northway, M. J., Jayne, J. T., Aiken, A. C., et al. (2006). Field-deployable, high-resolution, time-of-flight aerosol mass spectrometer. *Analytical Chemistry*, *78*(24), 8281–8289. https://doi.org/10.1021/ac061249n

Decker, Z. C. J., Zarzana, K. J., Coggon, M., Min, K. E., Pollack, I., Ryerson, T. B., et al. (2019). Nighttime Chemical Transformation in Biomass Burning Plumes: A Box Model Analysis Initialized with Aircraft Observations. *Environmental Science and Technology*, *53*(5), 2529–2538. https://doi.org/10.1021/acs.est.8b05359

Ditto, J. C., He, M., Hass-Mitchell, T. N., Moussa, S. G., Hayden, K., Li, S. M., et al. (2021). Atmospheric evolution of emissions from a boreal forest fire: The formation of highly functionalized oxygen-, nitrogen-, and sulfur-containing organic compounds. *Atmospheric Chemistry and Physics*, *21*(1), 255–267. https://doi.org/10.5194/acp-21-255-2021

Elshorbany, Y. F., Kurtenbach, R., Wiesen, P., Lissi, E., Rubio, M., Villena, G., et al. (2009). Oxidation capacity of the city air of Santiago, Chile. *Atmospheric Chemistry and Physics*, *9*(6), 2257–2273. https://doi.org/10.5194/acp-9-2257-2009

Evtyugina, M., Calvo, A. I., Nunes, T., Alves, C., Fernandes, A. P., Tarelho, L., et al. (2013). VOC emissions of smouldering combustion from Mediterranean wildfires in central Portugal. *Atmospheric Environment*, *64*, 339–348. https://doi.org/10.1016/j.atmosenv.2012.10.001

Farmer, D. K., Matsunaga, A., Docherty, K. S., Surratt, J. D., Seinfeld, J. H., Ziemann, P. J., & Jimenez, J. L. (2010). Response of an aerosol mass spectrometer to organonitrates and organosulfates and implications for atmospheric chemistry. *Proceedings of the National Academy of Sciences of the United States of America*, *107*(15), 6670–6675. https://doi.org/10.1073/pnas.0912340107

Garcia-Hurtado, E., Pey, J., Borrás, E., Sánchez, P., Vera, T., Carratalá, A., et al. (2014). Atmospheric PM and volatile organic compounds released from Mediterranean shrubland wildfires. *Atmospheric Environment*, *89*, 85–92. https://doi.org/10.1016/j.atmosenv.2014.02.016

Garofalo, L. A., Pothier, M. A., Levin, E. J. T., Campos, T., Kreidenweis, S. M., & Farmer, D.

K. (2019). Emission and Evolution of Submicron Organic Aerosol in Smoke from Wildfires in the Western United States. *ACS Earth and Space Chemistry*, *3*(7), 1237–1247. https://doi.org/10.1021/acsearthspacechem.9b00125

Goldberger, L. A., Jahl, L. G., Thornton, J. A., & Sullivan, R. C. (2019). N2O5 reactive uptake kinetics and chlorine activation on authentic biomass-burning aerosol. *Environmental Science: Processes and Impacts*, *21*(10), 1684–1698. https://doi.org/10.1039/c9em00330d

Griffin, R. J., Chen, J., Carmody, K., Vutukuru, S., & Dabdub, D. (2007). Contribution of gas phase oxidation of volatile organic compounds to atmospheric carbon monoxide levels in two areas of the United States. *Article in Journal of Geophysical Research Atmospheres*. https://doi.org/10.1029/2006JD007602

Hatch, L. E., Rivas-Ubach, A., Jen, C. N., Lipton, M., Goldstein, A. H., & Barsanti, K. C. (2018). Measurements of I/SVOCs in biomass-burning smoke using solid-phase extraction disks and two-dimensional gas chromatography. *Atmospheric Chemistry and Physics*, *18*(24), 17801–17817. https://doi.org/10.5194/acp-18-17801-2018

He, H., Liang, X.-Z., Sun, C., Tao, Z., & Tong, D. Q. (2020). The long-term trend and production sensitivity change in the US ozone pollution from observations and model simulations. *Atmospheric Chemistry and Physics*, *20*(5), 3191–3208. https://doi.org/10.5194/acp-20-3191-2020

Hodgson, A. K., Morgan, W. T., O'shea, S., Bauguitte, S., Allan, J. D., Darbyshire, E., et al. (2018). Near-field emission profiling of tropical forest and Cerrado fires in Brazil during SAMBBA 2012. *Atmos. Chem. Phys*, *18*, 5619–5638. https://doi.org/10.5194/acp-18-5619-2018

Hodshire, A. L., Akherati, A., Alvarado, M. J., Brown-Steiner, B., Jathar, S. H., Jimenez, J. L., et al. (2019, April 29). Aging Effects on Biomass Burning Aerosol Mass and Composition: A Critical Review of Field and Laboratory Studies. *Environmental Science and Technology*. American Chemical Society. https://doi.org/10.1021/acs.est.9b02588

Jacob, D. J., Wofsy, S. C., Bakwin, P. S., Fan, S.-M., Harriss, R. C., Talbot, R. W., et al. (1992). Summertime photochemistry of the troposphere at high northern latitudes. *Journal of Geophysical Research*, *97*(D15), 16421. https://doi.org/10.1029/91JD01968

Jacob, Daniel J. (2000). Heterogeneous chemistry and tropospheric ozone. *Atmospheric Environment*, *34*(12–14), 2131–2159. https://doi.org/10.1016/S1352-2310(99)00462-8

Jaffe, D. A., & Wigder, N. L. (2012, May 1). Ozone production from wildfires: A critical review. *Atmospheric Environment*. Pergamon. https://doi.org/10.1016/j.atmosenv.2011.11.063

Jenkin, M. E., Young, J. C., & Rickard, A. R. (2015). The MCM v3.3.1 degradation scheme for isoprene. *Atmospheric Chemistry and Physics*, *15*(20), 11433–11459. https://doi.org/10.5194/acp-15-11433-2015

Jolleys, M. D., Coe, H., McFiggans, G., Taylor, J. W., O'Shea, S. J., Le Breton, M., et al. (2015). Properties and evolution of biomass burning organic aerosol from Canadian boreal forest fires. *Atmospheric Chemistry and Physics*, *15*(6), 3077–3095. https://doi.org/10.5194/acp-15-3077-2015

Joo, T., Rivera-Rios, J. C., Takeuchi, M., Alvarado, M. J., & Ng, N. L. (2019). Secondary Organic Aerosol Formation from Reaction of 3-Methylfuran with Nitrate Radicals. *ACS Earth and Space Chemistry*, *3*(6), 922–934. https://doi.org/10.1021/acsearthspacechem.9b00068

Juncosa Calahorrano, J. F., Lindaas, J., O'Dell, K., Palm, B. B., Peng, Q., Flocke, F., et al. (2020). Daytime Oxidized Reactive Nitrogen Partitioning in Western U.S. Wildfire Smoke

Plumes. *Journal of Geophysical Research: Atmospheres*, e2020JD033484. https://doi.org/10.1029/2020JD033484

Kondo, Y., Matsui, H., Moteki, N., Sahu, L., Takegawa, N., Kajino, M., et al. (2011). Emissions of black carbon, organic, and inorganic aerosols from biomass burning in North America and Asia in 2008. *Journal of Geophysical Research Atmospheres*, *116*(8). https://doi.org/10.1029/2010JD015152

Koss, A. R., Sekimoto, K., Gilman, J. B., Selimovic, V., Coggon, M. M., Zarzana, K. J., et al. (2018). Non-methane organic gas emissions from biomass burning: identification, quantification, and emission factors from PTR-ToF during the FIREX 2016 laboratory experiment. *Atmos. Chem. Phys*, *18*, 3299–3319. https://doi.org/10.5194/acp-18-3299-2018

Kwok, C. Y., Laurent, O., Guemri, A., Philippon, C., Wastine, B., Rella, C. W., et al. (2015). Comprehensive laboratory and field testing of cavity ring-down spectroscopy analyzers measuring H2O, CO2, CH4 and CO. *Atmos. Meas. Tech*, *8*, 3867–3892. https://doi.org/10.5194/amt-8-3867-2015

Lee, B. H., Lopez-Hilfiker, F. D., Mohr, C., Kurtén, T., Worsnop, D. R., & Thornton, J. A. (2014). An iodide-adduct high-resolution time-of-flight chemical-ionization mass spectrometer: Application to atmospheric inorganic and organic compounds. *Environmental Science and Technology*, *48*(11), 6309–6317. https://doi.org/10.1021/es500362a

Lee, B. H., Lopez-Hilfiker, F. D., Veres, P. R., McDuffie, E. E., Fibiger, D. L., Sparks, T. L., et al. (2018). Flight Deployment of a High-Resolution Time-of-Flight Chemical Ionization Mass Spectrometer: Observations of Reactive Halogen and Nitrogen Oxide Species. *Journal of Geophysical Research: Atmospheres*, *123*(14), 7670–7686. https://doi.org/10.1029/2017JD028082

Lelieveld, J., Gromov, S., Pozzer, A., & Taraborrelli, D. (2016). Global tropospheric hydroxyl distribution, budget and reactivity. *Atmos. Chem. Phys*, *16*, 12477–12493. https://doi.org/10.5194/acp-16-12477-2016

Lindaas, J., Pollack, I. B., Garofalo, L. A., Pothier, M. A., Farmer, D. K., Kreidenweis, S. M., et al. (2021). Emissions of Reactive Nitrogen From Western U.S. Wildfires During Summer 2018. *Journal of Geophysical Research: Atmospheres*, *126*(2), e2020JD032657. https://doi.org/10.1029/2020JD032657

Liu, X., Zhang, Y., Huey, L. G., Yokelson, R. J., Wang, Y., Jimenez, J. L., et al. (2016). Agricultural fires in the southeastern U.S. during SEAC4RS: Emissions of trace gases and particles and evolution of ozone, reactive nitrogen, and organic aerosol. *Journal of Geophysical Research*, *121*(12), 7383–7414. https://doi.org/10.1002/2016JD025040

Lopez-Hilfiker, F. D., Iyer, S., Mohr, C., Lee, B. H., D'ambro, E. L., Kurtén, T., & Thornton, J. A. (2016). Constraining the sensitivity of iodide adduct chemical ionization mass spectrometry to multifunctional organic molecules using the collision limit and thermodynamic stability of iodide ion adducts. *Atmospheric Measurement Techniques*, *9*(4), 1505–1512. https://doi.org/10.5194/amt-9-1505-2016

McClure, C. D., & Jaffe, D. A. (2018). US particulate matter air quality improves except in wildfire-prone areas. *Proceedings of the National Academy of Sciences of the United States of America*, *115*(31), 7901–7906. https://doi.org/10.1073/pnas.1804353115

Mebust, A. K., Russell, A. R., Hudman, R. C., Valin, L. C., & Cohen, R. C. (2011). Characterization of wildfire NOx emissions using MODIS fire radiative power and OMI tropospheric NO2 columns. *Atmospheric Chemistry and Physics*, *11*(12), 5839–5851. https://doi.org/10.5194/acp-11-5839-2011

Palm, B. B., Liu, X., Jimenez, J. L., & Thornton, J. A. (2019). Performance of a new coaxial ion-molecule reaction region for low-pressure chemical ionization mass spectrometry with reduced instrument wall interactions. *Atmos. Meas. Tech*, *12*, 5829–5844. https://doi.org/10.5194/amt-12-5829-2019

Palm, B. B., Peng, Q., Fredrickson, C. D., Lee, B. H., Garofalo, L. A., Pothier, M. A., et al. (2020). Quantification of organic aerosol and brown carbon evolution in fresh wildfire plumes. *Proceedings of the National Academy of Sciences of the United States of America*, *117*(47), 29469–29477. https://doi.org/10.1073/pnas.2012218117

Parrington, M., Palmer, P. I., Lewis, A. C., Lee, J. D., Rickard, A. R., Carlo, P. Di, et al. (2013). Sciences ess Atmospheric Chemistry and Physics Climate of the Past Geoscientific Instrumentation Methods and Data Systems Ozone photochemistry in boreal biomass burning plumes. *Atmos. Chem. Phys*, *13*, 7321–7341. https://doi.org/10.5194/acp-13-7321-2013

Peng, Q., Palm, B. B., Melander, K. E., Lee, B. H., Hall, S. R., Ullmann, K., et al. (2020). HONO Emissions from Western U.S. Wildfires Provide Dominant Radical Source in Fresh Wildfire Smoke. *Environmental Science and Technology*, *54*(10), 5954–5963. https://doi.org/10.1021/acs.est.0c00126

Permar, W., Wang, Q., Selimovic, V., Wielgasz, C., Yokelson, R. J., Hornbrook, R. S., et al. (2021). Emissions of Trace Organic Gases From Western U.S. Wildfires Based on WE-CAN Aircraft Measurements. *Journal of Geophysical Research: Atmospheres*, *126*(11). https://doi.org/10.1029/2020JD033838

Real, E., Law, K. S., Weinzierl, B., Fiebig, M., Petzold, A., Wild, O., et al. (2007). Processes influencing ozone levels in Alaskan forest fire plumes during long-range transport over the North Atlantic. *Journal of Geophysical Research: Atmospheres*, *112*(D10). https://doi.org/10.1029/2006JD007576

Ridley, B. A., & Grahek, F. E. (1990). A Small, Low Flow, High Sensitivity Reaction Vessel for NO Chemiluminescence Detectors. *Journal of Atmospheric and Oceanic Technology*, *7*(2), 307–311. https://doi.org/10.1175/1520-0426(1990)007<0307:aslfhs>2.0.co;2

Ridley, B. A., Grahek, F. E., & Walega, J. G. (1992). A small, high-sensitivity, medium-response ozone detector suitable for measurements from light aircraft. *Journal of Atmospheric & Oceanic Technology*, *9*(2), 142–148. https://doi.org/10.1175/1520-0426(1992)009<0142:ASHSMR>2.0.CO;2

Roberts, J. M., Stockwell, C. E., Yokelson, R. J., De Gouw, J., Liu, Y., Selimovic, V., et al. (2020). The nitrogen budget of laboratory-simulated western US wildfires during the FIREX 2016 Fire Lab study. *Atmospheric Chemistry and Physics*, *20*(14), 8807–8826. https://doi.org/10.5194/acp-20-8807-2020

Romer, P. S., Duffey, K. C., Wooldridge, P. J., Edgerton, E., Baumann, K., Feiner, P. A., et al. (2018). Effects of temperature-dependent NOx emissions on continental ozone production. *Atmospheric Chemistry and Physics*, *18*(4), 2601–2614. https://doi.org/10.5194/acp-18-2601-2018

Ryder, O. S., Campbell, N. R., Shaloski, M., Al-Mashat, H., Nathanson, G. M., & Bertram, T. H. (2015). Role of Organics in Regulating ClNO2 Production at the Air-Sea Interface. *Journal of Physical Chemistry A*, *119*(31), 8519–8526. https://doi.org/10.1021/jp5129673

Schroeder, J. R., Crawford, J. H., Fried, A., Walega, J., Weinheimer, A., Wisthaler, A., et al. (2017). New insights into the column CH_2O/NO_2 ratio as an indicator of near-surface ozone sensitivity. *Journal of Geophysical Research: Atmospheres*, *122*(16), 8885–8907.

https://doi.org/10.1002/2017JD026781
Sekimoto, K., Koss, A. R., Gilman, J. B., Selimovic, V., Coggon, M. M., Zarzana, K. J., et al. (2018). High-and low-temperature pyrolysis profiles describe volatile organic compound emissions from western US wildfire fuels. *Atmos. Chem. Phys*, *18*, 9263–9281. https://doi.org/10.5194/acp-18-9263-2018
Shetter, R. E., & Müller, M. (1999). Photolysis frequency measurements using actinic flux spectroradiometry during the PEM-Tropics mission: Instrumentation description and some results. *Journal of Geophysical Research: Atmospheres*, *104*(D5), 5647–5661. https://doi.org/10.1029/98JD01381
Slusher, D. L. (2004). A thermal dissociation–chemical ionization mass spectrometry (TD-CIMS) technique for the simultaneous measurement of peroxyacyl nitrates and dinitrogen pentoxide. *Journal of Geophysical Research*, *109*(D19), D19315. https://doi.org/10.1029/2004JD004670
Stemmler, K., Ndour, M., Elshorbany, Y., Kleffmann, J., D'Anna, B., George, C., et al. (2007). Light induced conversion of nitrogen dioxide into nitrous acid on submicron humic acid aerosol. *Atmospheric Chemistry and Physics*, *7*(16), 4237–4248. https://doi.org/10.5194/acp-7-4237-2007
Tanimoto, H., Ikeda, K., Folkert Boersma, K., Van Der A., R. J., & Garivait, S. (2015). Interannual variability of nitrogen oxides emissions from boreal fires in Siberia and Alaska during 1996-2011 as observed from space. *Environmental Research Letters*, *10*(6), 065004. https://doi.org/10.1088/1748-9326/10/6/065004
Thornton, J. A., Kercher, J. P., Riedel, T. P., Wagner, N. L., Cozic, J., Holloway, J. S., et al. (2010). A large atomic chlorine source inferred from mid-continental reactive nitrogen chemistry. *Nature*, *464*(7286), 271–274. https://doi.org/10.1038/nature08905
Urbanski, S. (2014). Wildland fire emissions, carbon, and climate: Emission factors. *Forest Ecology and Management*, *317*, 51–60. https://doi.org/10.1016/j.foreco.2013.05.045
Wolfe, G. M., Marvin, M. R., Roberts, S. J., Travis, K. R., & Liao, J. (2016). The framework for 0-D atmospheric modeling (F0AM) v3.1. *Geoscientific Model Development*, *9*(9), 3309–3319. https://doi.org/10.5194/gmd-9-3309-2016
Yabushita, A., Enami, S., Sakamoto, Y., Kawasaki, M., Hoffmann, M. R., & Colussi, A. J. (2009). Anion-catalyzed dissolution of NO2 on aqueous microdroplets. *Journal of Physical Chemistry A*, *113*(17), 4844–4848. https://doi.org/10.1021/jp900685f
Zheng, W., Flocke, F. M., Tyndall, G. S., Swanson, A., Orlando, J. J., Roberts, J. M., et al. (2011). Characterization of a thermal decomposition chemical ionization mass spectrometer for the measurement of peroxy acyl nitrates (PANs) in the atmosphere. *Atmospheric Chemistry and Physics*, *11*(13), 6529–6547. https://doi.org/10.5194/acp-11-6529-2011

CHAPTER 4. DIRECT CONSTRAINTS ON SECONDARY HONO PRODUCTION IN AGED WILDFIRE SMOKE FROM AIRBORNE MEASUREMENTS IN WESTERN US

4.1 INTRODUCTION

Nitrous acid (HONO) is an important precursor of the tropospheric hydroxyl radical (OH), which controls the self-cleansing capacity of the atmosphere and accelerates the formation of secondary pollutants. Wildfires are a major source of HONO, and the known sources of HONO in fire plumes include direct emissions and homogeneous reaction between NO and OH. In addition, numerous secondary HONO formation pathways have been suggested in various environments (Bao et al., 2018; Z. Liu et al., 2014; K. Stemmler et al., 2007; Ye et al., 2016; Zhou et al., 2001). Recently, we've shown that for wildfires, HONO primary emissions either dominate over secondary sources or cannot easily be separated from fast secondary formation close to the fires (Peng et al., 2020). However, as smoke travels further downwind, daytime photolytic loss of directly emitted HONO ($\tau \sim 0.3$ hr) leads to secondary HONO formation becoming relatively more important to the resupply of HONO in smoke plumes. A consensus on the importance of secondary HONO sources has not yet been achieved, and the dominant mechanisms of HONO formation are still widely discussed. Several field studies outside of wildfire plumes have shown much higher daytime HONO levels than expected from known reactions, implying large unidentified HONO sources to reconcile such observations (Sörgel et al., 2011; Ye et al., 2018). On the contrary, some studies found that well known pathways could explain the observed HONO levels without the need to invoke additional mechanisms (Neuman et al., 2016), and some researchers suggested that the additional HONO sources may not be real but rather stem from disturbances in photo-stationary

states or instrument artifacts (B. H. Lee et al., 2013; R. Crilley et al., 2016; Veres et al., 2015).

Finlayson-Pitts et al. (2003) proposed a mechanism by which NO_2 heterogeneous chemistry can produce HONO in the absence of light via formation of the NO_2 dimer (N_2O_4) and its reaction on surfaces. However, Gustafsson et al. (2008) suggested that this mechanism is unlikely in typical atmospheric conditions, and proposed a process where NO_2 reacts directly on the active surface to form HONO. Heterogeneous reactions of NO_2 on surfaces are considered a potentially ubiquitous source of HONO, but with an uncertain magnitude especially for aerosol particle surfaces, with measured reactive uptake coefficients (γ) spanning 4 orders of magnitude from 10^{-7} to 10^{-3} and often dependent on relative humidity (Acker et al., 2004; Ammann et al., 1998; Han et al., 2016; Kleffmann et al., 1999; Liu et al., 2014; Monge et al., 2010; Stemmler et al., 2007). Photo-enhanced NO_2 heterogeneous chemistry via NO_2 hydrolytic disproportionation has also been reported as an important HONO source (George et al., 2005). Colussi et al. (2013) found that photochemically formed dicarboxylic acid anions may catalyze the conversion from NO_2 to HONO on aqueous aerosol surfaces with γ on the order of 10^{-4} to 10^{-3}, and Liu et al. (2014) supported this hypothesis using extensive correlation analysis to account for enhanced HONO formation in Beijing. Wang et al. (2021) used a large-eddy simulation model to assess the interplay between turbulent mixing and HONO chemistry for conditions typical of the Southeast United States and found a good model-observation agreement in HONO using a γ range of 10^{-4}-10^{-3}. Moreover, photosensitized heterogeneous reduction of NO_2 on organic substrates or soot particles has been observed as a major HONO source in many studies (Aubin & Abbatt, 2007; George et al., 2005; Han et al., 2016; Monge et al., 2010; Stemmler et al., 2006), especially in plumes with high NO_2 concentrations (Kleffmann et al., 1999).

Other studies have suggested that particulate nitrate (pNO_3) can be photolyzed to produce

HONO with the production rate described by scaling the HNO_3(g) photolysis frequency (j_{HNO3}) by an enhancement factor (Bao et al., 2018; Ye et al., 2016; Zhou et al., 2001, 2002, 2003). However, there are large discrepancies in estimates of this enhancement factor depending on the nitrate loading and aerosol organic composition, leading to drastically different conclusions as to the importance of this source (Romer et al., 2018; Ye et al., 2016, 2017). Haskins et al. (2019) reported that using an enhancement factor of 300 recommended in Ye et al. (2016) overestimated measured HONO in aged wintertime urban plumes, consistent with the moderate enhancement factors (1−30) reported in Romer et al. (2018) derived from analysis of HNO_3/NO_x ratios. Shi et al. (2021) found the enhancement factor to be an order of magnitude lower than Ye et al. (2016) in laboratory experiments using suspended submicron particles.

In addition to the potential for multiphase sources of HONO, novel homogeneous HONO sources have also been proposed in recent years. A gas-phase reaction between electronically excited NO_2 (NO_2*) and H_2O has been proposed as a source of HONO and OH (S. Li et al., 2008), but was shown to be irrelevant in the ambient atmosphere (Amedro et al., 2011; Carr et al., 2009; Czader et al., 2012; Sörgel et al., 2011; Wong et al., 2012). Li et al. (2014) observed high HONO levels in the sunlit residual layer, i.e. decoupled from the ground surface, and postulated the reaction between hydroperoxyl–water complex ($HO_2 \cdot H_2O$) and NO_2 produced HONO at 100% yield, but Ye et al. (2015) contended that the yield of this reaction was < 3%. This particular reaction is different from most HONO sources in that it is not a net source of HO_x and instead alters the OH/HO_2 ratio. If most HONO arose from such a pathway its importance on oxidizing capacity would therefore be much less.

The relative importance of different secondary HONO sources in different environments is thus not well constrained. Previous field observations show that pNO_3 photolysis is the main

contributor to secondary HONO production in low-NO_x conditions such as in remote background air and forest canopy (Ye et al., 2016; Zhou et al., 2011). However, a recent isotopic analysis suggests that nitrate photolysis plays a minor role (<5%) while photo-enhanced NO_2-to-HONO heterogeneous conversion contributes 85-95% to total HONO production for the aged daytime fire plume measured at the surface (Chai et al., 2021).

Few studies have used ambient HONO measurements aloft of the surface to better isolate the role of aerosol chemistry from that occurring on ground surface elements. Wildfire plumes often are injected aloft of the well-mixed planetary boundary layer, providing an opportunity to probe the homogeneous and aerosol particle processes more directly without efficient contact with the ground surface. Herein, we use *in situ* measurements made aboard the NCAR/NSF C-130 aircraft during the Western Wildfire Experiment for Cloud chemistry, Aerosol absorption and Nitrogen (WE-CAN) campaign, which was carried out in summer 2018 in the western U.S., to examine the possible unknown sources of HONO in aged smoke plumes aloft of the surface. We evaluate the upper-limit magnitudes of heterogeneous (NO_2-driven) and surface photolysis (pNO_3-driven) sources, and assess the range of key parameters required to reproduce the observed HONO levels. We also applied a multinomial linear regression to determine the contributions of these pathways in authentic fire smoke which were previously only studied in the laboratory or tested in the model with considerable speculation. We conclude with a box model simulation to show the contributions of governing secondary sources as the fire plume ages.

4.2 METHODS

The WE-CAN campaign took place from 22 July to 14 September 2018. The research aircraft was based in Boise, ID from 24 July to 31 August 2018, and this period is the focus of our paper. High time resolution in situ measurements were conducted aboard the NCAR/NSF C-130

aircraft, including various trace gases (such as HONO, NO_x, pNO_3, HNO_3, etc), photolysis frequencies, aerosol surface area density for submicron particles, meteorological parameters (such as pressure, temperature, relative humidity, wind speed and direction). The details of campaign and flight descriptions can be found elsewhere (Juncosa Calahorrano et al., 2020; Lindaas et al., 2021; Palm et al., 2020; Peng et al., 2020).

Measurements of HONO were made by the University of Washington Iodide adduct Chemical Ionization Mass Spectrometer (UW I-CIMS). Details for the instrument operation during WE-CAN and relevant calibration tests are described previously (Palm et al., 2020; Peng et al., 2020). For this analysis, we tested NO_2-to-HONO conversion in the instrument tubing by injecting NO_2 through the inlet used during WE-CAN, and measuring HONO as a function of the NO_2 mixing ratio sampled by the inlet. A small flow (1 to 10 sccm) of NO_2 from a dilute calibrated cylinder (Praxair) was passed over a calcium carbonate denuder just prior to mixing with the 20 slpm inlet flow to remove HONO produced from the cylinder, regulator, flow controller, and delivery tubing surfaces. The NO_2 conversion to HONO in the inlet/IMR under WE-CAN conditions is found to be less than 0.3% (Figure S4.1). Thus, inlet NO_2-to-HONO artefacts are negligible for the WE-CAN conditions we evaluate.

Other observations made aboard the C-130 aircraft during WE-CAN used in our analysis include NO and NO_2 mixing ratios from the NCAR chemiluminescence instrument (Ridley & Grahek, 1990), submicron pNO_3 mass concentrations from the aerosol mass spectrometer (AMS) (Garofalo et al., 2019), photolysis frequencies from upward and downward spectral radiometers (Shetter & Müller, 1999), dry aerosol size distributions from the UHSAS instrument (Brock et al., 2019), and additional tracers from the UW I-CIMS as detailed below.

A simple zero-dimensional box model was applied to evaluate the relative importance of

different secondary sources. Detailed descriptions for baseline model setup have been published elsewhere (Peng et al., 2021).

4.3 Results and Discussion

4.3.1 Observations of HONO Enhancement in the Far-field

Due to its short photolytic lifetime of 15-20 min in aged fire plumes (Peng et al., 2020), HONO is expected to reach photo-stationary steady state in the far-field, e.g. a few hours downwind of fire emissions during the daytime. In such aged smoke, we expect direct HONO emissions play a minor role and that secondary processes dominate the HONO source. To probe the existence of secondary HONO formation, we specifically examined wildfire smoke sampled with a physical age over 3 h during WE-CAN. Research Flight (RF) 5 provides an ideal case study given the interception of smoke spreading over the western U.S. from California wildfires, with a slight influence from emissions of the Mendocino Complex fire. In this "River of Smoke" flight, we estimate physical plume ages of at least 400 min, suggesting the smoke is significantly aged during the measurement period. In addition, the measurements were conducted in the free troposphere, which excludes complexities from ground surface interactions.

Figure 4.1a shows the satellite imagery of the wildfire smoke with RF5 flight tracks color coded by 1-min average HONO mixing ratios. Active fire fronts detected by the Visible Infrared Imaging Radiometer Suite (VIIRS) thermal band are outlined in red. We observed that HONO concentrations are consistently enhanced in a portion of smoke intercepted in Nevada originating from fires in California. The peak HONO measured reached above 190 ppt, well above the 3σ 1-min detection limit of ~14 ppt (Figure 4.1b). Given a significant photolytic loss rate, these HONO levels suggest an important secondary source of HONO well downwind of the emission location.

The photo-stationary steady state (PSS) method based on concentrations of HONO, OH

and NO_x has been widely used to infer missing HONO sources (Kleffmann et al., 2005). Here, we calculated the PSS HONO for RF 5 based on reactions 4.1-4.3, where OH concentrations were estimated by scaling the ozone photolysis rates (Tan et al., 2019). HONO photolytic loss exceeds the homogeneous formation by more than 5 times in the river of smoke. Even at a peak OH concentration of 1×10^7 molec cm^{-3}, the reaction is still too slow to compete with the loss by photolysis, revealing the presence of an *in situ* HONO source dispersed in the atmosphere. Potential HONO source mechanisms (reactions 4.4a–4.4e) are discussed below.

$$OH + NO + M \rightarrow HONO + M \quad (4.1)$$

$$HONO + h\nu \rightarrow OH + NO \quad (4.2)$$

$$HONO + OH \rightarrow H_2O + NO_2 \quad (4.3)$$

$$[\text{Other sources}] \rightarrow HONO \quad (4.4)$$

$$p\text{NO}_3 + h\nu \rightarrow 0.67\text{HONO} + 0.33\text{NO}_2 \quad (4.4a)$$

$$2NO_2 + H_2O\ (\text{surface}) + h\nu \rightarrow HONO + HNO_3 \quad (4.4b)$$

$$NO_2 + \{R - H\}_{red}\ (\text{surface}) \rightarrow HONO + \{R\}_{ox} \quad (4.4c)$$

$$NO_2^* + H_2O \rightarrow HONO + OH \quad (4.4d)$$

$$HO_2\cdot H_2O + NO_2 \rightarrow \alpha\text{HONO} + O_2 + H_2O \quad (4.4e)$$

We estimate the magnitude of missing daytime HONO source (Eq. 4.1) from the difference between the measured HONO loss rate (R4.2, R4.3) and homogeneous production rate (R4.1), which are by far the largest terms in the HONO budget comprised of R4.1-R4.4. In cases of high spatial heterogeneity, this calculation may be inaccurate as local PSS may be perturbed as a result of changes in the composition of the VOC and NO_x emissions in wildfire plumes (Crilley et al.,

2016). Other sources of variability include changes in meteorological conditions as well as measurement noise. Given the short lifetime of HONO in a sunlit plume more than a few hours old and disconnected from surface deposition, we assume such changes in plume composition and meteorological conditions are minor perturbations to the plume steady state. Thus, for this field of old smoke, we assume the air mass was homogeneous during the sampling period, and HONO was in steady state.

$$P(HONO)_{other} = j_{HONO}[HONO] + k_{HONO+OH}[HONO][OH] - k_{NO+OH}[NO][OH] \quad \text{(Eq. 4.1)}$$

We performed a correlation analysis of this inferred HONO source (P_{other}) to multiple candidate mechanisms identified in the literature (Figure S4.2) (J. D. Lee et al., 2016; Lu et al., 2018; Su et al., 2008). We found good correlations of the inferred missing source with particulate nitrate photolysis and both dark and photo-enhanced NO_2 heterogeneous uptake. We show the HONO budget time series for the River of Smoke (Figure S4.3) comparing the upper bounds of turnover rates for different NO_x-related pathways (reactions 4b-4e), where a maximum HONO yield of 3% was used for reaction 4e (Ye et al., 2015), and a maximum uptake coefficient of 10^{-4} was adopted for reaction 4c (Monge et al., 2010; Ndour et al., 2008). These NO_x-related pathways account for less than half of HONO production rates in the fire plume in RF 5 even though the upper limit rate parameters from past studies are applied.

To balance the rapid photolytic loss, we examined two plausible secondary sources based on the correlation analysis: (1) $p$$NO_3$ photolysis; (2) (dark and photo-enhanced) NO_2 heterogeneous hydrolysis (i.e., NO_2-driven pathway). The correlation of an inferred HONO source from $HO_2H_2O + NO_2$ is weak ($R^2 = 0.24$, Figure S4.3) and thus this pathway is not considered. We multiplied the measured photolysis frequency of gas phase nitric acid (j_{HNO3}) by an enhanced factor of 300 (Ye et al., 2016) as the baseline for HONO production from $p$$NO_3$ photolysis (P_{pNO3})

as shown in Eq. 4.2. Recent studies suggest $\gamma(NO_2)$ for HONO production on aerosol surfaces is in the range of 10^{-5} -10^{-3} for aerosol particle surfaces in sunlight (Colussi et al., 2013; Khalizov et al., 2010; Z. Liu et al., 2014; Wong et al., 2012), and we adopted a value of 10^{-4} for $\gamma(NO_2)$ as the baseline for HONO formation from NO_2 uptake (Eq. 4.3). The surface area (S_A) has been adjusted using a hygroscopic factor following Liu et al. (2008) to correct for aerosol hygroscopic growth.

$$P_{pNO3} = J(pNO_3) * [pNO_3] = 300*J(HNO_3)*[pNO_3] \quad \text{(Eq. 4.2)}$$

$$P_{NO2het} = K_{het} * [NO_2] = \gamma_{NO2\rightarrow HONO} * \omega * S_A/4*[NO_2] \quad \text{(Eq. 4.3)}$$

Figure 4.1c shows the 1 min average observed HONO mixing ratios in the River of Smoke flight, as well as the inferred HONO from baseline production of the two candidate mechanisms. The baseline pNO_3 photolysis source overestimates HONO levels by a factor of 3.2 on average, and a single scaling factor of j_{HNO3} would not be able to capture the measured HONO as the ratio of measured to predicted HONO changes across the plume samples. For example, HONO predicted by pNO_3 photolysis is more than a factor of 5 larger than that observed at 20:13 UTC, while just over a factor of 2 higher than observed at 20:28 UTC. The NO_2 heterogeneous uptake alone significantly underestimates HONO concentrations in the plumes using $\gamma(NO_2) = 10^{-4}$. The aerosol surface area used in these calculations may be a lower limit as only submicron aerosols were measured and assessed. If NO_2 heterogeneous conversion to HONO occurs across the entire size distribution, our $\gamma(NO_2)$ would be smaller for the same HONO production rate. However, for this pathway alone to explain the observed HONO, the $\gamma(NO_2)$ would need to be more than an order of magnitude larger which is likely inconsistent with all prior laboratory studies and other field studies. As pNO_3 also likely exists in super-micron particles, the pNO_3 source is even larger than we calculate and thus incorporating their contribution would overestimate observed HONO to an even greater extent.

4.3.2 Evaluation of Possible Secondary HONO Sources

Variable secondary HONO production may stem from different chemical and physical conditions in the plume. Multiple production pathways could also co-exist with relative contributions varying with plume age and smoke conditions. For example, NO_2 heterogeneous uptake may be important in early stages, but as NO_x gets oxidized and diluted with time, the pNO_3 reservoir may become a larger contributor to HONO formation. In order to further elucidate the relative importance of these processes as HONO sources, we performed a multinomial linear regression analysis of the unknown HONO source with baseline production mechanisms in section 4.3.1 as variables (Eq. 4.4).

$$P_{unknown} = a + b*P_{pNO3} + c*P_{NO2het} \quad \text{(Eq. 4.4)}$$

Parameters *b* and *c* are scaling factors of the corresponding baseline HONO source terms to provide a best fit of the predicted HONO to the observed in the aged wildfire smoke sampled during RF 5. Parameter *a* denotes the residual. The optimal fit for the River of Smoke flight is a = -0.007(-0.014, -0.0008), b = 0.22 (0.15, 0.29) and c = 4.0 (2.8, 5.2). These values translate to an enhancement factor of pNO_3 photolysis relative to HNO_3 photolysis of 67, and $\gamma_{NO2\rightarrow HONO}$ of 4.0×10^{-4}. The correlation of fitted HONO secondary source with the missing HONO source strength is shown in Figure 4.1c inset (R^2 = 0.81). These results suggest a factor 4.5 smaller HONO source from pNO_3 photolysis in wildfire smoke than reported by Ye et al 2018, but a significant source of HONO from NO_2 reactive uptake to aerosol particles. It reveals the important role of tropospheric aerosol as a media for secondary HONO chemistry over fire-prone regions, in contrast to previous assumptions that aerosols are not important in daytime HONO production (Ammann et al., 1998; Bröske et al., 2003; K. Stemmler et al., 2007; Vandenboer et al., 2013; Wong et al., 2011).

We studied smoke in all flights with ages above 3 h, and the overall statistics are presented in Table S4.1. Significant enhancements in HONO concentrations, with a median value of ~55 ppt across the campaign, were observed in these aged wildfire plumes compared to background air masses. The campaign-average missing HONO source strength (0.019 ± 0.037 ppt s^{-1}) is comparable in magnitude to those obtained from aircraft studies in Michigan (0.016 ppt s^{-1}; Zhang et al., 2009) and in the southern USA (0.047 ppt s^{-1}; Ye et al., 2018)), while much smaller than that in the upper boundary layer and lower free troposphere of the North China Plain in winter and spring (0.13 and 0.18 ppt s^{-1}; Jiang et al., 2020). In addition, we observed an apparent dependence of missing HONO source strength on both candidate mechanisms in aged fire smoke across flights (Figure S4.4). We extrapolated the relationship acquired from the River of Smoke flight to aged smoke in other flights using the same set of equations to examine its universality. Figure 4.2 shows the scatter plot of inferred production rates of HONO against predicted rates by applying the multilinear fit for different flights. The symbols are colored by the effective aging metric (physical age to photolysis lifetime) which accounts for the difference in photolysis due to varying plume darkness/thickness. The missing source rates have an overall good correlation with the predicted rates with R^2 of 0.64. These results suggest that a combination of NO_2-driven and pNO_3-driven HONO sources can explain a majority of the missing HONO source strength, with relatively consistent weighting across different fires. The variance may be partially due to changes in the rate coefficient from both pathways with chemical compositions in different smoke intercepts (Z. Liu et al., 2014; Ye et al., 2017; W. Zhang et al., 2020). Meanwhile, the possibility of other HONO sources like photolysis of ortho-nitrophenols (Bejan et al., 2006) and the contribution of super-micron particles are not ruled out, and as such the pNO_3 and NO_2 reactive uptake parameters presented here are likely upper limits.

4.3.3 Contributions of Secondary HONO across Multiple Fires

We evaluate the pNO$_3$ photolysis and NO$_2$ reactive uptake sources of HONO across multiple fire plumes to assess their range of possible importance with varying plume composition and age. Here, we isolate each of these potential sources to derive an upper limit estimate on their respective parameters (Figure S4.5). Assuming the observed HONO was exclusively from pNO$_3$ photolysis, we derive the pNO$_3$ photolysis frequency $j_{p\mathrm{NO3}}$ (assuming 67% yield of HONO) for each 1 min average measurement. The range of $J(p\mathrm{NO_3})$ spans from 2.6×10^{-6} to 2.5×10^{-4} with a median value of 6.8×10^{-5}, which translates to an enhancement factor over j_{HNO3} of 73 (3, 268). This result is larger than the enhancement factors reported in recent studies (e.g., 1-30 in Romer et al., 2018), while significantly lower compared to Ye et al. (2016). Similarly, assuming the entire HONO formation was from NO$_2$ uptake on the particle surface, the calculated $\gamma_{\mathrm{NO2\rightarrow HONO}}$ ranges from 9.4×10^{-6} to 2.4×10^{-2} with a median value of 2.0×10^{-3}. The median upper-limit value is 1 to 3 orders of magnitude higher than reported in other field studies (Z. Liu et al., 2014; W. Zhang et al., 2020). This higher $\gamma_{\mathrm{NO2\rightarrow HONO}}$ value may suggest that a more efficient heterogeneous conversion from NO$_2$ to HONO is present in aged fire smoke, but its importance is strongly influenced by the assumed magnitude of the pNO$_3$ photolysis source (see Figure 4.3). The density plots of weight coefficients for the multilinear fit of HONO secondary sources for different flights is shown in Figure 4.3. The median and interquartile range of the parameter distribution across all flights are estimated to be b = 0.40 (0.22, 0.70) and c = 9.8 (4.6, 21.0). The variations from flight to flight may be due to variations in aerosol particle properties such as aerosol pH, water content, and organic nitrate to inorganic nitrate fraction, among others. The production of HONO from organic nitrate and nitroaromatic photochemistry is not well understood, and the variations in the fraction of total particulate nitrate that is inorganic nitrate may add uncertainty to our conclusions.

As shown in Section 4.3.2, it is likely that both mechanisms occur in parallel in fire plumes. Thus, we defined the range of *c* given fixed *b* values for different flights to show a more realistic range of variations. Figure 4.3 shows that the *c* values start to become negative for $b >= 0.2$ for certain flights, and the variations in *c* are small despite orders of magnitude changes in *b*. This reflects a relatively narrow range for NO_2 uptake rates in biomass burning aerosols, with $\gamma_{NO2 \rightarrow HONO}$ on the order of 10^{-4}. The results also suggest lower the photolysis rate of pNO_3 in fire smoke than reported in Ye et al. (2016), possibly due to less photosensitizer or a lower branching to HONO release after photolysis in wildfire aerosols compared to sea-salt aerosols.

To compare the importance of direct HONO emissions to the secondary HONO sources evaluated above, we used a box model to simulate the evolution of two fire plumes with *in situ* plume sampling including a sequence of crosswind intercepts downwind of the fire. We added the secondary HONO sources to the model mechanism using the regression model parameters and found improved HONO simulations as compared to observations in both fires (Figure 4.4). Rapid photochemical evolution occurs in daytime fire plumes, and the relative contributions of different HONO sources change rapidly as plumes age. From modeled apportionment of the ambient HONO sources, we found that pNO_3 photolysis becomes more important with aging and more predominant in less polluted events (i.e., lower NO_x loading), while NO_2-related reactions and homogeneous HONO formation are more important in early stages of the plume and more polluted events. Model simulation for other compounds is shown in Figure S4.6.

The primarily emitted HONO is highly localized to the source region (< 1 h transport) due to fast photolytic loss, and the secondary sources sustain the HONO levels in aged smoke. Despite the dominance of secondary HONO chemistry in aged smoke, it is almost negligible for young plumes with physical age below 1 h compared to primary emissions. Secondarily produced HONO

from NO_2-driven and pNO_3-driven sources only account for <4% of measured HONO in young plumes (age < 1h) while making up >90% in old smoke (age > 2h).

4.4 CONCLUSIONS

We provide direct constraints on the production of secondary HONO in daytime wildfire smoke using airborne measurements in the Western United States. Our observations suggest that HONO levels in aged (> 1 hr) fire smoke are dominated by secondary sources that include NO_2 reactive uptake and pNO_3 photolysis, and highlight the potential importance of biomass burning aerosols as a media for secondary HONO production. A simple multi-linear regression model derived from the River of Smoke case study was found to explain 65% of the variance in all aged smoke detected in WE-CAN. A median enhancement factor of 45 for pNO_3 photolysis frequency relative to HNO_3 and $\gamma_{NO2\rightarrow HONO}$ of 4.0×10^{-4} were derived from a multilinear regression analysis for the River of Smoke Fire and could be extended to all fire plumes sampled in WE-CAN. Box model simulations with additional secondary HONO mechanisms improve the model-observation agreement in HONO, especially for more aged plumes. Our observations extend previous studies of HONO sources to wildfire plumes decoupled from the ground, and offer a unique range of key parameters, which could help better interpret field data and initiate models for biomass burning plumes. Sustained secondary HONO production in aged wildfire smoke will contribute to enhanced radical cycling even in the far field. The relative contributions of different secondary HONO sources may have implications on the photochemistry of O_3, PAN, and organic nitrate, as well as the lifetime of NO_x. Future laboratory efforts to develop more robust parameterizations for each governing pathway will be important to reduce uncertainties and better characterize the spatiotemporal HONO evolution.

4.5 REFERENCES

Acker, K., Spindler, G., & Brüggemann, E. (2004). Nitrous and nitric acid measurements during the INTERCOMP2000 campaign in Melpitz. *Atmospheric Environment*, *38*(38), 6497–6505. https://doi.org/10.1016/J.ATMOSENV.2004.08.030

Amedro, D., Parker, A. E., Schoemaecker, C., & Fittschen, C. (2011). Direct observation of OH radicals after 565nm multi-photon excitation of NO2 in the presence of H2O. *Chemical Physics Letters*, *1–3*(513), 12–16. https://doi.org/10.1016/J.CPLETT.2011.07.062

Ammann, M., Kalberer, M., Jost, D. T., Tobler, L., Rössler, E., Piguet, D., et al. (1998). Heterogeneous production of nitrous acid on soot in polluted air masses. *Nature 1998 395:6698*, *395*(6698), 157–160. https://doi.org/10.1038/25965

Aubin, D. G., & Abbatt, J. P. D. (2007). Interaction of NO2 with hydrocarbon soot: focus on HONO yield, surface modification, and mechanism. *The Journal of Physical Chemistry. A*, *111*(28), 6263–6273. https://doi.org/10.1021/JP068884H

Bao, F., Li, M., Zhang, Y., Chen, C., & Zhao, J. (2018). Photochemical Aging of Beijing Urban PM2.5: HONO Production. *Environmental Science and Technology*, *52*(11), 6309–6316. https://doi.org/10.1021/ACS.EST.8B00538/SUPPL_FILE/ES8B00538_SI_001.PDF

Bejan, I., Abd El Aal, Y., Barnes, I., Benter, T., Bohn, B., Wiesen, P., & Kleffmann, J. (2006). The photolysis of ortho-nitrophenols: a new gas phase source of HONO. *Physical Chemistry Chemical Physics*, *8*(17), 2028–2035. https://doi.org/10.1039/B516590C

Brock, C. A., Williamson, C., Kupc, A., Froyd, K. D., Erdesz, F., Wagner, N., et al. (2019). Aerosol size distributions during the Atmospheric Tomography Mission (ATom): Methods, uncertainties, and data products. *Atmospheric Measurement Techniques*, *12*(6), 3081–3099. https://doi.org/10.5194/AMT-12-3081-2019

Bröske, R., Kleffmann, J., & Wiesen, P. (2003). Atmospheric Chemistry and Physics. *European Geosciences Union*, *3*(3), 469–474. Retrieved from www.atmos-chem-phys.org/acp/3/469/

Carr, S., Heard, D. E., & Blitz, M. A. (2009). Comment on "atmospheric hydroxyl radical production from electronically excited NO2 and H2O." *Science*, *324*(5925). https://doi.org/10.1126/SCIENCE.1166669/SUPPL_FILE/CARR_SOM.PDF

Chai, J., Dibb, J. E., Anderson, B. E., Bekker, C., Blum, D. E., Heim, E., et al. (2021). Isotopic evidence for dominant secondary production of HONO in near-ground wildfire plumes. *Atmospheric Chemistry and Physics*, *21*(17), 13077–13098. https://doi.org/10.5194/ACP-21-13077-2021

Colussi, A. J., Enami, S., Yabushita, A., Hoffmann, M. R., Liu, W. G., Mishra, H., & Goddard, W. A. (2013). Tropospheric aerosol as a reactive intermediate. *Faraday Discussions*, *165*(0), 407–420. https://doi.org/10.1039/C3FD00040K

Czader, B. H., Rappengï Uck, B., Percell, P., Byun, D. W., Ngan, F., & Kim, S. (2012). Modeling nitrous acid and its impact on ozone and hydroxyl radical during the Texas Air Quality Study 2006. *Atmos. Chem. Phys*, *12*, 6939–6951. https://doi.org/10.5194/acp-12-

6939-2012

Finlayson-Pitts, B. J., Wingen, L. M., Sumner, A. L., Syomin, D., & Ramazan, K. A. (2003). The heterogeneous hydrolysis of NO2 in laboratory systems and in outdoor and indoor atmospheres: An integrated mechanism. *Physical Chemistry Chemical Physics*, *5*(2), 223–242. https://doi.org/10.1039/B208564J

Garofalo, L. A., Pothier, M. A., Levin, E. J. T., Campos, T., Kreidenweis, S. M., & Farmer, D. K. (2019). Emission and Evolution of Submicron Organic Aerosol in Smoke from Wildfires in the Western United States. *ACS Earth and Space Chemistry*, *3*(7), 1237–1247. https://doi.org/10.1021/acsearthspacechem.9b00125

George, C., Strekowski, R. S., Kleffmann, J., Stemmler, K., & Ammann, M. (2005). Photoenhanced uptake of gaseous NO2 on solid organic compounds: a photochemical source of HONO? *Faraday Discussions*, *130*(0), 195–210. https://doi.org/10.1039/B417888M

Gustafsson, R. J., Kyriakou, G., & Lambert, R. M. (2008). The molecular mechanism of tropospheric nitrous acid production on mineral dust surfaces. *Chemphyschem : A European Journal of Chemical Physics and Physical Chemistry*, *9*(10), 1390–1393. https://doi.org/10.1002/CPHC.200800259

Han, C., Yang, W., Wu, Q., Yang, H., & Xue, X. (2016). Heterogeneous Photochemical Conversion of NO2 to HONO on the Humic Acid Surface under Simulated Sunlight. *Environmental Science and Technology*, *50*(10), 5017–5023. https://doi.org/10.1021/ACS.EST.5B05101/SUPPL_FILE/ES5B05101_SI_001.PDF

Haskins, J. D., Lopez-Hilfiker, F. D., Lee, B. H., Shah, V., Wolfe, G. M., DiGangi, J., et al. (2019). Anthropogenic Control Over Wintertime Oxidation of Atmospheric Pollutants. *Geophysical Research Letters*, *46*(24), 14826–14835. https://doi.org/10.1029/2019GL085498

Jiang, Y., Xue, L., Gu, R., Jia, M., Zhang, Y., Wen, L., et al. (2020). Sources of nitrous acid (HONO) in the upper boundary layer and lower free troposphere of the North China Plain: Insights from the Mount Tai Observatory. *Atmospheric Chemistry and Physics*, *20*(20), 12115–12131. https://doi.org/10.5194/ACP-20-12115-2020

Juncosa Calahorrano, J. F., Lindaas, J., O'Dell, K., Palm, B. B., Peng, Q., Flocke, F., et al. (2020). Daytime Oxidized Reactive Nitrogen Partitioning in Western U.S. Wildfire Smoke Plumes. *Journal of Geophysical Research: Atmospheres*, e2020JD033484. https://doi.org/10.1029/2020JD033484

Khalizov, A. F., Cruz-Quinones, M., & Zhang, R. (2010). Heterogeneous reaction of NO2 on fresh and coated soot surfaces. *Journal of Physical Chemistry A*, *114*(28), 7516–7524. https://doi.org/10.1021/jp1021938

Kleffmann, J., Becker, K. H., Lackhoff, M., & Wiesen, P. (1999). Heterogeneous conversion of NO2 on carbonaceous surfaces. *Physical Chemistry Chemical Physics*, *1*(24), 5443–5450. https://doi.org/10.1039/A905545B

Kleffmann, J., Gavriloaiei, T., Hofzumahaus, A., Holland, F., Koppmann, R., Rupp, L., et al. (2005). Daytime formation of nitrous acid: A major source of OH radicals in a forest. *Geophysical Research Letters*, *32*(5), 1–4. https://doi.org/10.1029/2005GL022524

Lee, B. H., Wood, E. C., Herndon, S. C., Lefer, B. L., Luke, W. T., Brune, W. H., et al. (2013). Urban measurements of atmospheric nitrous acid: A caveat on the interpretation of the HONO photostationary state. *Journal of Geophysical Research: Atmospheres*, *118*(21), 12,274-12,281. https://doi.org/10.1002/2013JD020341

Lee, J. D., Whalley, L. K., Heard, D. E., Stone, D., Dunmore, R. E., Hamilton, J. F., et al. (2016). Detailed budget analysis of HONO in central London reveals a missing daytime source. *Atmos. Chem. Phys*, *16*, 2747–2764. https://doi.org/10.5194/acp-16-2747-2016

Li, S., Matthews, J., & Sinha, A. (2008). Atmospheric hydroxyl radical production from electronically excited NO 2 and H2O. *Science*, *319*(5870), 1657–1660. https://doi.org/10.1126/SCIENCE.1151443/SUPPL_FILE/LI.SOM.PDF

Li, X., Rohrer, F., Hofzumahaus, A., Brauers, T., Häseler, R., Bohn, B., et al. (2014). Missing gas-phase source of HONO inferred from Zeppelin measurements in the troposphere. *Science*, *344*(6181), 292–296. https://doi.org/10.1126/SCIENCE.1248999/SUPPL_FILE/LI_SM.PDF

Lindaas, J., Pollack, I. B., Garofalo, L. A., Pothier, M. A., Farmer, D. K., Kreidenweis, S. M., et al. (2021). Emissions of Reactive Nitrogen From Western U.S. Wildfires During Summer 2018. *Journal of Geophysical Research: Atmospheres*, *126*(2), e2020JD032657. https://doi.org/10.1029/2020JD032657

Liu, X., Cheng, Y., Zhang, Y., Jung, J., Sugimoto, N., Chang, S. Y., et al. (2008). Influences of relative humidity and particle chemical composition on aerosol scattering properties during the 2006 PRD campaign. *Atmospheric Environment*, *42*(7), 1525–1536. https://doi.org/10.1016/J.ATMOSENV.2007.10.077

Liu, Z., Wang, Y., Costabile, F., Amoroso, A., Zhao, C., Greg Huey, L., et al. (2014). Evidence of Aerosols as a Media for Rapid Daytime HONO Production over China. https://doi.org/10.1021/es504163z

Lu, X., Wang, Y., Li, J., Shen, L., & Fung, J. C. H. (2018). Evidence of heterogeneous HONO formation from aerosols and the regional photochemical impact of this HONO source. *Environmental Research Letters*, *13*(11). https://doi.org/10.1088/1748-9326/AAE492

Monge, M. E., D'Anna, B., Mazri, L., Giroir-Fendler, A., Ammann, M., Donaldson, D. J., & George, C. (2010). Light changes the atmospheric reactivity of soot. *Proceedings of the National Academy of Sciences*, *107*(15), 6605–6609. https://doi.org/10.1073/PNAS.0908341107

Ndour, M., D'Anna, B., George, C., Ka, O., Balkanski, Y., Kleffmann, J., et al. (2008). Photoenhanced uptake of NO2 on mineral dust: Laboratory experiments and model simulations. *Geophysical Research Letters*, *35*(5). https://doi.org/10.1029/2007GL032006

Neuman, J. A., Trainer, M., Brown, S. S., Min, K.-E., Nowak, J. B., Parrish, D. D., et al. (2016). HONO emission and production determined from airborne measurements over the Southeast U.S. *Journal of Geophysical Research: Atmospheres*, *121*(15), 9237–9250. https://doi.org/10.1002/2016JD025197

Palm, B. B., Peng, Q., Fredrickson, C. D., Lee, B. H., Garofalo, L. A., Pothier, M. A., et al. (2020). Quantification of organic aerosol and brown carbon evolution in fresh wildfire plumes. *Proceedings of the National Academy of Sciences of the United States of America*,

117(47), 29469–29477. https://doi.org/10.1073/pnas.2012218117

Peng, Q., Palm, B. B., Melander, K. E., Lee, B. H., Hall, S. R., Ullmann, K., et al. (2020). HONO Emissions from Western U.S. Wildfires Provide Dominant Radical Source in Fresh Wildfire Smoke. *Environmental Science and Technology*, *54*(10), 5954–5963. https://doi.org/10.1021/acs.est.0c00126

Peng, Q., Palm, B. B., Fredrickson, C. D., Lee, B. H., Hall, S. R., Ullmann, K., et al. (2021). Observations and Modeling of NO xPhotochemistry and Fate in Fresh Wildfire Plumes. *ACS Earth and Space Chemistry*, *5*(10), 2652–2667. https://doi.org/10.1021/ACSEARTHSPACECHEM.1C00086/SUPPL_FILE/SP1C00086_SI_001.PDF

R. Crilley, L., Louisa Kramer, D. Pope, F., K. Whalley, L., R. Cryer, D., E. Heard, D., et al. (2016). On the interpretation of in situ HONO observations via photochemical steady state. *Faraday Discussions*, *189*(0), 191–212. https://doi.org/10.1039/C5FD00224A

Ridley, B. A., & Grahek, F. E. (1990). A Small, Low Flow, High Sensitivity Reaction Vessel for NO Chemiluminescence Detectors. *Journal of Atmospheric and Oceanic Technology*, *7*(2), 307–311. https://doi.org/10.1175/1520-0426(1990)007<0307:aslfhs>2.0.co;2

Romer, P. S., Wooldridge, P. J., Crounse, J. D., Kim, M. J., Wennberg, P. O., Dibb, J. E., et al. (2018). Constraints on Aerosol Nitrate Photolysis as a Potential Source of HONO and NO x. *Environmental Science and Technology*, *52*(23), 13738–13746. https://doi.org/10.1021/acs.est.8b03861

Shetter, R. E., & Müller, M. (1999). Photolysis frequency measurements using actinic flux spectroradiometry during the PEM-Tropics mission: Instrumentation description and some results. *Journal of Geophysical Research: Atmospheres*, *104*(D5), 5647–5661. https://doi.org/10.1029/98JD01381

Shi, Q., Tao, Y., Krechmer, J. E., Heald, C. L., Murphy, J. G., Kroll, J. H., & Ye, Q. (2021). Laboratory Investigation of Renoxification from the Photolysis of Inorganic Particulate Nitrate. *Environmental Science and Technology*, *55*(2), 854–861. https://doi.org/10.1021/ACS.EST.0C06049

Sörgel, M., Trebs, I., Serafimovich, A., Moravek, A., Held, A., & Zetzsch, C. (2011). Simultaneous HONO measurements in and above a forest canopy: Influence of turbulent exchange on mixing ratio differences. *Atmospheric Chemistry and Physics*, *11*(2), 841–855. https://doi.org/10.5194/ACP-11-841-2011

Stemmler, K., Ndour, M., Elshorbany, Y., Kleffmann, J., D'Anna, B., George, C., et al. (2007). Light induced conversion of nitrogen dioxide into nitrous acid on submicron humic acid aerosol. *Atmospheric Chemistry and Physics*, *7*(16), 4237–4248. https://doi.org/10.5194/acp-7-4237-2007

Stemmler, Konrad, Ammann, M., Donders, C., Kleffmann, J., & George, C. (2006). Photosensitized reduction of nitrogen dioxide on humic acid as a source of nitrous acid. *Nature 2006 440:7081*, *440*(7081), 195–198. https://doi.org/10.1038/nature04603

Su, H., Cheng, Y., Wiedensohler, A., Fang Cheng, Y., Shao, M., Feng Gao, D., et al. (2008). PRIDE-PRD experiment in China. *Article in Journal of Geophysical Research Atmospheres*, *113*, 14312. https://doi.org/10.1029/2007JD009060

Tan, Z., Lu, K., Hofzumahaus, A., Fuchs, H., Bohn, B., Holland, F., et al. (2019). Experimental budgets of OH, HO $_2$, and RO $_2$ radicals and implications for ozone formation in the Pearl River Delta in China 2014. *Atmospheric Chemistry and Physics*, *19*(10), 7129–7150. https://doi.org/10.5194/acp-19-7129-2019

Vandenboer, T. C., Brown, S. S., Murphy, J. G., Keene, W. C., Young, C. J., Pszenny, A. A. P., et al. (2013). Understanding the role of the ground surface in HONO vertical structure: High resolution vertical profiles during NACHTT-11. *Journal of Geophysical Research: Atmospheres*, *118*(17), 10,155-10,171. https://doi.org/10.1002/JGRD.50721

Veres, P. R., Roberts, J. M., Wild, R. J., Edwards, P. M., Brown, S. S., Bates, T. S., et al. (2015). Peroxynitric acid (HO 2 NO 2) measurements during the UBWOS 2013 and 2014 studies using iodide ion chemical ionization mass spectrometry. *Atmos. Chem. Phys*, *15*, 8101–8114. https://doi.org/10.5194/acp-15-8101-2015

Wang, S., Coggon, M. M., Gkatzelis, G. I., Warneke, C., Bourgeois, I., Ryerson, T., et al. (2021). Chemical Tomography in a Fresh Wildland Fire Plume: A Large Eddy Simulation (LES) Study. *Journal of Geophysical Research: Atmospheres*, *126*(18). https://doi.org/10.1029/2021JD035203

Wong, K. W., Lefer, B. L., Rappenglück, B., & Stutz, J. (2011). Vertical profiles of nitrous acid in the nocturnal urban atmosphere of Houston, TX. *Atmospheric Chemistry and Physics*, *11*(8), 3595–3609. https://doi.org/10.5194/ACP-11-3595-2011

Wong, K. W., Tsai, C., Lefer, B., Haman, C., Grossberg, N., Brune, W. H., et al. (2012). Daytime HONO vertical gradients during SHARP 2009 in Houston, TX. *Atmospheric Chemistry and Physics*, *12*(2), 635–652. https://doi.org/10.5194/ACP-12-635-2012

Ye, C., Zhou, X., Pu, D., Stutz, J., Festa, J., Spolaor, M., et al. (2015). Comment on "Missing gas-phase source of HONO inferred from Zeppelin measurements in the troposphere." *Science*, *348*(6241), 1326d. https://doi.org/10.1126/SCIENCE.AAA1992/ASSET/93EBB8F4-0863-4D0B-8CB1-303C8314F3B0/ASSETS/GRAPHIC/348_1326D_F1.JPEG

Ye, C., Zhou, X., Pu, D., Stutz, J., Festa, J., Spolaor, M., et al. (2016). Rapid cycling of reactive nitrogen in the marine boundary layer. *Nature*, *532*(7600), 489–491. https://doi.org/10.1038/nature17195

Ye, C., Zhang, N., Gao, H., & Zhou, X. (2017). Photolysis of Particulate Nitrate as a Source of HONO and NOx. *Environmental Science and Technology*, *51*(12), 6849–6856. https://doi.org/10.1021/ACS.EST.7B00387

Ye, C., Zhou, X., Pu, D., Stutz, J., Festa, J., Spolaor, M., et al. (2018). Tropospheric HONO distribution and chemistry in the southeastern US. *Atmos. Chem. Phys*, *18*, 9107–9120. https://doi.org/10.5194/acp-18-9107-2018

Zhang, N., Zhou, X., Shepson, P. B., Gao, H., Alaghmand, M., & Stirm, B. (2009). Aircraft measurement of HONO vertical profiles over a forested region. *Geophysical Research Letters*, *36*(15). https://doi.org/10.1029/2009GL038999

Zhang, W., Tong, S., Jia, C., Wang, L., Liu, B., Tang, G., et al. (2020). Different HONO Sources for Three Layers at the Urban Area of Beijing. *Environmental Science and Technology*, *54*(20), 12870–12880.

https://doi.org/10.1021/ACS.EST.0C02146/SUPPL_FILE/ES0C02146_SI_001.PDF

Zhou, X., Beine, H. J., Honrath, R. E., Fuentes, J. D., Simpson, W., Shepson, P. B., & Bottenheim, J. W. (2001). Snowpack photochemical production of HONO: A major source of OH in the Arctic boundary layer in springtime. *Geophysical Research Letters*, *28*(21), 4087–4090. https://doi.org/10.1029/2001GL013531

Zhou, X., He, Y., Huang, G., Thornberry, T. D., Carroll, M. A., & Bertman, S. B. (2002). Photochemical production of nitrous acid on glass sample manifold surface. *Geophysical Research Letters*, *29*(14), 26–1. https://doi.org/10.1029/2002GL015080

Zhou, X., Gao, H., He, Y., Huang, G., Bertman, S. B., Civerolo, K., & Schwab, J. (2003). Nitric acid photolysis on surfaces in low-NOx environments: Significant atmospheric implications. *Geophysical Research Letters*, *30*(23), 2217. https://doi.org/10.1029/2003GL018620

Zhou, X., Zhang, N., Teravest, M., Tang, D., Hou, J., Bertman, S., et al. (2011). Nitric acid photolysis on forest canopy surface as a source for tropospheric nitrous acid. *Nature Geoscience*, 29. https://doi.org/10.1038/NGEO1164

4.6 TABLES

Table S4.1. Statistical summary of observations for aged fire plumes (> 3h) during WE-CAN (145 observations in total).

	Average	Median	5th percentile	25th percentile	75th percentile	95th percentile
HONO (ppb)	0.61	0.057	0.023	0.038	0.085	0.53
NO_2 (ppb)	0.59	0.30	0.12	0.19	0.62	1.47
HONO/NO_2	0.25	0.17	0.07	0.12	0.28	0.58
pNO_3 (ppb)	1.68	0.74	0.07	0.22	2.00	7.57
T (K)	278.6	277.8	269.0	275.5	281.1	290.3
RH (%)	33.4	32.8	12.0	21.5	38.6	70.9
WS (m s^{-1})	7.35	7.21	1.76	4.53	9.19	14.6

4.7 FIGURES

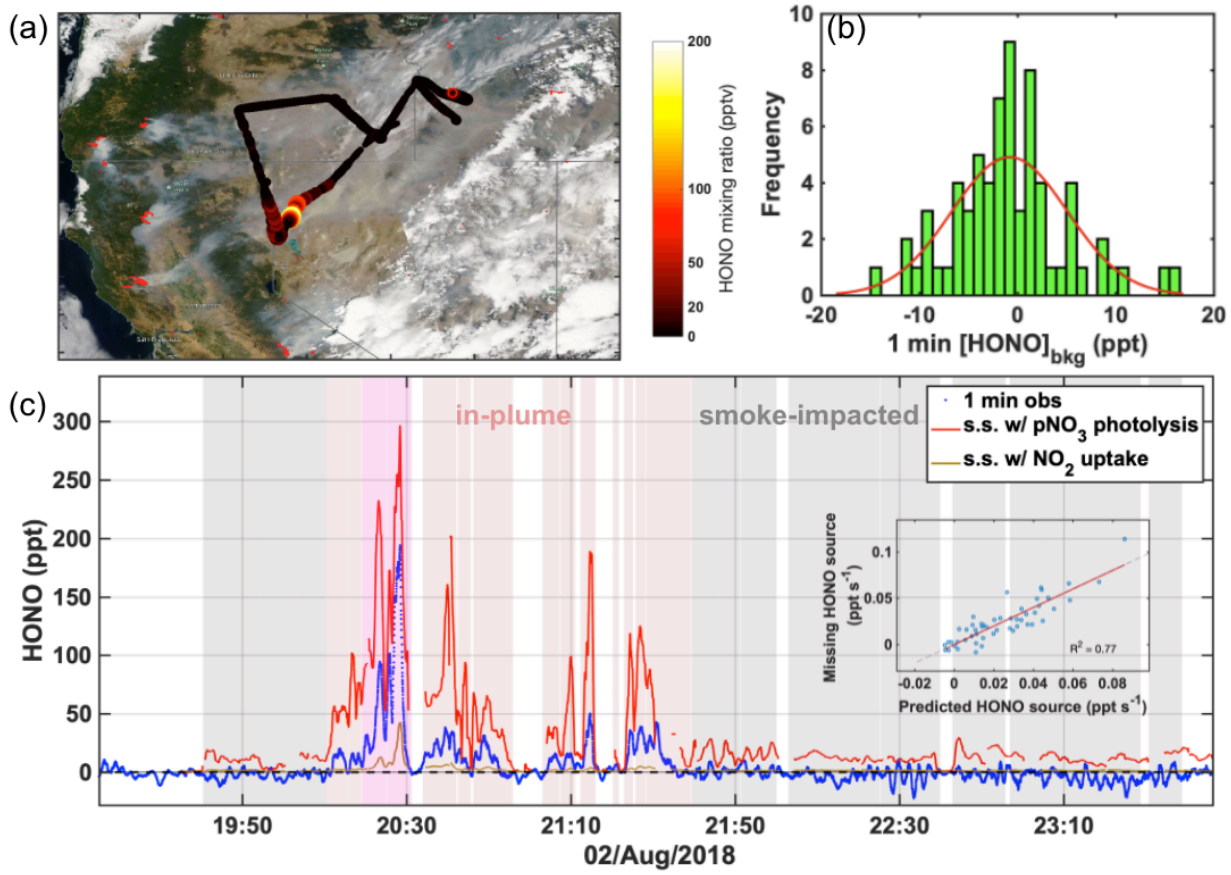

Figure 4.1. (a) MODIS VIIRS reflectance mapping with overlaid flight track color coded by 1-min average HONO mixing ratios (pptv) on August 2, 2018. Orange dots are active fires. (b) 1-min average HONO mixing ratios by CIMS for background air. Histogram fit: mu = -0.75, sigma = 4.6. (c) Steady state (s.s.) estimates of HONO for different potential secondary source mechanisms and observed HONO. Red shading denotes in-plume samples, magenta shading denotes measurements potentially affected by fresher plume intrusions, and gray shading denotes smoke-impacted backgrounds. The inset is the correlation between predicted HONO source strength using multilinear regression and missing HONO source strength.

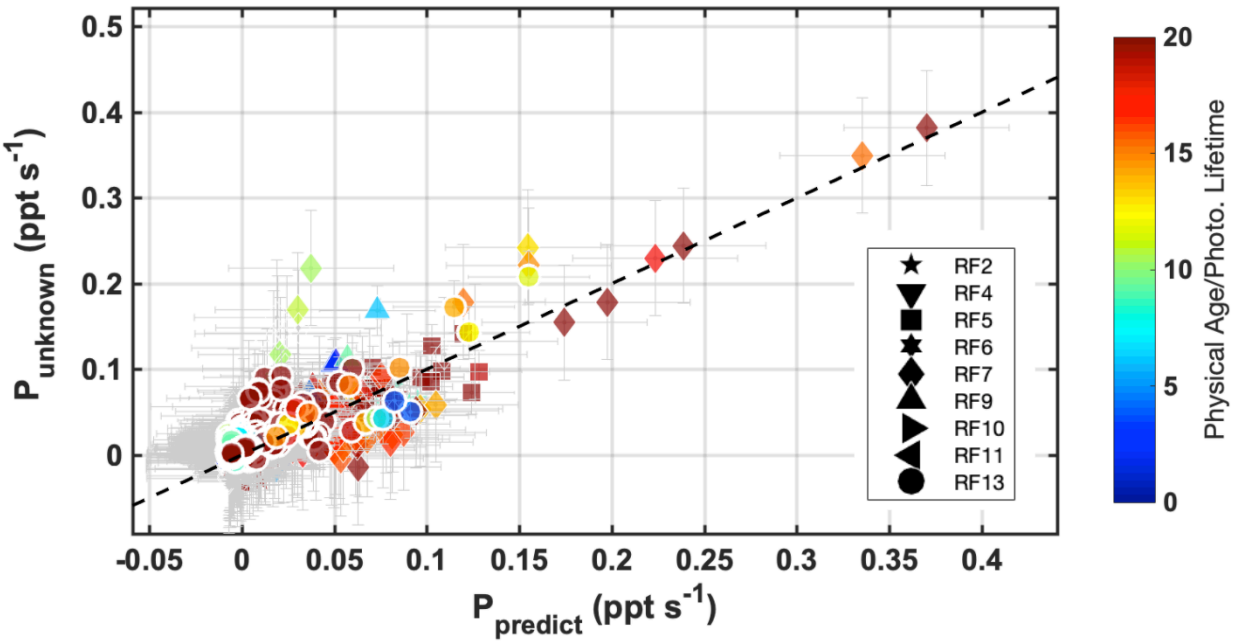

Figure 4.2. Scatter plot of the inferred HONO source strength ($P_{unknown}$) against that predicted from multilinear regression ($P_{predict}$) using River of Smoke parameters. Each point represents a 1-min average and is colored by the ratio of plume physical age to HONO photolysis lifetime. The error bars represent the uncertainties from the regression coefficients. A 1:1 line (black dashed) is shown for reference. The R^2 value for the least squares fit for the scatter plot was 0.64.

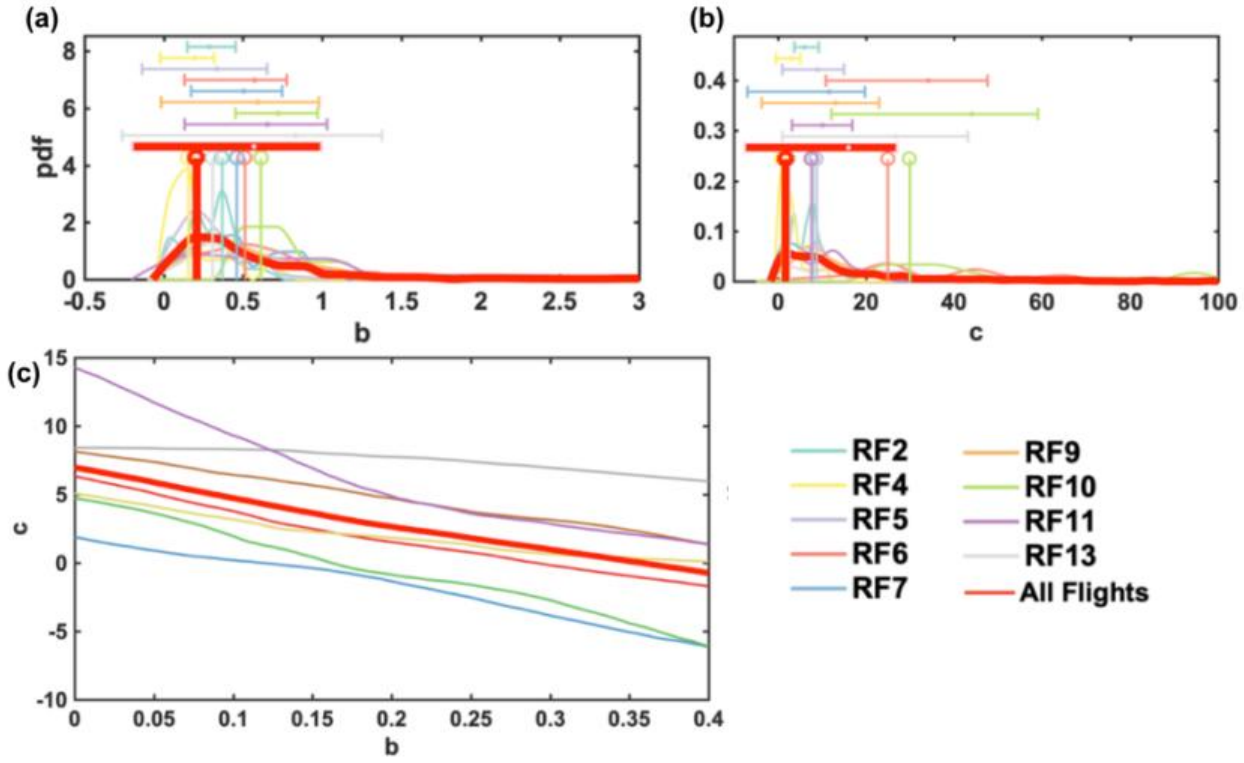

Figure 4.3. Histograms of weight coefficients (a) *b* and (b) *c* for the multilinear fit of HONO secondary sources for different flights ($P_{unknown} = a + b*P_{pNO3} + c*P_{NO2het}$) assuming each source is exclusive. The all-flight average distribution is shown in red. Vertical lines indicate the mode value for each flight. Overhead error bars denote mean ± standard deviation for each flight. The median and interquartile range is 0.40 and (0.22,0.70) for b, and 9.8 and (4.6, 21.0) for c. (c) Variations of c with increasing b assuming both sources contribute to HONO production. Each curve represents one flight and the red curve denotes the median of all flights.

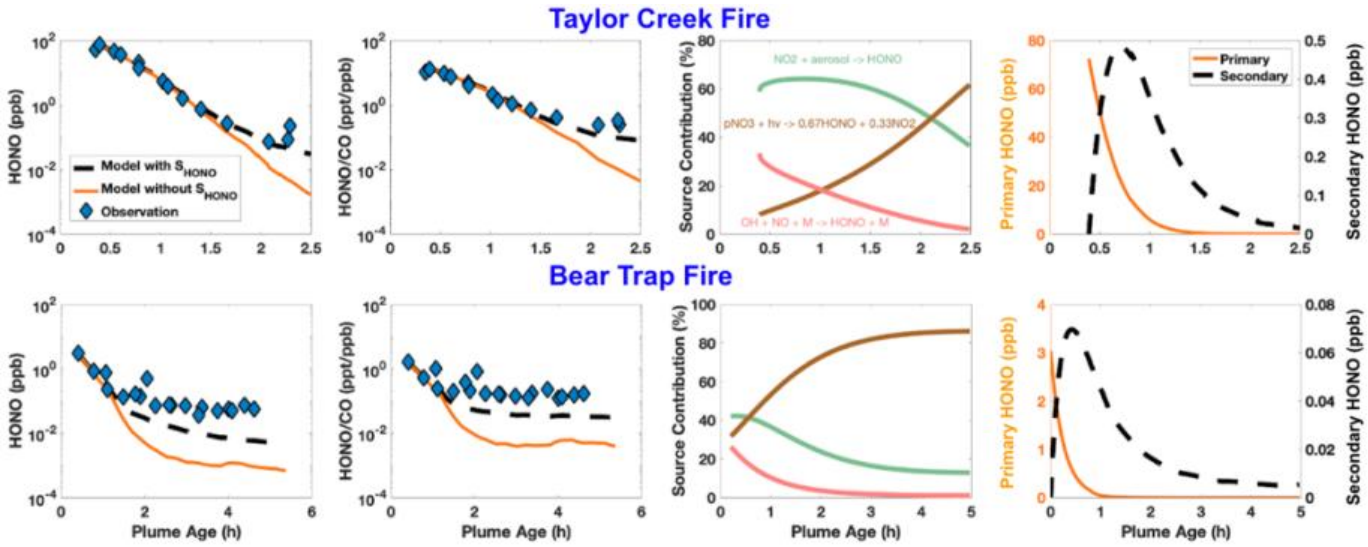

Figure 4.4. Box model simulations with and without secondary HONO sources for Taylor Creek Fire and Bear Trap Fire.

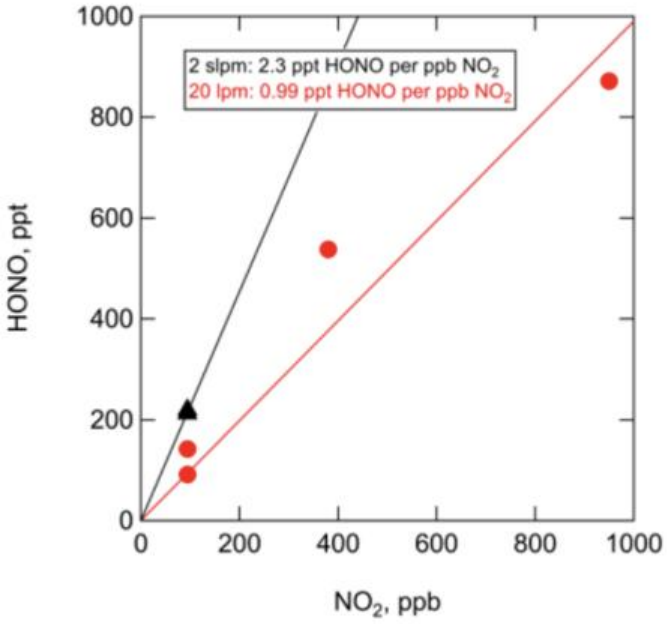

Figure S4.1. NO2-to-HONO conversion in the UW I-CIMS tubing.

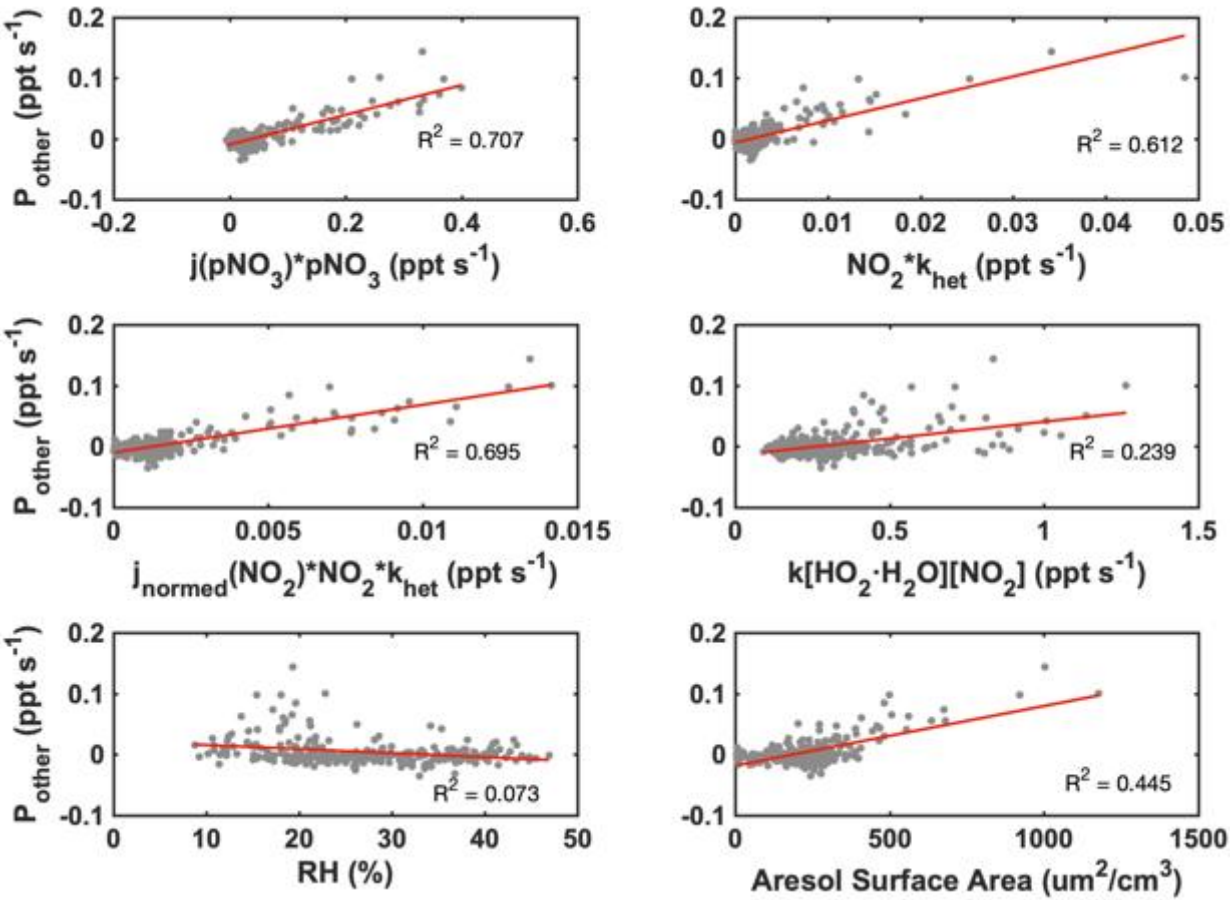

Figure S4.2. Correlation analysis of 1-min average additional sources for River of Smoke Fire. Binned average and standard deviations.

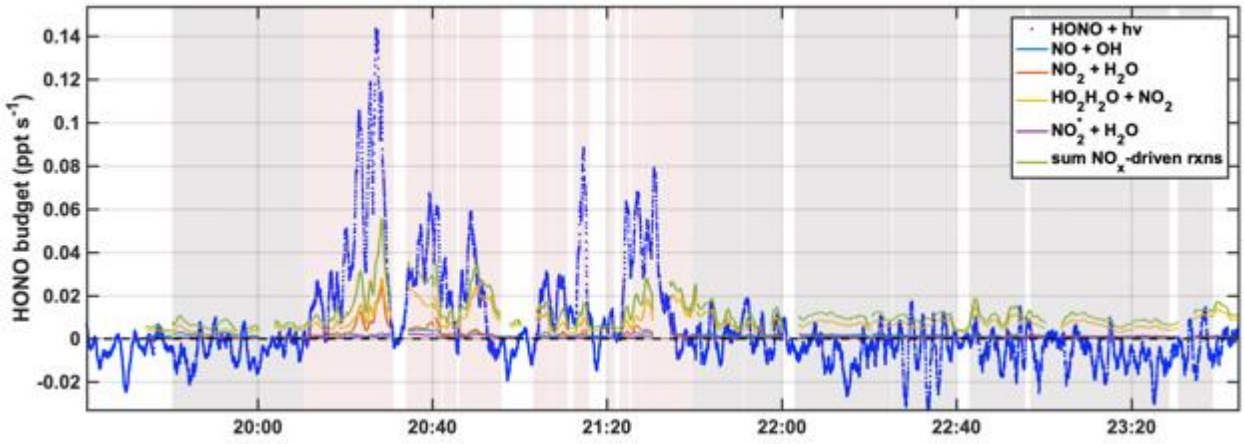

Figure S4.3. Turnover rates of NO_x-driven production and losses of HONO in River of Smoke Fire. Red shading denotes in-plume samples, and gray shading denotes smoke-impacted backgrounds.

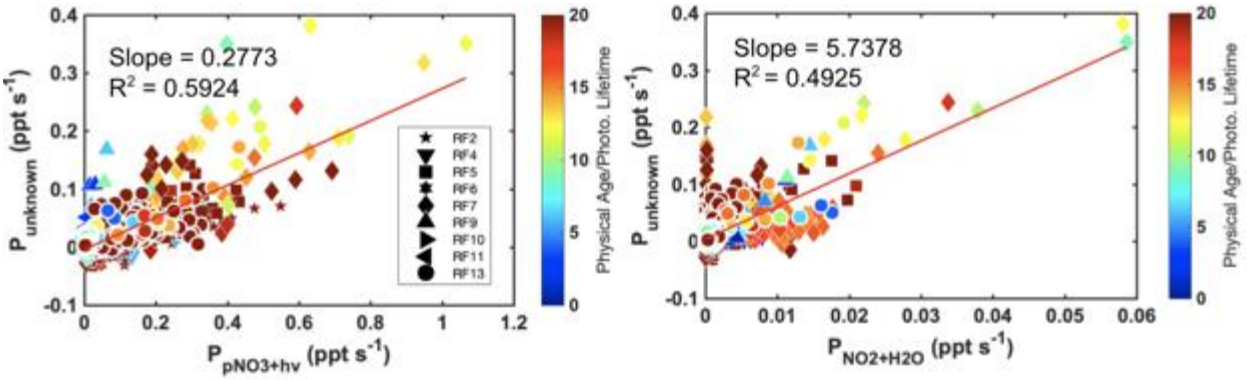

Figure S4.4. Correlation plot for unknown HONO source strength versus deduced HONO secondary source strength from (left) particle nitrate photolysis and (right) NO_2 heterogeneous hydrolysis for all aged smoke (>3 h physical age) in WE-CAN.

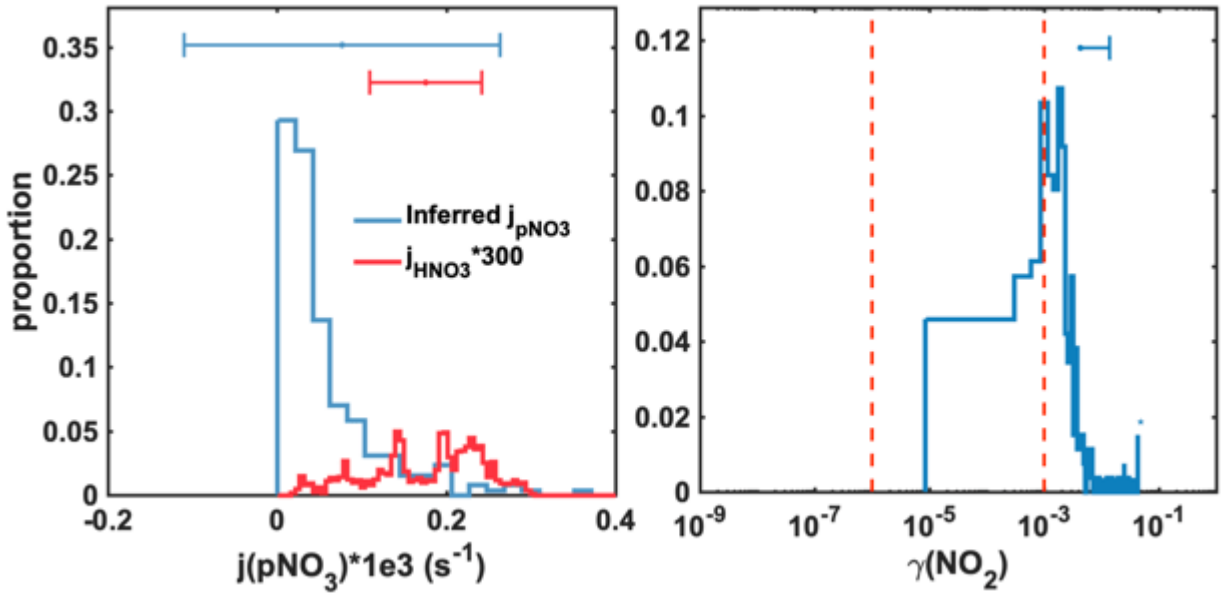

Figure S4.5. Histogram distribution of inferred (assuming all HONO from one source exclusively) versus observed parameters. (left) photolysis frequency of particle nitrate; (right) uptake coefficients of NO_2 to aerosol in River of Smoke Fire. Red dashed lines are the range of literature reported values.

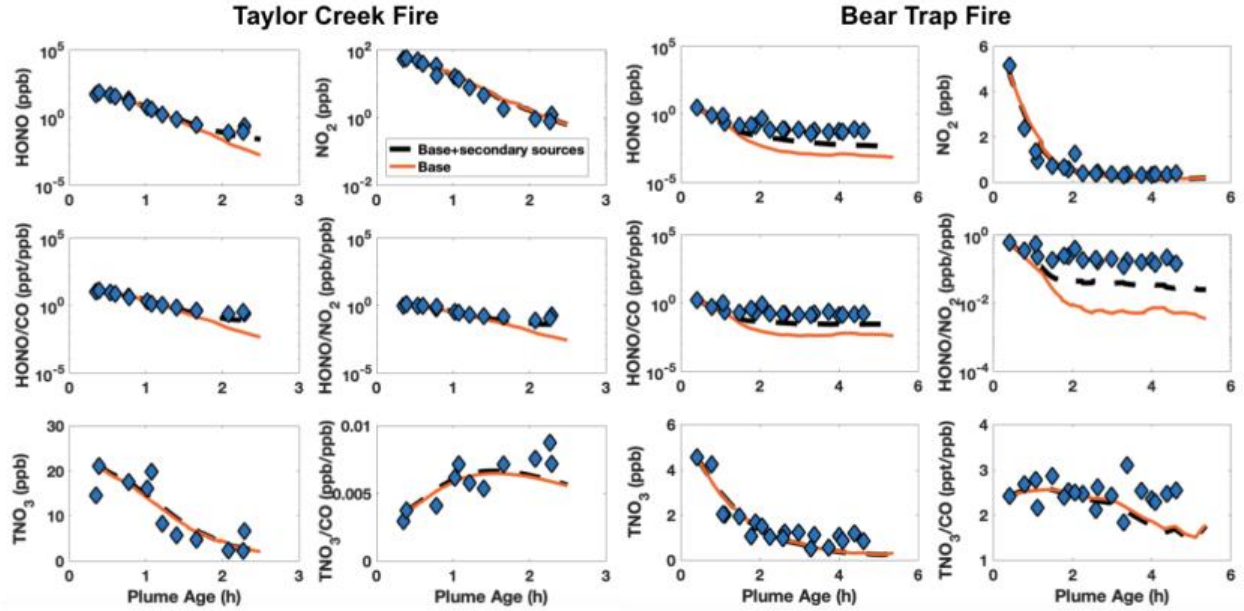

Figure S4.6. Box model simulations with and without secondary HONO sources for (left) Taylor Creek Fire and (right) Bear Trap Fire.

CHAPTER 5. CONCLUSIONS

5.1 SUMMARY OF RESULTS

In this work, I compiled an emission estimate of HONO from a variety of fire plume measurements, determined the major factors affecting its magnitude, evaluated the potential existence and relative importance of secondary HONO sources, and applied these observation constraints in atmospheric box models for more accurate descriptions of the effects of fire HONO emissions on the formation of air quality relevant secondary pollutants such as O_3 and particulate nitrate.

The WE-CAN campaign offers an unprecedented rich dataset with comprehensive measurements of over 250 wildfire plume transects, which enables detailed investigation of the complexities of reactive nitrogen chemistry in authentic smoke. Our University of Washington Iodide adduct Chemical Ionization Mass Spectrometer (UW-CIMS) onboard detects a range of nitrogen-containing organic compounds at high time resolution (2 Hz), allowing systematic diagnosis of the key nitrogen species that previous studies are short of. In Chapter 2, I documented the role of HONO as a major component of reactive nitrogen emissions from wildfires and the main driver of initial photochemical oxidation. I analyzed *in situ* measurements of HONO and NO_x and showed that the HONO/NO_x emission ratios were generally factors of 2 or higher than previous studies, revealing a significant underestimate of HONO primary emissions in earlier studies due to a lack of sampling close to large wildfires and/or instrumental artifacts such as NO_x instruments measuring HONO as NO_x due to its photolysis in the instrument. I found HONO enhancement ratios scale with modified combustion efficiency and certain nitrogenous trace gases, which may be useful to estimate HONO release when HONO observations at early plume stages are lacking. The study on HONO emission characteristics and limiting factors helps better estimate

or predict HONO emission ratio and its contribution to the primary radical source. I performed a radical budget analysis and found that HONO photolysis alone is the most important single primary source observed in fresh wildfire plumes, contributing over 90% in plumes with age shorter than an hour. The dominant role of HONO as the primary radical source, and its relatively rapid decay, suggests that wildfire plumes are highly photochemically active in the first few hours after emission, and then become much less active thereafter.

In Chapter 3, I investigated the rapid post-emission chemistry based on observation and simulation of four fire plumes with known source locations and fuel types sampled in a pseudo-Lagrangian approach. I studied near-source fire emissions and its impact on subsequent gas-phase photochemistry in plumes. Using a chemically explicit box model, I simulated the fundamental chemical behaviors of selected key species for different fires, and found current chemical schemes is inadequate to describing the evolution of NO_x into its oxidation products. The model predicts that the majority of emitted NO_x (96% ± 2%) is converted into PAN (27% ± 8%) and the sum of gas and particulate HNO_3 (29% ± 5%) within a few hours of plume evolution. In two of the plumes with the highest initial NO_x and HONO, the default model significantly underestimates the observed dilution-normalized decay rate of NO_x with plume age. I investigated several potential causes of this discrepancy, and illustrated with both modeling and observational evidence that uncharacterized organic nitrogen compounds (presumably organic nitrates) in the smoke plume may be partly responsible for the rapid loss of NO_x within the young smoke plumes. This organic nitrogen reservoir can be similar in magnitude to that of PAN, and thus represents an important fate of NO_x with uncertain impacts on downwind O_3 and aerosol nitrate formation depending on their composition and functionalities.

In Chapter 4, with high time resolution *in situ* observations of HONO and auxiliary measurements, I showed the existence of secondary HONO sources responsible for HONO formation in the fire smoke during daytime hours. Despite the high HONO primary emissions inferred from some of the youngest plume intercepts in WE-CAN, secondary HONO takes up over 90% in aged (> 2h) smoke due to the rapid photolytic loss of emitted HONO. I demonstrated that secondary sources of HONO can largely be explained by a linear combination of two processes – the photolysis of particulate nitrate and the reactive uptake of NO_2 to smoke aerosol particles. I mapped out variations in the missing HONO source across a wide span of wildfire characteristics, and placed an upper limit on the magnitude of HONO source parameters based on field observations. I found that the mean enhancement factor for particulate nitrate photolysis relative to that of gas-phase HNO_3 is significantly lower than previously reported, while the heterogeneous NO_2 reactive uptake to smoke particles could be more important than previous field studies have indicated, with a mean NO_2 reactive uptake coefficient of 4.0×10^{-4} to submicron aerosol mass forming HONO for all different fires combined. The previously overlooked secondary HONO source might increase the oxidizing capacity of wildfire smoke plumes significantly downwind of the emission source and therefore affect the formation and lifetime of other secondary wildfire smoke components.

5.2 Potential Future Research Directions

5.2.1 High Resolution 3-D chemical modeling of wildfire plumes

The edges and the center within a fire plume intercept are very distinct even with the same ages due to differences in physiochemical processing inside the dense dark center compared to the dilute lighter edges of the plume (Figure 5.1). Plume centers are optically thicker than the wing or edges of the same plume, which translates to varying amount of radiation level and photochemical

processing in the plume cross section. Photolysis mainly occurs on the outer edge of the plume, giving rise to gradients in HO_x and O_3 levels not only along the plume-advecting direction, but also in the plume-dispersing direction. Some of the fresh plumes that we sampled are dark in the center with possible nighttime chemistry. These behaviors imply a complex 3-D variation in the chemical processing of wildfire plumes.

Garofalo et al. (2019) and Palm et al. (2021) revealed that the variability within a single transect could be larger than the downwind transect-to-transect differences, with strong crosswind gradients for reactive compounds including HONO in fresh wildfire plumes. These results highlight the key differences in the cross-plume chemistry and indicate the need to develop a 2D and 3D representation of plume chemistry in order to better understand the physical and chemical mechanisms operating as smoke plumes evolve. The spatial gradients offer valuable insights into the changes in photochemical drivers with age and across the plume, particularly for the highly non-linear chemistry like O_3 photochemistry. The edge effects together with different dilution rates may drive the differences in OH and NO levels within a plume transect, leading to variable OH exposure and VOC reactivity as the plume travels downwind, which have important implications for subsequent RO_2 chemistry and O_3 formation. More efforts are needed to analyze cross-plume chemistry and examine how important edge effects are for explaining the overall chemical evolution of the plume at different ages to help further constrain the chemical heterogeneity in real wildfire plumes.

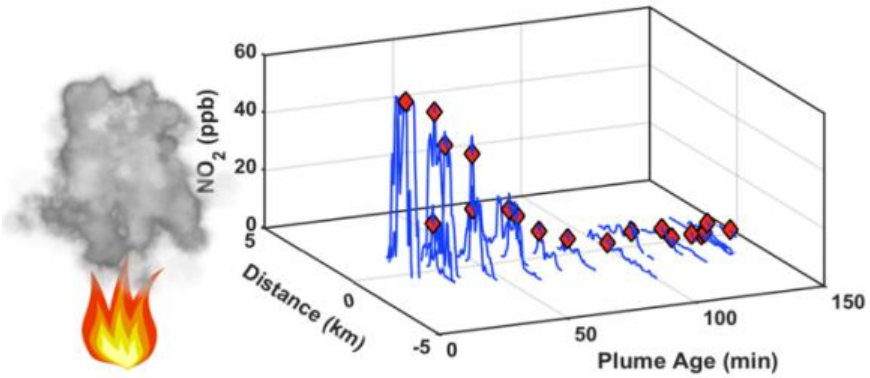

Figure 5.1 Evolution of NO_2 mixing ratios with plume age and cross-plume distance in Taylor Creek Fire.

5.2.2 Global modelling and satellite analysis of fire characteristics

My work has suggested that emissions of HONO in wildland fires are significantly influenced by fuel characteristics such as moisture and N content as well as combustion conditions. Varying emissions from different fuel types in turn may impact the photochemical transformations both near-source and downwind (Akagi et al., 2011; Van Der Werf et al., 2010). Quantifying the emissions from different fuel types in all major ecosystems is fundamental to advancing our ability to estimate smoke strength and evolution. Satellite data offer global coverage and provide essential information of fire attributes such as injection height, fire intensity, and burned areas. With newer and more sensitive satellite systems in place for atmospheric studies, our understanding of biomass burning impacts at a regional and global scale would be substantially improved by leveraging satellite-based techniques in combination with global modeling. For example, assessing the relationships among fuel types, burning conditions, and plume characteristics using satellite retrievals may help increase prediction accuracies of levels of secondary pollutants like formaldehyde and ozone in chemical transport models. Theys et al. (2020) reported varying HONO

enhancement ratios with biome type based on a global survey of satellite sounder observations, with highest values corresponding to extratropical evergreen forests burning and lowest from savannas and grasslands burning. Additionally, there are systematic differences in emissions and plume compositions with time of day, which may lead to variances in plume chemistry (Robinson et al., 2021). Yet, constraints on the changes in emissions from fires occurring across different biomes and subsequent differences in plume chemistry are not well represented in atmospheric chemistry models. More research on characterizing and modeling the emissions of trace gases across biomes from satellite data will help better represent the emission cocktail from specific wildfires.

5.2.3 Human health risks of fire smoke exposure

The frequency and severity of wildfires are on the rise in the context of global warming. In 2021 alone, a total of 58,733 wildfires was reported across the United States that had burned more than 7.13 million acres. In addition to the billions spent on suppressing these fires, more costs are taken in the health of people suffering from the fire pollutants even hundreds of miles away from the sources, with large quantities of soot and secondary pollutants released into the atmosphere from the enormous plumes of smoke spreading across a wide region. It is important to evaluate the health risks resulting from the hazardous air pollutants emitted or produced from wildfires as a function of distance or plume aging. O'Dell et al. (2020) showed that acrolein, formaldehyde, benzene, and hydrogen cyanide are the dominant contributors to the gas-phase pollutant risk in smoke plumes, and identified their relationships with associated health risks. The evolution of these fire-generated compounds depends strongly on near-field chemistry, and forecasting their contribution to exposure requires fidelity in the simulation of plume chemistry and not just emissions and transport. Building upon my work on modeling wildfire plume chemistry, further

investigations on the chemical transformations of fire smoke when mixed with urban air could be conducted to better understand the potential health hazards in fire-prone regions. As urban NO_x decline with stricter emission controls, the impact of wildfire smoke on respiratory irritants like O_3 in urban areas may also change, and assessing how the paradigm transitions is important to estimate the health risks from wildfires. Further efforts could be invested in systematically probing the smoke exposure of critical air pollutants from wildfires of different fire conditions and fuel types, and mapping the spatial correlation between fire emissions and health loss.

5.3 REFERENCES

Akagi, S. K., Yokelson, R. J., Wiedinmyer, C., Alvarado, M. J., Reid, J. S., Karl, T., et al. (2011). Atmospheric Chemistry and Physics Emission factors for open and domestic biomass burning for use in atmospheric models. *Atmos. Chem. Phys*, *11*, 4039–4072. https://doi.org/10.5194/acp-11-4039-2011

Garofalo, L. A., Pothier, M. A., Levin, E. J. T., Campos, T., Kreidenweis, S. M., & Farmer, D. K. (2019). Emission and Evolution of Submicron Organic Aerosol in Smoke from Wildfires in the Western United States. *ACS Earth and Space Chemistry*, *3*(7), 1237–1247. https://doi.org/10.1021/acsearthspacechem.9b00125

O'Dell, K., Hornbrook, R. S., Permar, W., Levin, E. J. T., Garofalo, L. A., Apel, E. C., et al. (2020). Hazardous Air Pollutants in Fresh and Aged Western US Wildfire Smoke and Implications for Long-Term Exposure. *Environmental Science and Technology*, *54*(19), 11838–11847. https://doi.org/10.1021/ACS.EST.0C04497/SUPPL_FILE/ES0C04497_SI_002.XLS

Palm, B. B., Peng, Q., Hall, S. R., Ullmann, K., Campos, T. L., Weinheimer, A., et al. (2021). Spatially Resolved Photochemistry Impacts Emissions Estimates in Fresh Wildfire Plumes. *Geophysical Research Letters*, *48*(23), e2021GL095443. https://doi.org/10.1029/2021GL095443

Robinson, M. A., Decker, Z. C. J., Barsanti, K. C., Coggon, M. M., Flocke, F. M., Franchin, A., et al. (2021). Variability and Time of Day Dependence of Ozone Photochemistry in Western Wildfire Plumes. *Environmental Science and Technology*, *55*(15), 10280–10290. https://doi.org/10.1021/ACS.EST.1C01963/SUPPL_FILE/ES1C01963_SI_001.PDF

Theys, N., Volkamer, R., Müller, J. F., Zarzana, K. J., Kille, N., Clarisse, L., et al. (2020). Global nitrous acid emissions and levels of regional oxidants enhanced by wildfires. *Nature Geoscience*, *13*(10), 681–686. https://doi.org/10.1038/S41561-020-0637-7

Van Der Werf, G. R., Randerson, J. T., Giglio, L., Collatz, G. J., Mu, M., Kasibhatla, P. S., et al. (2010). Global fire emissions and the contribution of deforestation, savanna, forest, agricultural, and peat fires (1997-2009). *Atmospheric Chemistry and Physics*, *10*(23), 11707–11735. https://doi.org/10.5194/ACP-10-11707-2010

APPENDIX

Chapter 2 has been previously published:

Peng, Q., Palm, B. B., Melander, K. E., Lee, B. H., Hall, S. R., Ullmann, K., et al. (2020). HONO Emissions from Western U.S. Wildfires Provide Dominant Radical Source in Fresh Wildfire Smoke. *Environmental Science and Technology*, *54*(10), 5954–5963. https://doi.org/10.1021/acs.est.0c00126

Chapter 3 has been previously published:

Peng, Q., Palm, B. B., Fredrickson, C. D., Lee, B. H., Hall, S. R., Ullmann, K., et al. (2021). Observations and Modeling of NOx Photochemistry and Fate in Fresh Wildfire Plumes. *ACS Earth and Space Chemistry*, *5*(10), 2652–2667. https://doi.org/10.1021/acsearthspacechem.1c00086

Chapter 4 is currently in preparation for publication

Peng, Q., Palm, B. B., Fredrickson, C. D., Lee, B. H., Hall, S. R., Ullmann, K., et al. (2022) Direct Constraint on Secondary HONO Production in Aged Wildfire Smoke from Airborne Measurements in Western US